Strongly correlated electrons : from two dimensions to heterostructures

Axel Euverte

UNIVERSITÉ DE NICE SOPHIA ANTIPOLIS - UFR Sciences

École doctorale des Sciences Fondamentales et Appliquées

THÈSE

pour obtenir le titre de

Docteur en Sciences

de l'Université de Nice Sophia Antipolis

Discipline: Physique Statistique

présentée et soutenue par

Axel EUVERTE

Strongly Correlated Electrons: From two dimensions to heterostructures

Thèse dirigée par George G. BATROUNI

soutenue à l'Institut Non Linéaire de Nice le 11 Octobre 2013

Jury:

Mme	VIGNOLO Patrizia	Professeur	Présidente
M.	MURAMATSU Alejandro	Professeur	Rapporteur
M.	SIMON Pascal	Professeur	Rapporteur
M.	ROUX Guillaume	Maître de Conférences	Examinateur
M.	HEBERT Frédéric	Maître de Conférences	Examinateur
M.	BATROUNI George G.	Professeur	Directeur

Contents

Introduction **1**

Introduction en français **5**

1 Model and Methods **9**
1.1 Introduction . . . 9
1.2 Electrons on a lattice . . . 10
1.2.1 Second quantization . . . 10
1.2.2 Hubbard model . . . 11
1.2.3 Noteworthy limits . . . 14
1.3 Monte Carlo methods . . . 16
1.3.1 Quantum Monte Carlo . . . 17
1.3.2 Determinant QMC . . . 19
1.3.3 Limitations and tricks . . . 20
1.4 Measurement of physical quantities . . . 21
1.4.1 Static and dynamical measurements . . . 21
1.4.2 Long-range order . . . 23
1.4.3 Analytic continuation . . . 24
1.4.4 Spectral functions . . . 26
1.4.5 Electrical conductivity . . . 28
1.5 Assessment of the theoretical framework . . . 29

2 Correlations in a band insulator **31**
2.1 Motivations . . . 31
2.1.1 Anderson-Mott transition . . . 31
2.1.2 Bilayer models . . . 32
2.1.3 The ionic Hubbard model . . . 33
2.2 A correlated band insulator . . . 34
2.2.1 Hamiltonian . . . 34
2.2.2 Preliminary phase diagram . . . 36
2.3 Magnetism . . . 37
2.4 Local moments . . . 39
2.5 Spin correlations . . . 41
2.6 Energy gaps and spectral functions . . . 43
2.7 Conclusions . . . 46

3 Finite bandwidth in a heavy-fermion model **49**
3.1 Introduction . . . 49
3.1.1 Resistivity minimum . . . 49
3.1.2 Heavy-fermions . . . 50
3.2 The Periodic Anderson Model . . . 52
3.3 Finite f-orbital bandwidth . . . 53
3.3.1 Non-interacting Limit . . . 55
3.3.2 Mean field theory . . . 56
3.4 Magnetic properties . . . 57
3.5 Spectral functions . . . 61
3.6 Conclusion . . . 63

4 Metal-Mott insulator Interface **67**
4.1 Introduction . . . 67
4.1.1 Theoretical methods . . . 69
4.1.2 Metal-Mott Insulator Interface . . . 70
4.2 Metal-Mott insulator interface . . . 71
4.2.1 Hamiltonian . . . 72
4.3 Spin correlations and singlet formation . . . 72
4.4 Suppression of magnetic order . . . 76
4.5 Spectral functions . . . 78
4.6 dc Conductivity . . . 79
4.7 More layers . . . 82
4.8 Summary . . . 83

Conclusion **87**

Conclusion en français **91**

Bibliography **95**

Abstract **107**

Introduction

Dimensionality is of fundamental importance in physics. From a theoretical perspective, the properties of a given model often change dramatically upon changing its number of spatial dimensions. A textbook example is the isotropic quantum Heisenberg model, which displays no spontaneous magnetization at finite temperature in two dimensions, while in the three dimensional case there is a finite critical temperature below which the system is ordered. This result can be generalized by way of the Mermin-Wagner theorem, which states that no continuous symmetry can be spontaneuously broken at finite temperature when the dimension is lower than or equal to 2, provided that the interactions are short-ranged.

While the study of dimensions other than 3 might seem irrelevant at first sight, there are plenty of experimentally accessible systems whose properties are mainly ruled by low-dimensional phenomena. For instance, many bulk crystals are arranged in non-isotropic structures in which interactions will mostly happen within chains or layers, leading to effective one- or two-dimensional physical properties. Moreover, among such low-dimensional systems appear some of the most intriguing and technologically promising materials, as the recently discovered layered high-temperature superconductors pnictides.

The field we are interested in here is condensed matter physics, which aims at describing the collective properties of a large number of atoms. Given that very few exact solutions are known for quantum systems beyond the most simple case of the hydrogen atom, this task implies the use of approximations that simplify the complexity of the problem. The notion of energy scale is therefore of crucial importance in order to neglect the degrees of freedom that will take no part in the phenomena under consideration. For instance, condensed matter theory can in most cases ignore the structure of the atomic nuclei that involve energies considerably larger than the electronic properties of interest. Effective models involving only the essential degrees of freedom can therefore be derived, but even these are in general extremely intricate. While many exact solutions can be computed analytically for quantum systems in one dimension or infinite dimensions, only approximate results can in general be obtained for intermediate dimensions. The advances made during the last decades in both computer performance and algorithms have made numerical simulations an unavoidable tool for understanding such models.

This work is devoted to describing physical systems in which a few two-

dimensional electronic layers are coupled together. While 2D systems have been the object of intensive research -largely motivated by the fact that high-temperature superconducting cuprates are essentially made of weakly coupled layers- much less has been done on the case of layered systems. The latter can equivalently describe 2D models in which more than one electronic band is involved, or a layered material in which atomic planes are coupled and form a complex heterostructure. In spite of several limitations, which we will detail later on, the numerical technique we employ can compute "exact" properties of quantum clusters at finite temperature that take into account spatial correlations, thus providing an important complementary alternative to other methods.

The tools and methods will be presented in Chapter 1. After briefly introducing the formalism of second quantization, we will derive the effective model that will be our theoretical framework, the Hubbard model. A few noteworthy physical limits of the latter will be discussed, before we present the numerical method called the Determinant Quantum Monte Carlo (DQMC). Our focus will be mainly on explaining the underlying concepts rather than on presenting detailed derivations of the formalisms. A section will be devoted to introducing the physical measurements that we will use in the subsequent chapters, which will offer the opportunity to illustrate a few standard results on the Hubbard model, as well as to underline some limitations and "tricks of the trade" of our numerical method. We will finally succinctly comment on a few other major methods used to study the Hubbard model, focusing on their advantages and drawbacks against the DQMC method.

The study of a first system will be presented in the second Chapter, where two Hubbard planes will generate two electronic bands separated by a band gap of tunable width. Motivated by recent investigations on the effect of electronic correlation in band insulators, a particular realization of such a correlated insulator will be analyzed. The results will be systematically compared against those published a few years ago for the same hamiltonian by means of the Dynamical Mean Field Theory (DMFT) technique, showing in particular a strong disagreement with this work as we found no shrinking of the energy gap upon increasing the electronic repulsion. Comparisons will also be made against work previoulsy done on a very similar system, the Ionic Hubbard Model, in which a metallic phase was found in between two insulating phases, drawing much attention and controversy.

Chapter 3 will be devoted to another multi-orbital two-dimensional system. The Periodic Anderson Model (PAM) is a theoretical milestone in the study of the coupling of electronic transport with magnetism that has been used to describe the behaviour of an important class of correlated compounds known

as *heavy fermions*. We will extend this model by allowing a tunable mobility in the magnetic band, therefore exploring a broad spectrum of physical phenomena related to the interplay of transport and magnetism. In particular, it will be shown that magnetic moments and correlations are maximized for a finite bandwidth f-band. The temperature dependence will be discussed, revealing the distinct energy scales of the model.

In Chapter 4, several Hubbard planes will no longer describe several orbitals of a two-dimensional system but rather the atomic layers of a few unit cells thick heterostructure. The latter will be made of a thin interface between a metal and a correlated insulator. After a brief introduction of the recent massive interest in correlated heterostructures and their potential applications in the field of micro-electronics, we will present different works previously done on similar systems through alternative theoretical methods as well as experimental investigations. It will be shown that, as the coupling at the interface is tuned, the system undergoes a transition to an unexpected insulating paramagnetic state that involves atomic layers not directly at the interface, before another transition at large coupling in which the interface decouples from the bulk, the latter recovering its initial properties. The effect of the correlation strength and of the interface thickness on the propagation of the intermediate state into the materials will be finally discussed.

The last chapter has our conclusions and perspectives for future work.

Introduction en français

> "[...] D'abord, nous allons faire le chapitre des finances, ensuite nous parlerons d'un petit système que j'ai imaginé pour faire venir le beau temps et conjurer la pluie."
>
> — Alfred Jarry [1]

La notion de dimensionalité a une importance fondamentale en physique. D'un point de vue théorique, les propriétés d'un modèle donné varient souvent de façon spectaculaire en fonction du nombre de dimensions spatiales. Un exemple classique est le modèle de Heisenberg quantique isotrope, qui n'a pas d'aimantation spontanée à température finie en deux dimensions, tandis qu'il existe en trois dimensions une température critique non nulle en deçà de laquelle le système est ordonné. Ce résultat peut être généralisé au moyen du théorème de Mermin-Wagner, qui établit qu'il ne peut y avoir de brisure spontanée de symétrie continue à température finie dans un système de dimension inférieure ou égale à 2, tant que les interactions sont de courte portée.

Bien qu'au premier abord l'étude de dimensions autres que 3 puisse sembler peu pertinente, il existe de nombreux systèmes accessibles expérimentalement dont les propriétés sont dominées par des phénomènes de basse dimensionnalité. Par exemple, de nombreux cristaux présentent des structures non-isotropes dans lesquelles les interactions ont lieu au sein de chaînes ou de plans, conduisant à des propriétés effectives en une ou deux dimensions. De plus, parmi ces systèmes de basse dimensionalité figurent des matériaux aux propriétés fascinantes qui offrent la possibilité d'applications prometteuses, tels les "pnictides" dont la supraconductivité à haute température n'a été découverte que récemment.

Le domaine qui nous intéresse est celui de la physique de la matière condensée, qui vise à décrire les propriétés collectives d'un grand nombre d'atomes. Étant donné qu'il n'existe que très peu de solutions mathématiques exactes pour des systèmes quantiques au-delà de l'atome d'hydrogène, cette tâche impose d'avoir recours à des approximations qui réduisent la complexité du problème. La notion d'échelle d'énergie est par conséquent cruciale afin de négliger les degrés de liberté qui ne contribuent pas aux phénomènes considérés. En matière condensée, par exemple, on peux en général ignorer la structure interne des noyaux atomiques, qui implique des énergies beaucoup plus élevées que les propriétés électroniques auxquelles on s'intéresse. Des modèles effectifs

n'incluant que les degrés de liberté nécessaires peuvent donc être dérivés, mais ceux-ci demeurent souvent d'une grande complexité. Bien que de nombreuses solutions exactes existent en une dimension ou en dimension infinie, seuls des résultats approchés peuvent en général être obtenus en dimensions intermédiaires. Les progrès qu'ont connu au cours des dernières décennies les performances des ordinateurs et des algorithmes font des simulations numériques un outil incontournable pour la compréhension de ces modèles.

Ce travail porte sur des systèmes physiques dans lesquels plusieurs couches électroniques sont couplées. Tandis que les systèmes 2D ont été l'objet de nombreux travaux, en grande partie motivés par le fait que les cuprates supraconducteurs à haute température sont composés de plans faiblement couplés, les systèmes en couches demeurent dans une large mesure inexplorés. Ces derniers peuvent décrire, de façon équivalente, des modèles 2D dans lesquels plusieurs bandes d'énergie sont prises en compte, ou des matériaux constitués de couches bidimensionnelles dans lesquels les plans atomiques couplés composent des hétérostructures complexes. En dépit de certaines restrictions qui seront discutées plus loin, la technique numérique que nous utilisons permet de calculer de façon "exacte" les propriétés d'agrégats quantiques à température finie en prenant en compte les corrélations spatiales, offrant ainsi une alternative complémentaire d'autres méthodes.

Les outils et méthodes seront présentés au Chapitre 1. Après avoir introduit le formalisme de la seconde quantification, nous dériverons le modèle effectif qui nous servira de base, le modèle de Hubbard. Quelques limites physiques notables de ce dernier seront discutées, puis nous présenterons l'algorithme appelé Monte Carlo Quantique du déterminant (DQMC). Notre but sera principalement d'expliquer les concepts sous-jacents plutôt que de présenter une dérivation détaillée des formalismes. Une section sera dédiée à la description des mesures physiques que nous emploierons au cours des chapitres suivants, ce qui nous offrira l'opportunité d'illustrer quelques résultats classiques concernant le modèle de Hubbard, ainsi que certaines limites et subtilités de notre méthode numérique. Pour finir, nous évoquerons succinctement quelques autres méthodes utilisées pour étudier le modèle de Hubbard, en nous concentrant sur leurs avantages et inconvénients par rapport à la méthode DQMC.

L'étude d'un premier système sera présentée au cours du second chapitre, dans lequel deux plans de Hubbard engendreront deux bandes d'énergie séparées par une bande interdite (ou *gap*) de largeur ajustable. Une réalisation particulière d'un tel système sera étudiée, et motivée par de récentes recherches sur les effets de la corrélation électronique dans les isolants de bande. Les résultats seront comparés de façon systématique à ceux publiés il y a quelques années pour le même hamiltonien au moyen de la Théorie du Champ Moyen

Dynamique (DMFT), démontrant en particulier un important désaccord au sujet du comportement du gap d'énergie lorsque la répulsion électronique est augmentée. On fera également la comparaison avec un modèle très similaire, le modèle de Hubard ionique, dans lequel une phase métallique avait été trouvée entre les deux phases isolantes.

Le Chapitre 3 sera dédié à un autre modèle bidimensionnel comprenant plusieurs orbitales. Le modèle périodique d'Anderson (PAM) est un jalon théorique essentiel pour l'étude du couplage entre transport électronique et magnétisme qui a permit la description d'une classe importante de matériaux correlés appelés *fermions lourds*. Nous étendrons ce modèle en permettant une mobilité électronique ajustable dans la bande magnétique, permettant par conséquent d'explorer une large gamme de phénomènes physiques engendrés par la présence simultanée de transport électronique et de magnétisme. En particulier, nous montrerons que la formation de moments locaux ainsi que les corrélations magnétiques sont maximisées quand la largeur de bande est étroite mais non-nulle. La dépendance en température sera également discutée, révélant les différentes échelles d'énergie du modèle.

Dans le dernier chapitre, les plans de Hubbard ne décriront pas les plusieurs orbitales d'un système bidimensionnel, mais plutôt les couches atomiques d'une hétérostructure épaisse de quelques cellules unité. Cette dernière sera composée d'une interface mince entre un métal et un isolant corrélé. Après une brève mention du récent intérêt porté aux hétérostructures corrélées et de leurs possibles applications dans le domaine de la micro-électronique, nous présenterons différents travaux effectués sur des systèmes similaires à l'aide d'autres méthodes théoriques, ainsi que des études expérimentales. Nous montrerons que, en ajustant le couplage à l'interface, le système présente une transition vers un état isolant paramagnétique qui implique des couches atomiques qui ne sont pas en contact direct avec l'interface. Dans le régime de couplage fort, on observera une autre transition dans laquelle l'interface se découple du volume, ce dernier recouvrant ses propriétés initiales. Les effets de la valeur de la corrélation et de l'épaisseur de la structure considérée sur la pénétration de la phase paramagnétique intermédiaire seront finalement discutés.

Le dernier chapitre résume nos conclusions et les perspectives de développement ultérieur.

Chapter 1

Model and Methods

1.1 Introduction

The standard properties of metals are well described within the framework of the Fermi gas, in which the degrees of freedom of independent electrons are mainly ruled by the Pauli exclusion principle that leads the available particle-hole excitations to be restricted in the vicinity $k_B T$ of the Fermi energy, so that only few of the total number of electrons are involved in the thermodynamic properties. Since in most metals the Coulomb interaction between electrons is typically of the order of magnitude of the kinetic energy, it is far from trivial that this description is relevant for describing even simple metals. The *Fermi liquid* theory, developed early on by Landau, addresses this question by acknowledging that the eigenstates of the interacting case shall be adiabatically connected to the eigenstates of the noninteracting problem. The excitations will therefore be described in terms of *quasi-particles* that share the same equilibrium properties as the non-interacting electrons but with "renormalized" parameters (such as the mass).

Although the Fermi liquid theory has proven to be extremely helpful in accounting for the thermodynamic properties of metals, there are broad classes of models and compounds in which this description breaks down. In particular the electron scattering, that scales as the square of the temperature T predicted in the Fermi liquid context, is not compatible with the linear resistivity observed in doped cuprates. In order to deal with non-Fermi liquid behavior, it is necessary to go beyond the picture drawn by Landau and to deal with electronic correlation in a non-pertubative way. Because of the complexity of the problem, it is often necessary to have recourse to *effective models* that are simpler than the exact problem but capture nonetheless some of its fundamental properties. The analysis of these models remains usually cumbersome, so that approximate analytical or numerical methods are required in order to study them.

After introducing briefly the formalism of second quantization, the goal of this chapter is to present the particular model we will focus on, known as the *Hubbard model*, as well as the numerical method we shall use throughout this

work, the *Determinant Quantum Monte Carlo* method. Some general properties of the Hubbard model will also be discussed, with a special emphasis on the advantages and limitations inherent to these model and numerical method.

1.2 Electrons on a lattice

The goal of this section is to introduce the tools we will be using below. We shall therefore not get into unnecessary details, and refer the reader the existing references for further details and rigour (see for example the books by Mahan [2] or Coleman [3]).

1.2.1 Second quantization

In quantum mechanics, "first quantization" refers to the formalism in which a system of N particles is described by means of a wavefunction Ψ, whose evolution is determined by the Schrödinger equation

$$i\hbar\frac{\partial}{\partial t}\Psi = \hat{H}\Psi. \tag{1.1}$$

When dealing with the statistical properties of an open system, the first quantization formulation is cumbersome and it is convenient to turn to a formalism in which the basis set is made of products of the independent particles wavefunctions, called second quantization. The vector $\Phi_{\{n_1,\ldots,n_i,\ldots\}} = |n_1, n_2, \ldots, n_i, \ldots\rangle$ then defines the state with n_i particles in the state i, the full set of all possible occupation numbers generating a complete basis set for the many-body system. This basis can be obtained by defining the vacuum state $|0\rangle$, and a set of operators $\{c_i^\dagger\}$ that create a particle in a given state:

$$\Phi_{\{n_i\}} = \prod_i (c_i^\dagger)^{n_i} |0\rangle . \tag{1.2}$$

The $\{c_i^\dagger\}$ operators are called creation operators, while their adjoints $\{c_i\}$ are called destruction operators for they remove particles from the system.

In order to enforce the symmetry of the state upon permutation of two particles, one must impose commutation relation between operators. We will focus on the antisymmetric case of fermions, the symmetric bosonic case being obtained in a similar manner. Let us first introduce the anticommutator between operators $\hat{A}$ and $\hat{B}$:

$$\{\hat{A}, \hat{B}\} = \hat{A}\hat{B} + \hat{B}\hat{A} \tag{1.3}$$

We then define the anticommutation relation for the fermionic creation and destruction operators

$$\begin{cases} \{c^\dagger_{i,\sigma}, c_{j,\sigma'}\} = \delta_{i,j}\delta_{\sigma,\sigma'} \\ \{c^\dagger_{i,\sigma}, c^\dagger_{j,\sigma'}\} = \{c_{i,\sigma}, c_{j,\sigma'}\} = 0. \end{cases} \tag{1.4}$$

The Pauli exclusion principle ensures immediately from these definitions, enforcing no state can be occupied by more than one particle ($n_i \in 0, 1$):

$$c^\dagger_{i,\sigma} c^\dagger_{i,\sigma} = -c^\dagger_{i,\sigma} c^\dagger_{i,\sigma} = 0. \tag{1.5}$$

1.2.2 Hubbard model

In order to describe the electronic properties of a crystal, a simple model consists of considering electrons on a lattice. When the Coulomb interaction between the electrons is not taken into account this model can be easily solved and describes satisfactorily a broad class of metallic compounds. The only interaction we thus take temporarily into account is the effective potential generated by the mean electronic background and the underlying ionic lattice, $V(\mathbf{r})$. For the sake of simplicity we also consider only one electronic band, and shall consider multi-band systems at a later stage. When the lattice is translationally invariant, Bloch theorem tells us the wavefunctions that are solutions of the Schrödinger equation for this problem are Bloch states, namely functions that are can be written as:

$$\psi_{\mathbf{k}}(\mathbf{r}) = e^{i\mathbf{k}\cdot\mathbf{r}} u_{\mathbf{k}}(\mathbf{r}), \tag{1.6}$$

where $\mathbf{k}$ denotes a momentum and $u_{\mathbf{k}}(\mathbf{r})$ is a function that has the same periodicity as the ionic potential.

The Schrödinger equation then reads:

$$\mathcal{H}_0 \psi_{\mathbf{k}}(\mathbf{r}) = [-\frac{\hbar^2}{2m}\nabla^2 + V(\mathbf{r})]\psi_{\mathbf{k}}(\mathbf{r}) = E_{\mathbf{k}}\psi_{\mathbf{k}}(\mathbf{r}). \tag{1.7}$$

Because of the Pauli principle, each eigen-energy $E_{\mathbf{k}}$ can be occupied by at most two electrons, corresponding to the spin states $\sigma \in \{\uparrow, \downarrow\}$. The maximum of the eigen-energies that are occupied is called the *Fermi energy*, E_F, and depends on the number of electrons present in the system. The Fermi energy defines, in momentum space, the Fermi surface around which most electronic processes occur at low temperature. It is now convenient to switch to the second quantization formalism and define the field operator $\Psi_\sigma(\mathbf{r})$ that destroys an electron of spin σ at the position $\mathbf{r}$:

$$\Psi_\sigma(\mathbf{r}) = \sum_{\mathbf{k},\sigma} \psi_{\mathbf{k}}(\mathbf{r}) c_{\mathbf{k},\sigma}. \tag{1.8}$$

The field operators obey the canonical anticommutation relations if the Bloch states are normalized. It is possible to show that the free electron Hamiltonian operator takes, in this language, the diagonal form in momentum space:

$$\hat{\mathcal{H}}_0 = \sum_{\mathbf{k},\sigma} E_{\mathbf{k}} c^\dagger_{\mathbf{k},\sigma} c_{\mathbf{k},\sigma} = \sum_{\mathbf{k},\sigma} E_{\mathbf{k}} n_{\mathbf{k},\sigma}. \tag{1.9}$$

We introduced in the last equation the *number operator* $n_{\mathbf{k},\sigma}$ that counts the number of electrons with momentum $\mathbf{k}$ and spin σ, and that in the fermionic case takes the values 0 or 1. Let us now add to this non-interacting system the Coulomb interaction. To do so, it is convenient to introduce localized states centered on an atomic site labelled i of coordinates $\mathbf{R}_i$, called Wannier functions, and relate them to the non-local Bloch states through the Fourier transform

$$\phi_i(\mathbf{r}) = \frac{1}{N} \sum_{\mathbf{k}} e^{-i\mathbf{k}\cdot\mathbf{R}_i} \psi_{\mathbf{k}}(\mathbf{r}), \tag{1.10}$$

where N is the number of sites. By defining the creation and destruction operators for Wannier states as the Fourier transforms of the respective operators for Bloch states, we can now write the field operators equivalently in term of localized or delocalized operators:

$$\Psi_\sigma(\mathbf{r}) = \sum_{\mathbf{k},\sigma} \psi_{\mathbf{k}}(\mathbf{r}) c_{\mathbf{k},\sigma} = \sum_{i,\sigma} \phi_i(\mathbf{r}) c_{i,\sigma}. \tag{1.11}$$

The non-interacting Hamiltonian can then be rewritten in real space as

$$\hat{\mathcal{H}}_0 = \sum_{i,j,\sigma} t_{i,j} c^\dagger_{i,\sigma} c_{j,\sigma}, \tag{1.12}$$

where we introduced the hopping term that accounts for the kinetic energy betwen the sites i and j

$$t_{i,j} = \frac{1}{N} \sum_{\mathbf{k}} e^{i\mathbf{k}\cdot(\mathbf{R}_i - \mathbf{R}_j)} E_{\mathbf{k}}. \tag{1.13}$$

The set of Wannier functions makes it possible to account for the electron-electron interaction. The interaction term representing the Coulomb repulsion $V(|\mathbf{r} - \mathbf{r}'|)$ reads in terms of field operators

$$\begin{aligned} \hat{\mathcal{U}} &= \int d\mathbf{r} d\mathbf{r}' \Psi^\dagger_\sigma(\mathbf{r}) \Psi^\dagger_{\sigma'}(\mathbf{r}') V(|\mathbf{r} - \mathbf{r}'|) \Psi_{\sigma'}(\mathbf{r}') \Psi_\sigma(\mathbf{r}) \\ &= \sum_{i,j,k,l} U_{i,j,k,l} c^\dagger_{i,\sigma} c^\dagger_{j,\sigma'} c_{k,\sigma'} c_{l,\sigma}, \end{aligned} \tag{1.14}$$

with

$$U_{i,j,k,l} = \int d\mathbf{r}d\mathbf{r}'\phi_i^*(\mathbf{r})\phi_j^*(\mathbf{r}')V(|\mathbf{r}-\mathbf{r}'|)\phi_k(\mathbf{r}')\phi_l(\mathbf{r}). \tag{1.15}$$

We will now make two assumptions. First, the electron overlap will be neglected beyond nearest-neighbors, which is reasonable since the Wannier functions are tightly localized on the ionic centers. Second, we will restrict the Coulomb repulsion to its on-site component and neglect any further electron-electron interaction. Finally, the band filling is allowed to be tuned by adding a chemical potential term μ. The Hubbard model then reads

$$\hat{\mathcal{H}} = \sum_{\langle i,j\rangle,\sigma} t_{i,j}(c_{i,\sigma}^\dagger c_{j,\sigma} + c_{j,\sigma}^\dagger c_{i,\sigma}) + \sum_i U_i n_{i,\uparrow}n_{i,\downarrow} - \mu\sum_{i,\sigma} n_{i,\sigma}. \tag{1.16}$$

In spite of its appearant lack of complexity, the analysis of this model proves to be difficult and has kept physicists busy for decades.

1.2.2.1 Particle-hole symmetry

A lattice is said to be *bipartite* when two sublattices A and B can be defined such as every site belonging to one of the sublattices is connected only to sites belonging to the other sublattice. For instance this is the case for the square and the honeycomb lattices, while the triangular or the Kagome lattices are not bipartite.

In the case of a bipartite lattice, the Hubbard model has a particle-hole symmetry, which means its properties can equivalently be described in terms of creation and destruction operators for electrons -what we did up to now- or in terms of operators acting on "holes", namely on the absence of an electron:

$$\begin{cases} h_i \to (-1)^i c_i^\dagger \\ h_i^\dagger \to (-1)^i c_i \end{cases} \tag{1.17}$$

where the sign of the term $(-1)^i$ depends on the sublattice in which is located the site i. Upon these transformations the Hubbard Hamiltonian becomes:

$$\hat{\mathcal{H}} = \sum_{\langle i,j\rangle,\sigma} t_{i,j}(h_{i,\sigma}^\dagger h_{j,\sigma} + h.c.) + \sum_i U_i m_{i,\uparrow}m_{i,\downarrow} - \mu\sum_{i,\sigma} m_{i,\sigma} + \sum_{i,\sigma} U_i(\frac{1}{2} - m_{i,\sigma})$$

where we introduced the notation $m_{i,\sigma} = h_{i,\sigma}^\dagger h_{i,\sigma}$ for the number of holes at the site i and with spin σ.

The transformations thus add an extra term that cancels at half-filling $n_{i,\uparrow} = n_{i,\downarrow} = \frac{1}{2}$. In that important special case, the Hubbard model is therefore unchanged upon the particle-hole transformation. More generally it is possible to demonstrate that the phase diagram of the model is symmetric about half-filling.

1.2.3 Noteworthy limits

1.2.3.1 Non-interacting case

We now go back to the situation in which the electrons do not interact, namely in our Hubbard model when the local interaction U_i is zero everywhere. The non-interacting Hamiltonian being diagonal in momentum space, it is natural to consider the dispersion relation $E(\mathbf{k})$ in order to gain some insight into the band structure it generates. The latter depends on the parameters of the model such as the dimension, the geometry of the lattice and the specific pattern of hopping between each pair of sites. For the sake of simplicity we shall focus on the case of the two-dimensional square lattice with homogeneous nearest-neighbor hopping $-t$.

$$\begin{aligned}
\hat{\mathcal{H}}_0 &= \sum_{\langle a,b\rangle,\sigma} t_{a,b}(c^\dagger_{a,\sigma}c_{b,\sigma} + h.c.) \\
&= -t\sum_{a,\sigma}[(c^\dagger_{a,\sigma}c_{a+x,\sigma} + c^\dagger_{a,\sigma}c_{a-x,\sigma} + c^\dagger_{a,\sigma}c_{a+y,\sigma} + c^\dagger_{a,\sigma}c_{a-y,\sigma}) + h.c.] \\
&= -\frac{t}{N}\sum_{a,\sigma}\sum_{k_x,k'_x,k_y,k'_y} e^{ik_x a}e^{-ik'_x(a+1)}c^\dagger_{k_x,\sigma}c_{k'_x,\sigma} + \dots \\
&= -2t\sum_{k_x,k_y,\sigma}\cos(k_x)c^\dagger_{k_x,\sigma}c_{k_x,\sigma} + \cos(k_y)c^\dagger_{k_y,\sigma}c_{k_y,\sigma}. \qquad (1.18)
\end{aligned}$$

This dispersion relation is represented on Fig.1.1, with the contour lines corresponding to the Fermi surface for a given chemical potential. Since this dispersion is continuous in the thermodynamic limit, no energy gap is present for any band filling; arbitrarily low energy excitations are available and the system is therefore metallic.

The half-filling case $\mu = 0$ presents the distinctive feature of having a square Fermi surface with side length $\sqrt{2\pi}$. When the Coulomb repulsion is non-zero charge excitations are gapped, making double occupancy unfavourable. Low-energy excitations are possible by destroying two quasi-particles located just below the surface and creating two other just above it, where the total momentum of these particles is conserved. Because of the peculiar shape of the Fermi surface, a great number of excitations involving a momentum transfer $\mathbf{k} = \pm(\pi, \pi)$ are available. It can be shown that in the square lattice case this "nesting" of the Fermi surface leads to antiferromagnetic spin-density waves for any interaction $U > 0$ [4].

It is also worth noting that, in the half-filled square lattice, the density of states $N(\omega)$, which counts the number of disctinct quantum states at an energy ω, diverges at the Fermi energy. Such a divergence, known as Van

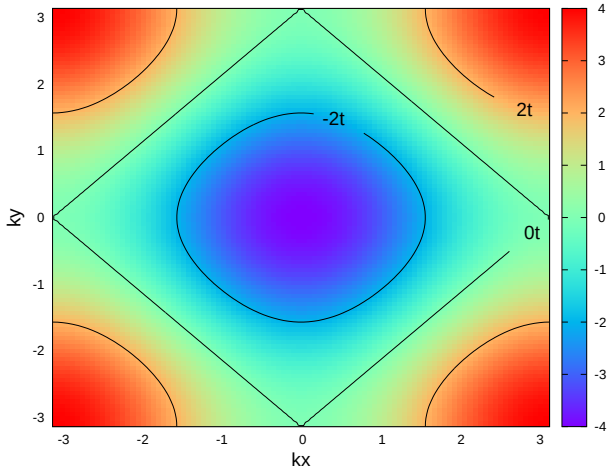

Figure 1.1: Dispersion relation $E(k_x, k_y)$ of the non-interacting Hubbard model in the square lattice. At half-filling the Fermi sea at $E_f = 0$ becomes a square "nested" contour that causes the antiferromagnetic susceptibility to diverge.

Hove singularity, implies that a great number of electrons are available for low-energy excitations.

1.2.3.2 Strong interaction limit

Another important limit is the one in which the on-site repulsion is much larger than the bandwidth $t/U \to 0$. In the large U limit, the ground-state minimizes the number of doubly occupied sites N_d: at or below half-filling there is no double occupancy, while above half-filling there is no empty site. It is then tempting to reduce the complexity of the problem by deriving an effective low-energy model that excludes the sectors with more than the minimal number of double occupancies, leading to a reduction of the dimension of the Hilbert space from 4^N to 3^N (see for example the book by Auerbach [5]).

We define the projectors into the sectors of single occupancy $\hat{\mathcal{P}}_1$ (the sector of empty sites gives a zero contribution to the Hamiltonian)

$$\hat{\mathcal{P}}_1 = \prod_{i=1}^{N} (1 - n_{i,\uparrow} n_{i,\downarrow}). \tag{1.19}$$

The Hubbard hamiltonian becomes in the strong coupling limit the $t - J$ hamiltonian

$$\hat{\mathcal{H}}_{t-J} = -t \sum_{\langle i,j \rangle, \sigma} \hat{\mathcal{P}}_1 (c^{\dagger}_{i,\sigma} c_{j,\sigma} + h.c.) \hat{\mathcal{P}}_1 + J \sum_{\langle i,j \rangle} (\mathbf{S}_i \cdot \mathbf{S}_j - \frac{n_i n_j}{4}). \tag{1.20}$$

where we introduced the spin operators $\{\mathbf{S}_i\}$, and the coupling $J \sim 4t^2/U$. The first term in Eq.(1.20) is the kinetic term of the Hubbard model projected into the subspace of non doubly occupied states. The second term derives from the second order perturbative expansion of the interaction term, corresponding to the virtual hopping of an electron into a doubly occupied state. Because of the Pauli principle, such a process can happen only if the adjacent electrons carry different spins, leading to antiferromagnetism as suggested by the positive sign of coupling J. Hopping terms involving three sites have been here neglected.

At half-filling, every site is singly occupied so the hopping term would necessarily lead to a doubly occupied state; the kinetic term then vanishes and the model becomes the quantum Heisenberg hamiltonian

$$\hat{\mathcal{H}}_H = J \sum_{\langle i,j \rangle} (\mathbf{S}_i \cdot \mathbf{S}_j - \frac{n_i n_j}{4}). \tag{1.21}$$

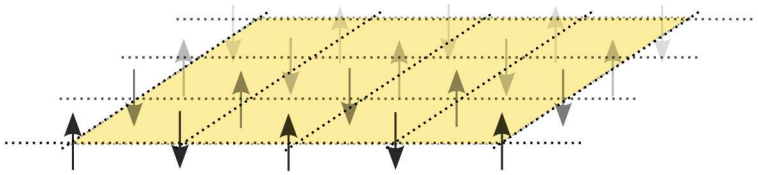

Figure 1.2: In the strong coupling limit $U \to \infty$, the half-filled Hubbard model maps onto the quantum Heisenberg model, in which the absence of charge fluctuations gives way to a leading second-order antiferromagnetic exchange between nearest-neighbor spins.

1.3 Monte Carlo methods

The term *Monte Carlo method* is used to describe a broad range of numerical techniques in which the resolution of the problem is based on performing a stochastic sampling of the configurations of the system. The name is said to be a reference to the "Casino de Monte Carlo", alluding to the randomness of the sampling. This class of methods is applied in a great number of fields going from physical sciences to finance.

In statistical physics, the most important probability distribution is the Boltzmann distribution which gives the probability to measure a state in a given system. In the grand-canonical ensemble -that is when both energy and particle number fluctuate in the vicinity of an equilibrium determined by the temperature T and chemical potential μ- the Boltzmann weight is given by:

$$P_i = P(E_i, N_i) = \frac{e^{-\beta(E_i - \mu N_i)}}{\sum_j e^{-\beta(E_j - \mu N_j)}} \equiv \frac{1}{Z} e^{-\beta(E_i - \mu N_i)}. \tag{1.22}$$

The physical properties of such a finite temperature system are determined for a given observable $\hat{O}$ by the average value it takes over all the states i of the system weighted by the Boltzmann distribution:

$$\langle \hat{O} \rangle = \frac{\sum_j O_j e^{-\beta(E_j - \mu N_j)}}{\sum_j e^{-\beta(E_j - \mu N_j)}} \tag{1.23}$$

A major difficulty arises from the fact that the value of the partition function Z is in general not known, and would require exploring the whole configuration space of the system which is intractable in practice. A way to circumvent this difficulty is to evaluate only the ratio of the probability of two configurations, for example by employing the Metropolis algorithm. Here we review the basic concepts behind it.

The goal is to perform a finite sampling of the configuration space through a random process known as a Markov chain, in which at each step the choice of the next sample does not depend on the history of the chain and is fully characterized by the probability distribution $P(i \to j)$ of the transition between two configurations i and j. The Boltzmann distribution $\{P_i\}$ will be the stationary distribution described by the Markov process if the detailed balance condition is fulfilled:

$$P_i P(i \to j) = P_j P(j \to i). \tag{1.24}$$

When generating a new configuration, an acceptance probability $A(i \to j)$ will thus be defined such as to satisfy the detailed balance condition. The Metropolis probability is one possible choice for that acceptance, and is defined by

$$A(i \to j) = \min(1, \frac{P_j}{P_i}) = \min(1, e^{-\beta[(E_j - \mu N_j) - (E_i - \mu N_i)]}) \tag{1.25}$$

1.3.1 Quantum Monte Carlo

When the temperature is low enough –more precisely when the quantum fluctucations $\hbar\omega$ are larger than the thermal fluctuations $k_B T$– the statistical system can no longer be viewed as composed of classical particles and quantum properties have to be taken into account. It would be deceptive to believe that such a temperature is necessarily close to the absolute zero. For instance, the Pauli principle that prevents fermions from occupying the same state leads in metals to characteristic Fermi energies of order $T \sim 10^4 K$. In such cases, one has to worry about the quantum description of the states, which are then described by operators that make the direct way of sampling configurations

used for classical systems impracticable and require using more sophisticated methods.

A tight-binding Hamiltonian can typically be written in the form

$$\hat{\mathcal{H}} = \hat{\mathcal{T}} + \hat{\mathcal{U}}, \tag{1.26}$$

where $\hat{\mathcal{U}}$ is the interaction term (typically the electron-electron Coulomb repulsion), and $\hat{\mathcal{T}}$ is a kinetic term $\hat{\mathcal{H}}_0 - \mu\hat{\mathcal{N}}$ ($\hat{\mathcal{N}}$ is the number operator that measures the number of particles). While the first term is usually diagonalizable in real-space, and the second term in the momentum-space, the general problem admits in most cases no trivial solution. Perturbation theory is the method of choice when one of the terms dominates, allowing a perturbative expansion in the vicinity of its exact solution, but this approach is bound to fail when both terms are of the same order. By the same token, first principle calculations like density functional theory (DFT) are only valid when the interaction is small compared with the bandwidth. It is thus necessary to have recourse to alternative techniques, among which the Feynman's path integral formulation stands out by the deep insight it brings into quantum mechanics.

The evaluation of the partition function is cumbersome because the kinetic term and the interaction term do not commute. In order to overcome this difficulty, performing a Suzuki-Trotter decomposition allows us to write the partition function as the product of exponentials involving these terms separately:

$$\begin{aligned} Z &= \mathrm{Tr}\ e^{-\beta\hat{\mathcal{H}}} \\ &= \mathrm{Tr}\left(\prod_{l=1}^{L} e^{-\Delta\tau\hat{\mathcal{H}}}\right) \\ &= \mathrm{Tr}\left(\prod_{l=1}^{L} e^{-\Delta\tau\hat{\mathcal{T}}} e^{-\Delta\tau\hat{\mathcal{U}}}\right) + O(\Delta\tau^2), \end{aligned} \tag{1.27}$$

where we introduced the L imaginary time steps $\Delta\tau = \beta L$. The systematic "Trotter error" $O(\Delta\tau^2)$ can in principle be made arbitrarily small by decreasing the time step, up to an additional computational cost.

Among the number of QMC methods that are available, the *Determinant* QMC is the one of choice for fermionic systems. We will describe it briefly in the next section, but we suggest the interested reader to refer, for further details, to the original work by Blankenbecler *et al.* [6], to the chapter by Loh and Gubernatis [7] or to the study of the 2D Hubbard model by White *et al.* [8]. The particular implementation we used, the *quantum electron simulation toolbox* (QUEST), can be found at `http://quest.ucdavis.edu/`.

1.3.2 Determinant QMC

When dealing with quadratic forms of fermionic operators, that is operators that can be written

$$\hat{\mathcal{H}}_l = \sum_{i,j} (H_l)_{ij}\, c_i^\dagger c_j, \tag{1.28}$$

the trace over the product of exponentials of such operators can be evaluated straightforwardly by means of a determinant

$$\mathrm{Tr}\left(e^{\hat{\mathcal{H}}_1} e^{\hat{\mathcal{H}}_2} \dots e^{\hat{\mathcal{H}}_L}\right) = \det\left(1 + e^{-\hat{\mathcal{H}}_L} \dots e^{-\hat{\mathcal{H}}_2} e^{-\hat{\mathcal{H}}_1}\right). \tag{1.29}$$

The latter equality requires the use of algebras that account for the fermionic anticommutation relations, known as Grassman algebras. For a rigorous derivation the reader can refer, for instance, to the book by Negele and Orland [9]. While the kinetic term $\hat{\mathcal{T}}$ already has a quadratic form, the interaction term $\hat{\mathcal{U}}$ is quartic in fermionic operators. It is therefore necessary to transform it into a quadratic form by performing a discrete Hubbard-Stratonovich transformation

$$e^{-\Delta\tau U(n_{i,\uparrow}-\frac{1}{2})(n_{i,\downarrow}-\frac{1}{2})} = C \sum_{h_{i,l}=\pm 1} e^{\lambda h_{i,l}(n_{i,\uparrow}-n_{i,\downarrow})}, \tag{1.30}$$

where $\cosh(\lambda) = e^{\frac{\Delta\tau U}{2}}$ and $C = \frac{1}{2}e^{-\frac{\Delta\tau U}{4}}$. The quartic term is consequently decoupled into a quadratic form by the introduction of an auxiliary Ising-like bosonic field $\{h_{i,l}\}$ known as the Hubbard-Stratonovich field, that couples to the local magnetization at site i, $(n_{i,\uparrow} - n_{i,\downarrow})$, at every time slice l. Coupling the auxiliary field to the spin component S^z breaks the $SU(2)$ invariance of the hamiltonian, which is theoretically restored after sampling over the whole configuration space. Other choices of decomposition are also possible.

The partition function, now expressed in terms of quadratic forms only, can be written as a sum over every possible Hubbard-Stratonovich field

$$Z = C^{LN} \mathrm{Tr}_h \left[\det(M_\uparrow)\det(M_\downarrow)\right], \tag{1.31}$$

where we introduced the trace Tr_h over the Ising field $h = \pm 1$ and the matrices

$$M_\sigma = 1 + e^{-K} e^{-V_\sigma(L)} \dots e^{-K} e^{-V_\sigma(1)}, \tag{1.32}$$

with the kinetic term reading in one dimension

$$K = -\Delta\tau \begin{pmatrix} \mu & t & 0 & & t \\ t & \mu & t & \dots & 0 \\ 0 & t & \mu & & 0 \\ & \dots & & \dots & \\ t & 0 & 0 & & \mu \end{pmatrix} \tag{1.33}$$

and the interaction term

$$(V_\sigma(l))_{ij} = -\lambda\sigma_{i,l}\delta_{i,j}. \tag{1.34}$$

The Metropolis ratio of the Boltzmann weights that determines the acceptance probability of a Markov step from a configuration i to a configuration j thus becomes the product of determinants

$$r(i \to j) = \frac{\det(M_\uparrow(j))\det(M_\downarrow(j))}{\det(M_\uparrow(i))\det(M_\downarrow(i))}. \tag{1.35}$$

Since this quantity is not always positive, its absolute value is usually taken as the Boltzmann weight. This might render the numerical convergence tough because of a numerical *sign problem*, one of the main limitations of QMC methods.

1.3.3 Limitations and tricks

1.3.3.1 The sign problem

In the Determinant QMC formalism we presented, there is *a priori* no reason for the determinants involved in the definition of the partition function to be positive, leading to the possibility of negative Boltzmann weights P_i with no physical meaning. A solution consists in taking the absolute value of these weights when computing the expectation value of an observable $\hat{O}$:

$$\langle\hat{O}\rangle = \frac{\sum_i O_i P_i}{\sum_i P_i} = \frac{\sum_i O_i |P_i| \mathrm{sgn}(P_i)}{\sum_i |P_i| \mathrm{sgn}(P_i)}. \tag{1.36}$$

The problem arises from the fact the average sign decreases exponentially [10], thus leading to large fluctuations and a slow convergence of the measurements

$$\frac{\sum_i P_i}{\sum_i |P_i|} \sim e^{-\beta\Delta F}, \tag{1.37}$$

where we introduced the difference in the free energy ΔF involved by taking the absolute value of the determinants. Since the free energy is an extensive quantity, both decreasing the temperature and increasing the size of the lattice cluster worsen the problem, when one is usually precisely interested in understanding the low-temperature properties of the system in the thermodynamic limit. It can be shown that, among the multiple possible choices for the Hubbard-Stratonovich transformation, none can systematically give the square of a determinant and thus a positive weight [11].

Fortunately, the sign problem is not a concern in several important cases. One is the attractive Hubbard model $U < 0$, where the determinant for the two spin species are equal and consequently their product is always positive. In the repulsive case at half-filling, both determinants always have the same sign, thus also leading to well defined Boltzmann weights. Although every study presented in this work is performed at half-filling, and will be consequently devoid of any sign problem, this important limitation of the method should be kept in mind.

1.3.3.2 Boundary conditions

Because the DQMC algorithm computes properties of a finite cluster, a choice has to be made about the boundary conditions (BC). Even though any choice leads to the same result in the thermodynamic limit, the choice of periodic boundary conditions allows in general a better convergence. Periodic conditions allow the choice of a phase factor at each boundary, which once again does not affect the computed physical properties for an arbitrarily large cluster.

The real-space correlations computed by our algorithm can be equivalently computed in the reciprocal momentum-space by way of a numerical Fourier transform. All the information about spatial correlations will then be described within the first Brillouin zone, which in the case of the square lattice belongs to $\{k_x, k_y\} \in [-\pi, \pi[^2$. The number of *k-points* sampled in this interval is equal to the number N of sites of the cluster under consideration. Increasing the size of the cluster thus improves the sampling of the Brillouin zone.

The effect of changing the phase factors at the boundaries is to shift the position of the k-points in the Brillouin zone. By averaging independent simulations performed under different choices of boundary conditions, it is therefore possible to increase the number of points sampled in the momentum-space at a linear numerical cost, better than by increasing the size of the cluster (whose numerical cost scales as N^3) [12]. This is illustrated in Fig.1.3, in which the k-points for a small $N = 6 \times 6$ cluster are drawn for four different choices of boundary conditions.

1.4 Measurement of physical quantities

1.4.1 Static and dynamical measurements

A central quantity in statistical physics is the two-point correlator called Green's function, which is the response function to an elementary excitation. In DQMC, the Green's function can be easily extracted from the matrices used

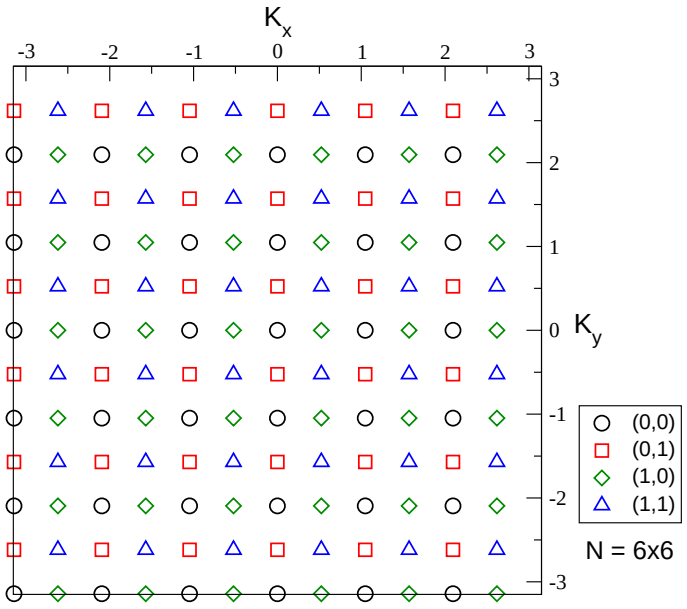

Figure 1.3: k-points in the first Brillouin zone of a $N = 6 \times 6$ square lattice. The four types of symbols specify the type of boundary condition (b_x, b_y) chosen, $b_\alpha = 0$ corresponding to periodic BC and $b_\alpha = 1$ to anti-periodic BC. Averaging results over different sets of BC allows a better sampling of the momentum-space.

to perform the stochastic evolution:

$$G^{\sigma}_{i,j} = \langle c_{i,\sigma} c^{\dagger}_{j\sigma} \rangle = \left(M^{-1}_{\sigma} \right)_{ij} . \tag{1.38}$$

For instance, the kinetic energy can be computed straightforwardly from the Green function:

$$\langle \hat{\mathcal{H}}_0 \rangle = \langle \sum_{\langle i,j \rangle, \sigma} t_{i,j} (h^{\dagger}_{i,\sigma} h_{j,\sigma} + h.c.) \rangle = \sum_{\langle i,j \rangle, \sigma} t_{i,j} (G^{\sigma}_{i,j} + G^{\sigma}_{j,i}). \tag{1.39}$$

General physical properties are determined by way of correlation functions of observables $\hat{\mathcal{O}}$

$$C(r) = \langle \hat{\mathcal{O}}_{i+r} \hat{\mathcal{O}}^{\dagger}_{i} \rangle - \langle \hat{\mathcal{O}}_{i+r} \rangle \langle \hat{\mathcal{O}}^{\dagger}_{i} \rangle, \tag{1.40}$$

where $\langle \cdot \rangle$ is the statistical average in the grand-canonical ensemble. Such correlation functions provide information about how an elementary perturbation at a site will affect the state of another site located at a distance r. Since in our definition we subtracted the uncorrelated value, the correlation function vanishes when the observable does not couple the distant sites.

Evaluating from the Green function the expectation value of physical quantities that involve more than two fermionic operators is made straightforward by using Wick's theorem. The latter gives the rules how to write such expectation values as a sum of products of two-point correlation functions. In the case of correlation functions involving four fermionic operators, it writes

$$\langle c^\dagger_{i,\alpha} c_{j,\beta} c^\dagger_{k,\gamma} c_{l,\delta} \rangle = \delta_{\alpha\beta}\delta_{\gamma\delta}(\delta_{ij} - G^\alpha_{j,i})(\delta_{kl} - G^\alpha_{l,k}) + \delta_{\alpha\delta}\delta_{\gamma\beta}(\delta_{il} - G^\alpha_{l,i})G^\alpha_{j,k}.$$

1.4.1.1 Time-dependent measurements

As we noted in a previous section, Quantum Monte Carlo methods account for quantum fluctuations by considering an additional "imaginary time" dimension. It is therefore possible to measure correlations at different imaginary times, in particular the Green function $\langle c^\dagger_{i,\sigma}(\tau) c_{j,\sigma}(0) \rangle$. By applying the Wick theorem, it is then possible to compute the imaginary time dependence of any observable.

The interest of computing time-dependent correlation functions stems from the possibility of extracting from them information about the real-time correlations (and consequently the energy spectrum), by means of the *analytic continuation* we shall briefly review below.

1.4.2 Long-range order

A physical system can be driven from a state to another upon changing a parameter such as pressure, chemical doping, external electric or magnetic field, etc., this phenomenon being called a phase transition. Temperature can also drive a thermal phase transition by increasing the thermal fluctuations in the system. Two phases of matter can in general be distinguished by a quantity that takes a finite value in one phase and vanishes in the other, the order parameter. For instance, an external magnetic field can align the disordered moments in a paramagnet, leading to a ferromagnetic order that breaks the rotational invariance of the moments. The order parameter is, in that case, the magnetization of the system. Such a transition is due to an external field that changes the symmetry of the hamiltonian and consequently drives an explicit symmetry breaking. When a transition breaks the symmetry of the hamiltonian in the absence of an external field, a spontaneous symmetry breaking occurs, an example being the order to disorder transition of a ferromagnet upon increasing the temperature. Some phase transitions can also occur with no symmetry breaking.

The order parameter that characterizes the transition is not always straightforward to determine. A way to characterize ordered phases is to look at the

spatial Fourier transform of real-space correlation functions, known as structure factors. We will be mostly interested in magnetic order, which will be determined through the magnetic structure factor $S(\mathbf{k})$:

$$\begin{cases} S(\mathbf{k}) = \frac{1}{N} e^{i\mathbf{k}\cdot\mathbf{R}} S(\mathbf{R}), \\ S(\mathbf{R}) = \frac{1}{3N} \sum\limits_{\alpha=\{x,y,z\}} \sum\limits_{\mathbf{r}} \langle \sigma^{\alpha}_{\mathbf{r}+\mathbf{R}} \sigma^{\alpha}_{\mathbf{r}} \rangle. \end{cases} \tag{1.41}$$

where we introduced the three spatial components of the spin operators:

$$\begin{cases} \sigma^{x}_{\mathbf{r}} = c^{\dagger}_{\mathbf{r}\uparrow} c_{\mathbf{r}\downarrow} + c^{\dagger}_{\mathbf{r}\downarrow} c_{\mathbf{r}\uparrow} \\ \sigma^{y}_{\mathbf{r}} = i(-c^{\dagger}_{\mathbf{r}\uparrow} c_{\mathbf{r}\downarrow} + c^{\dagger}_{\mathbf{r}\downarrow} c_{\mathbf{r}\uparrow}) \\ \sigma^{z}_{\mathbf{r}} = c^{\dagger}_{\mathbf{r}\uparrow} c_{\mathbf{r}\uparrow} - c^{\dagger}_{\mathbf{r}\downarrow} c_{\mathbf{r}\downarrow}. \end{cases} \tag{1.42}$$

Ferromagnetism is then seen as a peak in the magnetic structure factor at the wave-vector $\mathbf{k} = \mathbf{0}$, and antiferromagnetism as a peak at $\mathbf{k} = \pi$. It is useful to introduce a notation for the important particular point that characterizes antiferromagnetism,

$$S^{\mathrm{af}} \equiv S(\pi). \tag{1.43}$$

Complex types of order will lead to more intricate structures. Inhomogeneities in the charge distribution can equivalently be determined by way of a charge structure factor.

1.4.3 Analytic continuation

In the non-relativistic formalism the evolution of a quantum system described by a wave function $|\Psi\rangle$ is determined by the Schrödinger equation

$$i\hbar \frac{\partial}{\partial t} |\Psi\rangle = \hat{\mathcal{H}} |\Psi\rangle . \tag{1.44}$$

This leads to a time-dependent solution that reads in the basis of eigenstates of the Hamiltonian $\{|n\rangle\}$ as the linear sum of oscillating terms of frequency $E_n/\hbar$, where E_n is an eigenenergy and $\hbar$ the reduced Planck constant:

$$|\Psi(t)\rangle = |\Psi_0\rangle \, e^{-it\hat{\mathcal{H}}/\hbar} = \sum_n \langle n|\Psi_0|n\rangle e^{-itE_n/\hbar}, \tag{1.45}$$

with $|\Psi_0\rangle \equiv |\Psi(t=0)\rangle$. This evolution in time bears a formal -and deep- resemblance to the probability distribution of a statistical system at equilibrium. (For the sake of simplicity we consider here the canonical ensemble case.)

$$\langle \hat{O} \rangle_0 = \sum_n \frac{1}{Z} \langle n|\hat{O}|n\rangle e^{-\beta E_n}; \qquad Z \equiv \frac{1}{\sum_n e^{-\beta E_n}}, \quad \beta \equiv k_B T. \tag{1.46}$$

The similarity is evidenced by performing a Wick rotation $it/\hbar \to \beta$, that replaces the real time of the quantum mechanical system by the inverse temperature of the equilibrium statistical ensemble. It makes clear why the somewhat artificial dimension added in Quantum Monte Carlo (or equivalently in the Path-integral formulation) is called an imaginary time. But it also has the foremost practical consequence of allowing the evaluation of spectral properties of our statistical system.

In QMC, one can access correlation functions in imaginary time $C(\tau)$, for example the time dependent Green's function[1]:

$$G^{\sigma}_{i,j}(\tau) = \langle c_{i,\sigma}(\tau) c^{\dagger}_{j\sigma}(0) \rangle \tag{1.47}$$

Under some mathematical assumptions such as the analyticity of the correlation function, this function of a real variable admits a continuation over the whole complex plane that is uniquely determined by its expression on the real axis. This allows us to relate the correlation function to a "spectral function" $A(\omega)$.

We want to compute the time-dependent correlation function of an operator $\hat{O}$, which is

$$\begin{aligned} C(\tau) &= \langle \hat{O}(\tau)\hat{O}^{\dagger}(0) + \hat{O}^{\dagger}(\tau)\hat{O}(0) \rangle \\ &= \frac{1}{Z} \mathrm{Tr}\left[e^{-\beta H} \left(\hat{O}(\tau)\hat{O}^{\dagger}(0) + \hat{O}^{\dagger}(\tau)\hat{O}(0) \right) \right] \\ &= \frac{1}{Z} \sum_{n} \langle n | \, e^{-\beta H} e^{\tau H} \hat{O} e^{-\tau H} \hat{O}^{\dagger} + e^{-\beta H} e^{\tau H} \hat{O}^{\dagger} e^{-\tau H} \hat{O} \, | n \rangle \\ &= \frac{1}{Z} \sum_{n,m} e^{-(\beta-\tau)E_n} e^{-\tau E_m} \left(\langle n | \, \hat{O} \, | m \rangle \langle m | \, \hat{O}^{\dagger} \, | n \rangle + \langle n | \, \hat{O}^{\dagger} \, | m \rangle \langle m | \, \hat{O} \, | n \rangle \right) \\ &= \frac{1}{Z} \sum_{n,m} \left(e^{-\beta E_n} e^{-\tau(E_m - E_n)} + e^{-\beta E_m} e^{-\tau(E_n - E_m)} \right) \left| \, \langle m | \, \hat{O}^{\dagger} \, | n \rangle \, \right|^2, \end{aligned} \tag{1.48}$$

where $|n\rangle$ and $|m\rangle$ are eigenstates of the Hamiltonian.

By performing a Fourier transform one obtains

$$\begin{aligned} C(\omega) &= \int_0^{\beta} d\tau e^{-i\omega\tau} C(\tau) \\ &= \frac{1}{Z} \sum_{n,m} \frac{e^{-\beta E_n} + e^{-\beta E_m}}{\omega + E_n - E_m + i0^+} \left| \langle m | \hat{O} | n \rangle \right|^2. \end{aligned} \tag{1.49}$$

[1] The static Green's function $G(0)$ was defined in Equation (1.38).

We then define the spectral function

$$\begin{aligned} A(\omega) &= -\frac{1}{\pi}\mathrm{Im}C(\omega) \\ &= \frac{1}{Z}\sum_{n,m}\left(e^{-\beta E_n}+e^{-\beta E_m}\right)\left|\langle m|\hat{O}|n\rangle\right|^2\delta(\omega+E_n-E_m) \\ &= \frac{1+e^{-\beta\omega}}{Z}\sum_{n,m}e^{-\beta E_n}\left|\langle m|\hat{O}|n\rangle\right|^2\delta(\omega+E_n-E_m), \end{aligned} \tag{1.50}$$

which verifies the sum rule

$$\int_{-\infty}^{+\infty} d\omega A(\omega) = 1, \tag{1.51}$$

$$C(\tau) = \int_{-\infty}^{+\infty} d\omega A(\omega)\frac{e^{-\tau\omega}}{1+e^{-\beta\omega}}. \tag{1.52}$$

$A(\omega)$ is a function of energy and determines the available excitations corresponding to the real-time correlation function. When one disposes of statistically noisy data, inverting the above relation is a mathematically ill-posed problem and the simple possibility of fitting the integral of a trial function $A(\omega)$ to $C(\tau)$ does not lead to satisfactory results. The Maximum Entropy Method (MaxEnt) [6, 13] addresses that question by adding a constraint that enforces the likelihood of the solution by taking into account both the goodness of fit χ^2 and the information entropy S. The likelihood of a given spectral function A is then given by

$$P[A] \sim e^{\alpha S-\chi^2}, \tag{1.53}$$

where α is a positive parameter that tunes the respective importance of minimizing the goodness of fit and maximizing the information entropy. In practice, one averages the spectra obtained with a given distribution of α [13]. This method has been more recently extended into the more general stochastic analytic continuation approach. The latter consists of generating a solution "thermally" averaged over different trial spectral functions, the Boltzmann weight of each function corresponding to its goodness of fit [14, 15].

1.4.4 Spectral functions

Spectral functions provide information about the excitations available to the many-body system, thus bringing insight into the properties of the underlying phases. Throughout this work we will be particularly interested in the single-particle and the spin-spin spectral functions.

1.4.4.1 Single-particle excitations

The single-particle spectral function $A(\omega, \mathbf{k})$ can be extracted from the time-dependent Green function:

$$G(\tau, \mathbf{k}) = \int_0^\beta d\omega A(\omega, \mathbf{k}) \frac{e^{-\tau\omega}}{1 + e^{-\beta\omega}}. \tag{1.54}$$

An important point is that this quantity is experimentally accessible by means of angle-resolved photo-emission spectroscopy (ARPES). This technique is based on photo-emission spectroscopy: when light falls on a sample, photons can be absorbed only at energies corresponding to the energy difference between available excited and occupied states. The density of states of the material considered can consequently be deduced from the absorption spectrum because of the law of conservation of energy. Refinement of this method allows to extract the momentum dependence of this absorption, by probing the angular dependence of the absorption and considering the conservation of total momentum.

1.4.4.2 Spin-wave excitations

Spin excitations can be probed experimentally by scattering neutrons, which have a typical wavelength comparable to the interatomic distance in materials and thus are diffracted [16]. Because they are neutral particles, neutrons can penetrate into the sample and reveal different properties of the bulk. In particular, magnetic order can be accessed because the spin of the incident neutron interacts with the magnetic degrees of freedom of the material. Inelastic scattering allows to access the momentum dependence of these excitations, providing the dynamic structure factor $S(\omega, \mathbf{k})$.

1.4.4.3 Finite-size effects on the DOS

Finite-size effects can lead to undesirable effects on the spectra obtained by way of analytic continuation, in particular at $U = 0$ as illustrated in Fig.1.4 for the single-particle spectral function $A(\omega)$. Because of the high symmetry of the lattice, the eigen-energies of the hamiltonian take only a few values that are highly degenerate. The *exact* density of states for the finite cluster thus displays only a few peaks, differing dramatically from the smooth curve one obtains in the thermodynamic limit. Because the analytic continuation tends to prefer smooth solutions, it fails to reproduce the discrete spectrum. The result consequently differs from both the finite cluster exact solution and the thermodynamic spectrum. By the same token, artificial small gaps due to the discrete spectrum of the small cluster can appear in the extracted data.

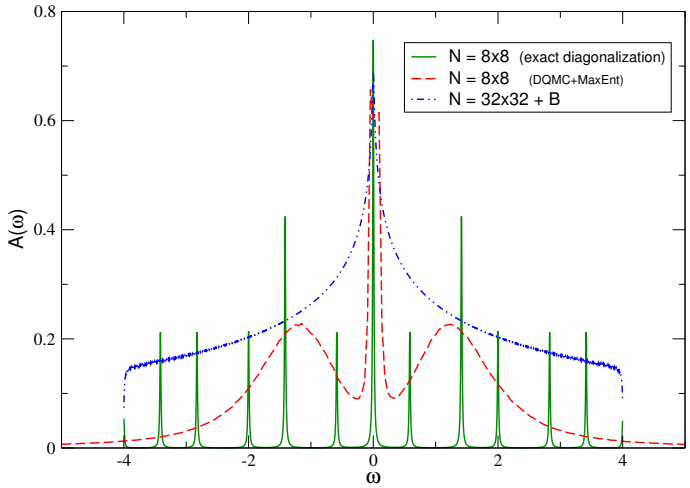

Figure 1.4: On a $N = 8 \times 8$ cluster, symmetries lead to highly degenerate spectra with only few peaks (continuous line). Analytic continuation of these discrete spectra gives the correct peak at the Fermi energy but spurious features are observed (dashed line). Exact diagonalization on a large cluster $N = 32 \times 32$ in which the degeneracy is lifted by a small magnetic field gives, in comparison, spectra close to the one expected in the thermodynamic limit.

The analytic continuation of clusters of different sizes can help detect such a problem. However, interactions between fermions tend to lift the degeneracy of the spectrum and therefore suffer from finite size effect in a much lesser extent than the non-interacting case,

1.4.5 Electrical conductivity

Information about the transport properties can be obtained by computing the electrical conductivity. We first introduce the current operator in the $\hat{x}$ direction at site $\mathbf{l}$

$$j_x(\mathbf{l}, \tau) = e^{H\tau} \left(it \sum_{\sigma} \left[c^{\dagger}_{\mathbf{l}+\hat{x},\sigma} c_{\mathbf{l},\sigma} + c^{\dagger}_{\mathbf{l},\sigma} c_{\mathbf{l}+\hat{x},\sigma} \right] \right) e^{-H\tau}. \tag{1.55}$$

In momentum space, the current-current correlation function can then be defined as

$$\Lambda_{xx}(\mathbf{k}, i\omega_n) = \frac{1}{N} \sum_{\mathbf{l}} \int_0^{\beta} d\tau \langle j_x(\mathbf{l}, \tau) j_x(\mathbf{0}, 0) \rangle e^{i\mathbf{k}\cdot\mathbf{l}} e^{-i\omega_n \tau} \tag{1.56}$$

where we introduced the Matsubara frequency $\omega_n = \frac{2\pi n}{\beta}$.

The direct current (dc) conductivity we are interested in is defined from the static component of the imaginary part of the analytic continuation of the current-current correlation into real frequencies

$$\sigma_{dc} = \frac{1}{\omega}\mathrm{Im}\Lambda_{xx}(\mathbf{q}=0,\omega). \tag{1.57}$$

The fluctuation-dissipation theorem relates the current-current correlation we obtain in DQMC to its real frequency dependence through a bosonic kernel:

$$\Lambda_{xx}(\mathbf{q},\tau) = \int_{-\infty}^{+\infty} \frac{d\omega}{\pi} \frac{e^{-\tau\omega}}{1-e^{-\beta\omega}} \mathrm{Im}\Lambda_{xx}(\mathbf{q},\omega). \tag{1.58}$$

Although it is, in principle, possible to invert numerically this Laplace transform by way of the Maximum Entropy Method or a related technique, it can be convenient to estimate the dc conductivity from its low frequency dependency $\sigma_{dc} \approx \frac{1}{\omega}\mathrm{Im}\Lambda_{xx}(\mathbf{0},\omega)$, this relation being valid at low temperature [17, 18]. By integrating the previous relation one finally obtains:

$$\sigma_{dc} = \frac{\beta^2}{\pi}\Lambda_{xx}(\mathbf{0},\tau=\frac{\beta}{2}). \tag{1.59}$$

1.5 Assessment of the theoretical framework

The three studies we present below have some limitations. First, the Hubbard model limited to nearest-neighbor hopping and on-site interaction is a minimal description of interacting fermions. In spite of the rich physics it generates, the possibility of including a Hund coupling is complicated because of the fermionic sign problem that appears when next-nearest-neighbor interactions are included in the hamiltonian [19]. Key branches of the field will thus escape our scope, like the itinerant ferromagnetism metal phases that appear when Hund rules are accounted for. Even for this simple model, the sign problem will also restrict us to the half-filling case, while electron and hole dopings are known to engender unconventional properties, like "high-T_c" superconductivity. The cubic lattice is convenient since it has only one site per unit cell, and more importantly for not being geometrically frustrated. Biparticity favours ordered phases, and the "exotic" liquid states found in frustrated lattices (like the triangular and Kagome lattices) will not be accessible. Another major peculiarity this lattice shows at half-filling is the divergence of the antiferromagnetic susceptibility owing to the nesting of the Fermi surface, which leads to a magnetic Mott insulator at arbitrary small Coulomb repulsion. This scenario is obviously not a generic one, and comparison to different

geometries with finite critical interaction would have been beneficial. However, these limitations should be balanced against the following considerations.

In contrast with spin models, the Hubbard hamiltonian takes into account the charge fluctuations inherent to finite interaction. This point is fundamental to capture the interplay of transport and magnetism that underlies the physics related to the "Kondo effect", in particular the broad field of heavy-fermions related physics. While Kondo-Heisenberg hamiltonians allow to work within a sub-space of the Hubbard hamiltonian and therefore to simplify the complexity, charge fluctuations can not be neglected for mildly interacting systems.

Few alternative techniques are available for the study of strongly correlated electronic systems. Most of the exact results known for the Hubbard model apply to the one-dimensional case, for which real-space density-matrix renormalization techniques are also essentially restricted. On the other extreme stand mean field theories, which are exact in the limit of infinite dimensions, but are often unable to describe the phases that exist in low dimension. Belonging to this category is dynamical mean-field theory (DMFT) [20], which is able to compute self-consistently the dynamical properties of the quantum problem at the cost of neglecting spatial correlations in its single-site version. Cluster extensions of DMFT offer promising prospects, but the small size of the clusters considered imposes a spatial cut-off whose effects are cumbersome to evaluate a priori.

On the other hand, Determinant QMC can, in principle, generate exact results for finite clusters containing hundreds of sites. Working in the grand-canonical ensemble allows to study the temperature dependence of the phase diagram and capture transitions driven by thermal fluctuations. Making the choice of avoiding any sign problem allows to attain low temperatures and to converge quickly. It is therefore possible to explore broad regions of the phase space, and to reach clusters large enough so to perform finite-size extrapolation.

Chapter 2

Correlations in a band insulator

2.1 Motivations

Band theory allows us to explain the sharp distinction of the electronic properties in materials between metals and insulators, depending on the filling of the band. When an electronic band is entirely filled, a finite energy is needed in order to access the first available excited state, leading to insulating properties. On the other hand, when the band is only partially filled excitations are accessible at an arbitrary small energy cost, thus displaying metallic properties. Materials being described within that framework offer few opportunities for information technology applications since their conductivities are essentially not tunable. However, the intermediate case of semiconductors in which the band gap is small has allowed the development of integrated electronics in which logical properties can be obtained from interfaces of doped metal-oxyde semiconductors. As the miniaturization of transistor integration following the exponential "Moore's law" [21] approaches the limit of few atomic sizes where quantum effects become predominant, new ways of controlling the electronic properties of materials are needed in order to ensure further progress in the field of information technology. In that context, it is natural to look for materials displaying phase transitions that could be controlled by simple experimental parameters such as electric or magnetic fields. In the last decades, much attention has been focused on metal-insulator transitions driven by local electron-electron interactions, in particular the Mott transition that occurs in the Hubbard model as we previously discussed. However, other types of transitions have more recently been investigated and offer promising prospects.

2.1.1 Anderson-Mott transition

A crystal is not necessarily made of identical sites and can therefore include some degree of disorder. A typical realization of such a situation is when an alloy contains some proportion of impurities or defects randomly distributed in the crystal. This situation can be described by the Anderson model, a tight-biding hamiltonian which allows the energy of the sites to vary locally according to a given distribution of width Δ_μ. The electronic properties of this

model are based on the competition between the completely delocalized plane-waves found in the perfect crystal and the tendency of electrons to localize at the sites of lower energy, sometimes leading to an insulating transition called the Anderson localization (or strong localization) [22]. Dimensionality is a crucial factor in this model: in one dimension the localization is triggered as soon randomness is allowed $\Delta_\mu \neq 0$, while a metal-insulator transition has been reported in three dimension by theoretical and experimental works.

In the two-dimensional case, the localization occurs only marginally. It is thus relevant to ask whether an on-site repulsion could screen the disorder and lead to a metallic state, a question that has been addressed early on by Anderson [23] and has been the subject of considerable investigation since then [24, 25, 26]. Quantum Monte Carlo studies have found signs of a such a transition at finite temperature [27, 28], although it has been argued a metallic state can not survive at zero temperature in the ground-state [29, 30]. In the limit of infinite dimension, single-site DMFT has provided several results that demonstrate a metal-insulator transition driven by the correlations at intermediate interaction [31, 32, 33].

Even though we shall not consider the role of disorder in the present work, it is important to keep in mind the variety of ways in which a non-interacting insulating state can be achieved and the fact that the role of including correlation in such models remains highly controversial.

2.1.2 Bilayer models

Another way to realize a band insulator is to consider a bilayer Hubbard model in which the orbitals are connected through a local hopping term V. The effect of the latter is to split the two original bands, which overlap at small V. In the non-interacting limit, this model is consequently characterized by the opening of a band gap at a critical V_c from which singlet dimers are formed across the bands, the finite energy needed to break these pairs being the width of the gap.

Determinant QMC studies have yielded a phase diagram in which three phases can be distinguished, namely a paramagnetic metal at small interaction, and two insulating phases distinguished by the presence or absence of magnetic order [34, 35]. In spite of displaying no intermediate metallicity in between these two insulating phases, this model demonstrates that bilayer models can lead to richer phase diagrams than the single metal-insulating transition known in the single-band Hubbard model. The pair excitation spectra of a similar model was recently explored within a DMFT study [36], in which the role of double occupancy in the metallicity of the doped phases was underlined.

Models including more than two orbitals were also shown to display complex phase diagram. For example, a three-band Hubbard model, including spin-orbit interaction and Hund's rules coupling, was found to have an intermediate band insulating phase in between the Mott-metal transition [37].

2.1.3 The ionic Hubbard model

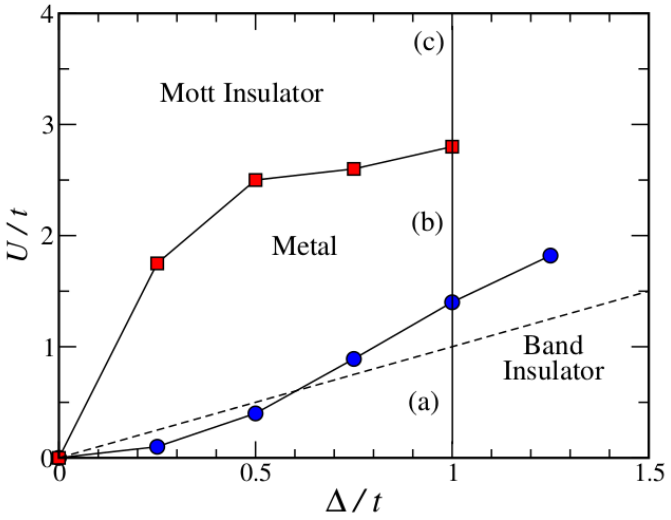

Figure 2.1: Phase diagram of the ionic Hubbard model as obtained from DQMC simulations. At a given gap Δ, enhancing the interaction U first drives a transition from a band insulator to a correlated metal, before the system goes to a Mott insulating phase. The dashed line is the strong coupling limit ($t = 0$). From [38].

Another possibility is to consider the effect of local interactions in a band insulator. This case has been extensively studied in the framework of the Ionic Hubbard Model [39], in which adjacent sites have a difference in chemical potential Δ due to crystal field splitting. In the non-interacting limit, this model has a band gap Δ owing to the energy cost when an electron hops from one site to another. Interest in this model was first triggered by organic compounds [40] that can be described in a minimal way by the one-dimensional version of the IHM [41, 42, 43]:

$$\begin{aligned} \hat{\mathcal{H}}_{\mathrm{IHM}} = - \quad & t \sum_{\langle i,j\rangle,\sigma} (c^{\dagger}_{i,\sigma} c_{j,\sigma} + c^{\dagger}_{j,\sigma} c_{i,\sigma}) \\ + \quad & U \sum_{i} n_{i,\uparrow} n_{i,\downarrow} + \sum_{i,\sigma} ((-1)^{i} \frac{\Delta}{2} - \mu) n_{i,\sigma}. \end{aligned} \tag{2.1}$$

The two-dimensional version of this model has then been studied and led to controversial results. Intermediate phases in between the band insulating and the Mott insulating states were indeed found, but the nature of this phase was claimed to be metallic by DMFT [44] and DQMC [38, 45], while a cluster DMFT study found it to be insulating with bond order [46]. An experimental illustration of the metal-insulator transition found in the 2D IHM was demonstrated on the compound $SrRu_{1-x}Ti_xO_3$ by photoemission spectroscopy [47].

2.2 A correlated band insulator

The models we have briefly reviewed in the former section show us there are multiple ways to approach the question of correlated insulators. In the last example, the Ionic Hubbard model, a non-interacting insulating phase stems from the ionicity of the system. Band insulating properties can alternatively arise from electronic hybridization, as in materials like FeSi [48] or $FeSb_2$ [49] which display transport properties similar to Kondo insulators while they do not belong to the $4f$ intermetallic compounds. A DMFT work proposed a description of these materials in terms of correlated covalent insulators described by a Hubbard hamiltonian [50], in which the local orbitals are half filled in contrast to the ionic models, and found good agreement with experimental data. Another subsequent DMFT paper by Sentef *et al.* on such a correlated covalent band insulator found an intervening metallic phase in between the BI and MI upon increasing the Coulomb repulsion [51].

Motivated by these results, we study in what follows the effect of correlation in a covalent insulator similar to the one proposed by Sentef. Interestingly, the non-interacting Hamiltonian has exactly the same dispersion relation as the IHM, allowing us to pinpoint the origin of the differences in the phase diagrams of both models.

2.2.1 Hamiltonian

The band structure of a non-interacting tight-binding hamiltonian is determined by its particular pattern of hopping terms. The two-dimensional honeycomb and square lattices -in which each site is connected to three or four nearest neighbors respectively- are textbook cases of the dramatic role played by the number of links per site. The dispersion relation in the former is characterized by the bonding and anti-bonding bands being connected at single points with linear dispersion in their vicinity, while the latter shows in the half-filled case a divergence in the density of states at the Fermi level and a nesting of the Fermi surface leading to an antiferromagnetic instability. Beyond these simple

examples, it is possible to "engineer" a specific band structure in a particular geometry by setting non-isotropic hoppings, or allowing connections between non-nearest-neighbor sites.

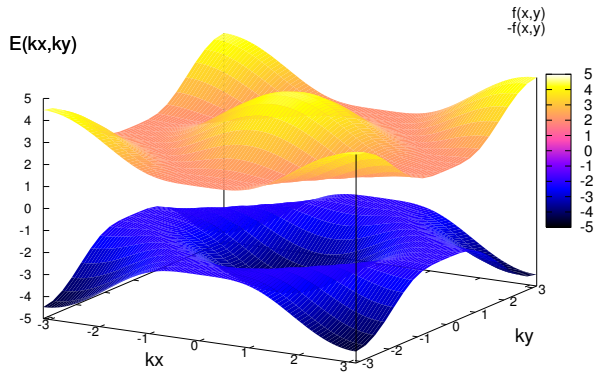

Figure 2.2: Non-interacting dispersion relation of the Hubbard bilayer with opposite in-layer hopping signs. At half-filling the band gap minimum $\Delta = 2V$ coincides with the square Fermi surface.

In principle many choices are possible in order to realize a band insulator. We chose the following bilayer hamiltonian:

$$\begin{aligned}\hat{\mathcal{H}} = & - \sum_{\langle \mathbf{jk}\rangle,l,\sigma} t_l (c^\dagger_{\mathbf{j},l,\sigma} c_{\mathbf{k},l,\sigma} + c^\dagger_{\mathbf{k},l,\sigma} c_{\mathbf{j},l,\sigma}) - V \sum_{\mathbf{j},\sigma} (c^\dagger_{\mathbf{j},1,\sigma} c_{\mathbf{j},2,\sigma} + c^\dagger_{\mathbf{j},2,\sigma} c_{\mathbf{j},1,\sigma}) \\ & + U \sum_{\mathbf{j},l} (n_{\mathbf{j},l,\uparrow} - \frac{1}{2})(n_{\mathbf{j},l,\downarrow} - \frac{1}{2}) - \sum_{\mathbf{j},l,\sigma} \mu_l n_{\mathbf{j},l,\sigma}. \end{aligned} \tag{2.2}$$

Electrons are labelled by their coordinate at the site $\mathbf{j}$ of the layer l on a cubic lattice. The chemical potential μ is set to zero so the system is at half-filling, while the on-site Coulomb interaction is chosen to be repulsive $U > 0$. In-plane hopping have opposite signs, $t_1 = -t_2 \equiv t$, and t will be taken as the unit of energy. The non-interacting dispersion relation reads $E_{\mathbf{q}} = \pm\sqrt{\varepsilon^2_{\mathbf{q}} + V^2}$, where $\varepsilon_{\mathbf{q}} = -2t(\cos(q_x)+\cos(q_y))$. It has a band gap at any inter-plane hopping $V > 0$, and the gap reaches the minimum width $2V$ along the Fermi surface parametrized in momentum-space by $k_y = \pm\pi(1 - |k_x|)$. The bandwidth is a monotonically decreasing function of the perpendicular hopping: $W = (V^2 + 16t^2)^{1/2} - V$. In the decoupled case $V = 0$ each plane is known to show a magnetic instablility due to the nesting of the Fermi surface of the square lattice, leading to AF long-range order (LRO) at any $U > 0$.

This system has been previously studied within the dynamical mean-field theory (DMFT) formalism [20], although one should note that semi-circular electronic bands were used. They found a transition from a band insulator to a correlated insulator when increasing U, with a coexistence region at low temperature. The signal for the transition was a discontinuity in the double occupancy. A main result of that paper is the shrinking of the single-particle gap upon increasing the on-site correlation when approaching the transition. One of our motivations for studying this system was to find a possible metallic phase around the insulator-insulator transition.

2.2.2 Preliminary phase diagram

The phase diagram is sketched qualitatively in Fig.2.3. In the infinite-U limit our system is indeed the bilayer Heisenberg model, which is known to display antiferromagnetic order up to a critical interlayer hybridization $V_c \approx 1.59$ beyond which singlet formation destroys magnetism [52, 53]. No magnetic transition is thus expected beyond this value.

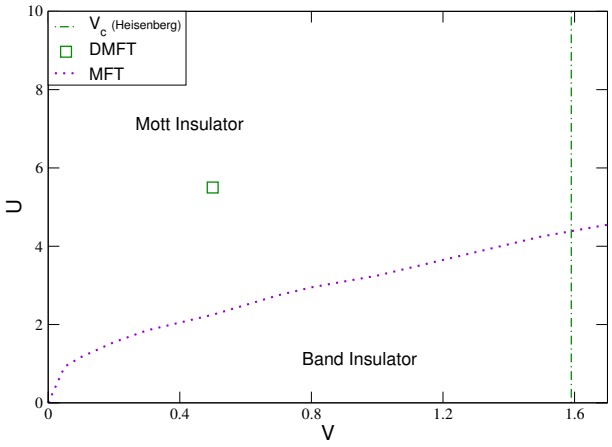

(a) tata

Figure 2.3: Preliminary phase diagram in the $V - U$ plane. The dotted line shows the phase boundary we found by way of MFT. The BI/MI transition obtained by DMFT at $V = 0.5$ is shown by the square symbol [51]. The Heisenberg critical hybridization, V_c, above which the transition to an ordered phase is prevented by singlet formation [53] is represented as a dashed line.

In order to draw a first boundary between the band insulating and Mott insulating phases, we performed a mean field calculation. In that framework the transition is characterized by the formation of local moments. The phase boundary we obtained is shown as a dotted line; at $V = 0.5$ the transition

is found to occur at a much weaker interaction than in DMFT. The Mott transition was studied in DMFT only at the value $V = 0.5$, where the critical interaction is $U \approx 5.5$.

2.3 Magnetism

An important property that was not accessible in the previous single-site DMFT work is magnetism. An onset of magnetic order is to be expected since as the interaction is increased the underlying band structure becomes less relevant and the model progresses toward the Heisenberg limit. However as previously noted, this magnetic transition happens only below a critical $V_c \approx 1.59$ beyond which well-formed pairs prevent the onset of magnetic order.

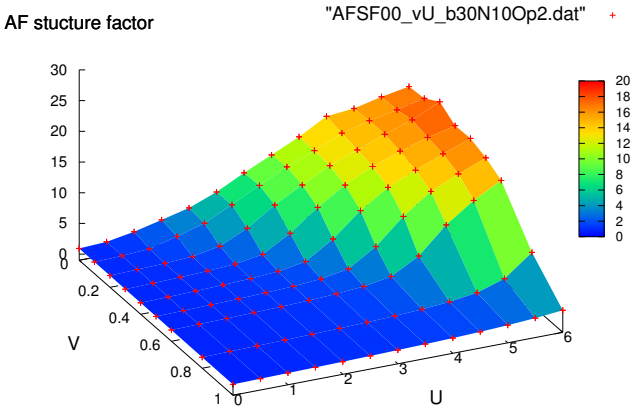

Figure 2.4: Antiferromagnetic structure factor in the $V - U$ plane, for a $N = 2 \times 10 \times 10$ cluster at inverse temperature $\beta = 30$. The interaction U_c from which magnetic order arises grows with the width of the gap $2V$. Finite-size effects smooth out the transition, hence the need to perform finite-size extrapolation in order to estimate where the thermodynamic transition takes place.

The antiferromagnetic structure factor (see Eq.(1.43)) in the $V-U$ plane is represented in Fig.2.4. As the non-interacting band gap increases the critical interaction needed to trigger the magnetic transition increases monotonically, reflecting the fact that the hybridization across the planes tends to destabilize the tendency toward order. The importance of temperature should be noted: while at $V = 0$ the system is made of two decoupled Hubbard planes and

magnetic order should thus be expected at any nonzero interaction $U > 0$, thermal fluctuations destroy this order and lead to a paramagnetic state at small finite U.

Going beyond these qualitative trends and determining the actual phase boundary requires us to perform finite-size scaling of the antiferromagnetic structure factor. We first focus on the $V = 0.5$ value. As shown in Fig.2.5 the transition can be located precisely and occurs around $U_c \approx 4.2$, which should be contrasted with the higher value $U \approx 5.5$ found in DMFT; this discrepancy can be explained by the fact that we take into account non-local correlations that contribute to the transition.

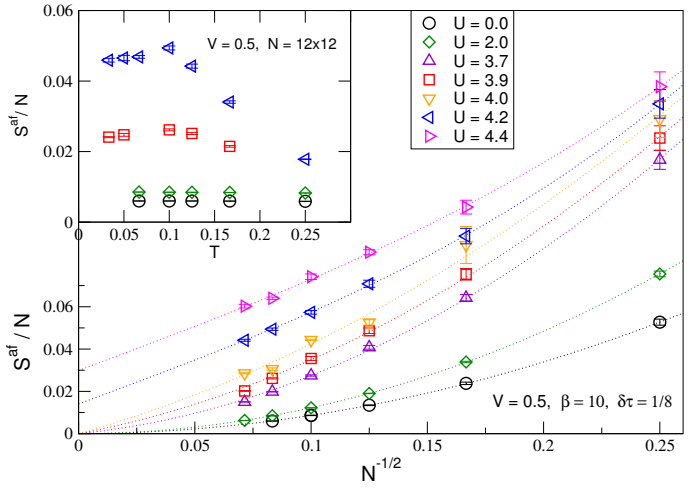

Figure 2.5: Main panel: Finite-size scaling of the AF structure factor at $V = 0.5$ for several values of the interaction U and at $\beta = 10$. The dotted lines are the polynomial fits to the data, showing the transition occurs in around $U_c = 4.1$. The inset shows the convergence at low temperature of four characteristic values of U, for the cluster size $N = 2 \times 12 \times 12$.

The inset in Fig.2.5 shows the AF structure factor dependence on temperature at a fixed size $N = 2 \times 12 \times 12$. While S^{af} (see Eq.(1.43)) shows no sensitivity to temperature in the disordered phase, high temperature destroy the magnetic order for points above the magnetic transition and the structure factor converges only below a critical temperature. In that example the $\beta = 10$ data seem to overestimate slightly the ground-state value, although this is not expected to shift significantly the critical interaction we found for the transition. However, determining the precise value of the order parameter at a given interaction would require to go to lower temperatures.

For larger V, the critical interaction needed for the onset of order grows larger and fluctuations make numerical simulations cumbersome. This is illus-

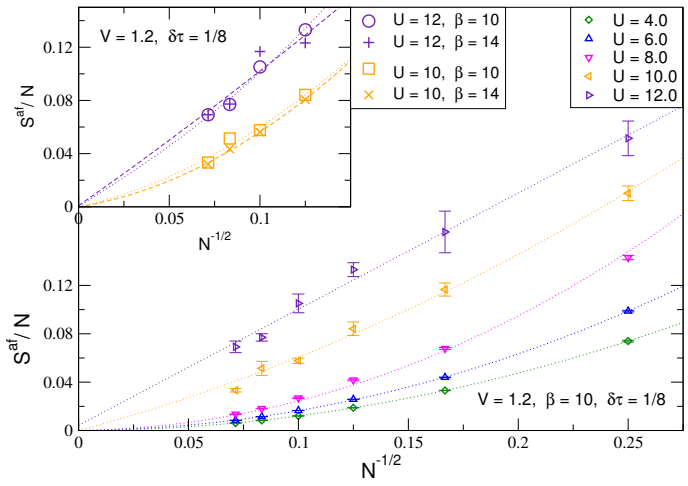

Figure 2.6: At $V = 1.2$ and $\beta = 10$ the system remains disordered up to $U = 12$, the maximum value of the interaction we could reach, although magnetism seems to be at the point of appearing. The inset shows no difference in the extrapolation is found upon slightly decreasing the temperature.

trated in Fig.2.6 for the case of $V = 1.2$. It shows that in spite of being larger than at $U = 10$, the structure factor does not extrapolate to a finite value in the thermodynamic limit at $U = 12$, even though the Heisenberg limit is known to be ordered. Upon further increasing U (Fig.2.7), the structure factor seems not to grow significantly anymore although large fluctuations make any strong statement difficult. Consequently, the magnetic boundary in our phase diagram will be limited to moderate values of U, the question of its detailed shape when approaching the Heisenberg limit being beyond the reach of our algorithm.

2.4 Local moments

Now that we determined the magnetic transition boundary we turn to the behavior of local moments m, which are related to the double occupancy d by (and using the z-component of the spin operator $\sigma^z_{\mathbf{j}}$ that was defined in Eq. (1.42)):

$$m = \frac{1}{N}\sum_{\mathbf{j}}\langle(\sigma^z_{\mathbf{j}})^2\rangle = 1 - \frac{2}{N}\sum_{\mathbf{j}}\langle n_{\mathbf{j}\uparrow}n_{\mathbf{j}\downarrow}\rangle = 1 - 2d. \tag{2.3}$$

Our interest was at first driven by the fact that DMFT characterizes the transition by a discontinuity in double occupancy. Even though we found this discontinuity to be an artifact, the derivative of double occupancy with respect

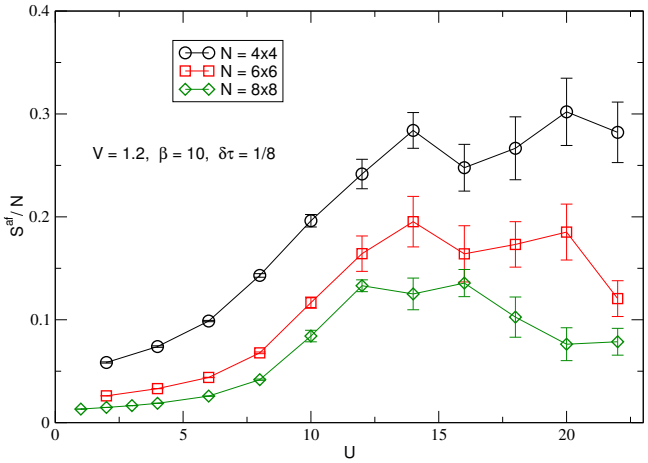

Figure 2.7: Antiferromagnetic structure factor at $V = 1.2$ and $\beta = 10$ up to $U = 22$ for small clusters. In comparison with the $U = 12$ extrapolation shown in Fig.2.6, it seems unlikely we could capture any magnetic transition within these parameters regime.

to the interaction is indeed a susceptibility and is then expected to characterize the transition.

Fig.2.8a shows that upon increasing the interaction the local moments undergo a monotonic increase from the uncorrelated value 1/2. For small values of V an inflexion point is observed that can be better distinguished as a maximum in the derivative $\partial m/\partial U$, as illustrated in Fig.2.8b. The position of these maxima can be located rather precisely, and for instance at $V = 0.5$ it indeed coincides within error bars with the critical interaction $U_c \approx 4.2$.

At large hybridization, for example at $V = 2.0$, no maximum is found in the derivative. This can be explained by the fact that we know from the Heisenberg model limit no magnetic transition will ever happen beyond $V_c = 1.59$, so no phase transition is expected there. In order to capture where this maximum vanishes we show a close-up view in Fig.2.8c. Surprisingly, the critical interaction at which the maximum occurs is reduced upon increasing the hybridization in the range $V = [1.0, 1.2]$, while no peak is visible for any U above $V \approx 1.2$. There is therefore a region of the phase diagram were the inflexion point of the moments does not match the magnetic transition anymore. Although we verified that the results have converged, it is numerically cumbersome to conclude whether the decoupling of the behavior of local moments from the magnetic ordering is an actual transition or a crossover. This opens the door to a possible intermediate featureless Mott insulating state in which no symmetry would be broken.

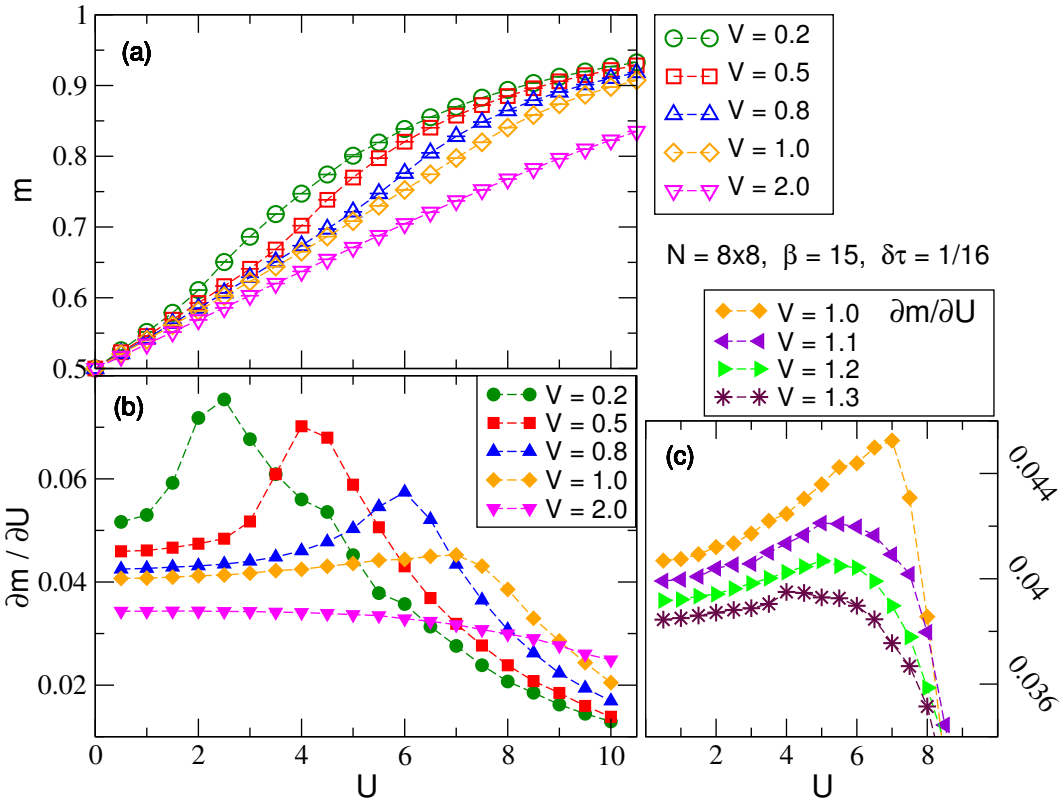

Figure 2.8: (a) Local moment m as a function of U for 8x8 layers at $\beta = 15$ (symbols). (b) first derivative of the local moment with respect to U, $\partial m/\partial U$, shows a peak at the transition to the Mott insulating state. (c) A close up view of (b) shows the peak is no longer present for any U above $V_c = 1.2$.

2.5 Spin correlations

The study of real space spin correlations brings further insight into the different regimes of the phase diagram. Fig. 2.9a shows the nearest-neighbor correlation across the layers $\langle \sigma_{j1} \cdot \sigma_{j2} \rangle$ as a function of U (see Eq.1.42 for the definition of the spin operator σ). The increase in absolute value of this correlation upon increasing V is a well-known feature of bilayer models that characterizes singlet bound-state formation leading to the destruction of magnetic order. Here we see that increasing the interaction also enhances short-ranged correlation (Fig. 2.9b). This can be interpreted as concomitant to the formation of local moments, as a reduced proportion of double occupancies and vacancies favours spin correlation. The evolution exhibits a kink for an interaction value that corresponds to that found for the magnetic transition, as well as the inflexion point in local moments. It is worth noting that within the magnetic phase the

increase of correlation is slower than in the paramagnetic phase, the correlation being even suppressed at intermediate V upon entering the Mott phase. This peculiarity can be understood as the competition between AFLRO and singlets.

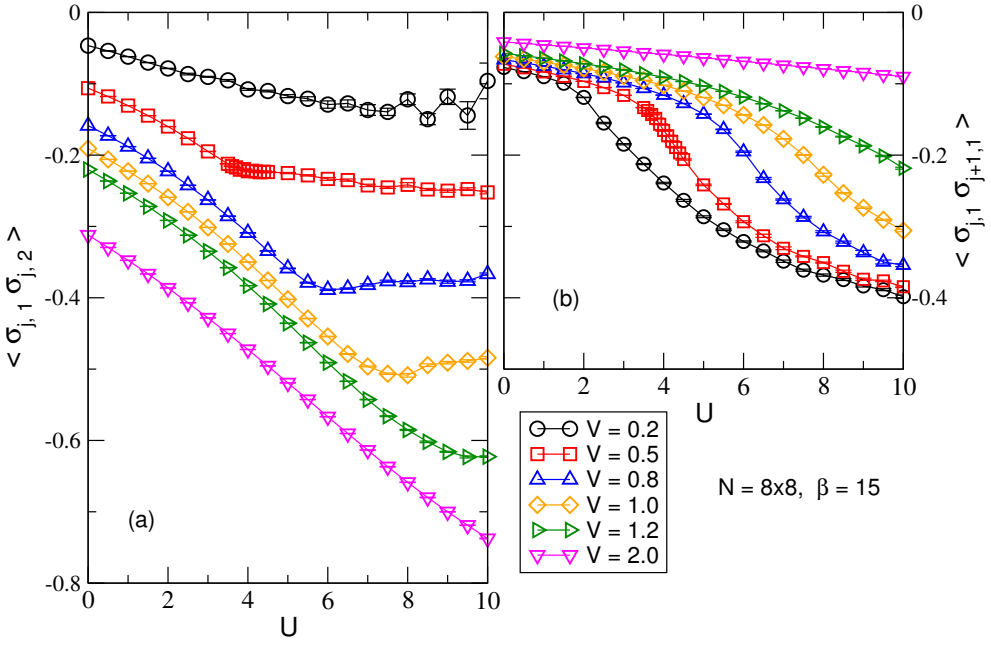

Figure 2.9: Nearest-neighbor real space spin-spin correlations (a) across the layers and (b) within an individual plane. At small $V < 1.2$ the correlations converge to finite values characterizing the magnetically ordered phase, while for large $V = 2.0$, the system is made of almost uncorrelated singlets.

The right panel Fig.2.9b presents the intra-plane real space nearest-neighbor spin correlations. This quantity decreases very slightly upon increasing U until the magnetic transition, where it sharply drops before saturating. At $V = 2.0$, where no transition is expected the correlation experiences no such drop and remains small at any U.

The comparison of the two panels gives us a hint of the discrepancy between our calculations and the single site DMFT study: at small U the correlation across the layers (left panel) grows faster than the in-plane correlation, indicating the difference in our study is more likely to be attributed to the inclusion of inter-layer short range correlations than to the short-ranged magnetic order within the planes.

2.6 Energy gaps and spectral functions

We now present results on the energy spectra of the correlated insulator. The single-particle gap $\Delta_{\rm sp}$ and the spin gap Δ_S will be extracted by exponential fits of the time-dependent correlation functions corresponding to these excitations, which clearly follows from the expression we obtained in Eq.(1.49). This method is illustrated in Fig.2.10 for the case of the single-particle gap.

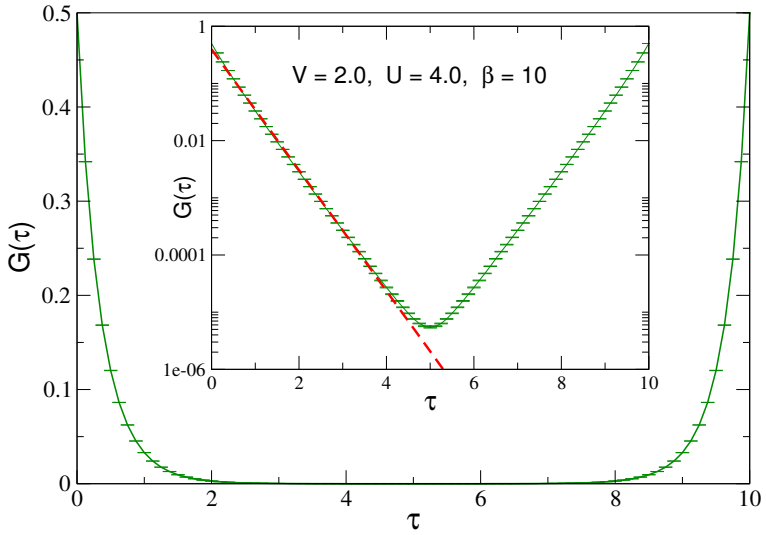

Figure 2.10: We obtain the single-particle gap by fitting the exponential decay of the time-dependent Green function. The latter is shown in the main panel on a linear scale, and in the inset on a semi-log scale. The red line corresponds to the fit that allows to extract the gap. Parameters are $U = 4.0$, $V = 2.0$ and $\beta = 10$.

Band insulators are characterized by displaying a gap to all excitations. In contrast, a Mott insulator at half filling is gapped to charge excitations due to the energy cost of double occupancy, but might have low-energy excitations in other sectors. In particular, magnetic long-range order is expected to allow long wavelength Goldstone modes with arbitrarily small energies in the thermodynamic limit. The behavior of gaps at the transition between a BI and a MI is therefore expected to be non-trivial, and intervening metallic phases were indeed previoulsy reported in both the IHM and the system we presently study.

We plot in Fig. 2.11a the dependence of both the single-particle gap and the spin gap upon increasing U, for three characteristic values of $V \in \{0.5, 1.0, 2.0\}$. These energy gaps were obtained by fitting the exponential decrease of local correlation in imaginary time obtained through our DQMC

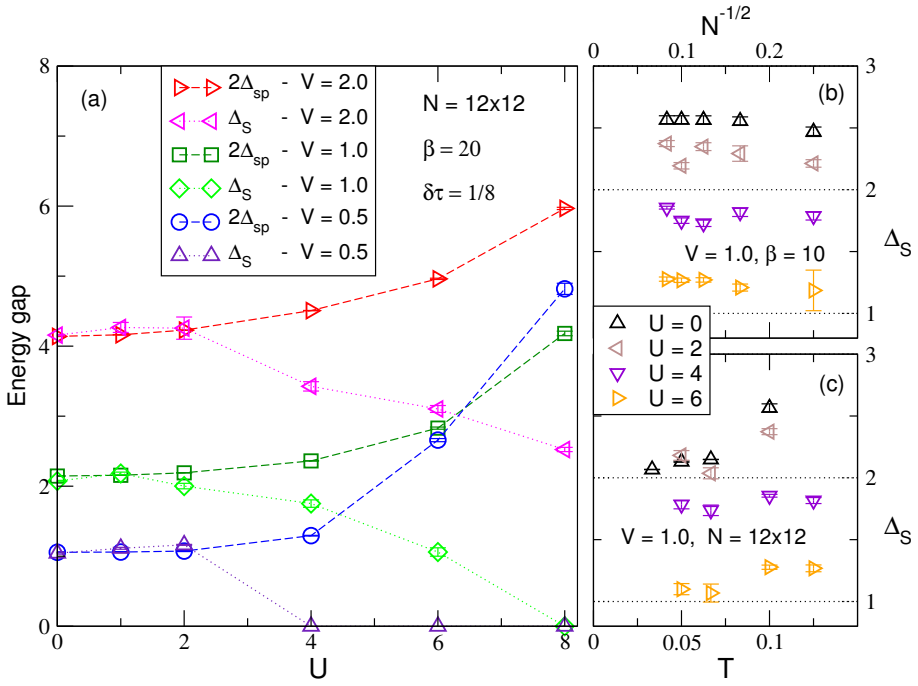

Figure 2.11: Main panel: Gaps in the single particle spectral function and the spin-spin correlation function are shown as functions of interaction U for several values of interlayer hopping V. At weak U, the spin gap Δ_S is precisely twice the single particle gap $\Delta_{\rm sp}$, as expected in a Fermi liquid phase. The smaller panels at right show the finite size (top) and finite temperature (bottom) effects for the spin gap.

simulations. The gap was estimated to vanish when the data allowed no exponential fitting and the correlation appeared to decrease as a power law, hinting at low-energy excitations.

In striking contrast with DMFT, which finds that the single-particle gap, $\Delta_{\rm sp}$, shrinks in the band insulating phase upon increasing the interaction, we find this gap to increase monotonically from its non-interacting value $\Delta^0_{\rm sp} = V$. More precisely, the gap remains roughly constant at low interaction $U \leq 2$ where the system is still clearly in the band insulating regime, before it steadily increases toward the Heisenberg limit $2\Delta_{\rm sp} = U$. The evolution of the spin excitation gap $\Delta_{\rm S}$ is opposite, the interaction suppressing the gap continuously from the non-interacting value Δ_0. While small Coulomb repulsion, $U \leq 2$, does not affect significantly its value, a further increase of the interaction monotonically suppresses the gap which finally closes at a critical interaction corresponding to the onset of magnetic order where spin density waves are expected. At $V = 2.0$, dimers across the interface prevent the transition to an

ordered phase so the spin gap should not vanish even in the infinite-U limit.

The upper right panel (Fig. 2.11b) demonstrates that finite size effects are small when estimating the spin gap Δ_S. However, to get a more precise value for the gap would require a huge computational effort. The lower right panel shows the dependence of the spin gap on decreasing temperature. In spite of the difficulty of getting very precise values, the global behaviour gives confidence that the values we obtained at $\beta = 20$ are reliable to show that the suppression of the gap is a feature of our model.

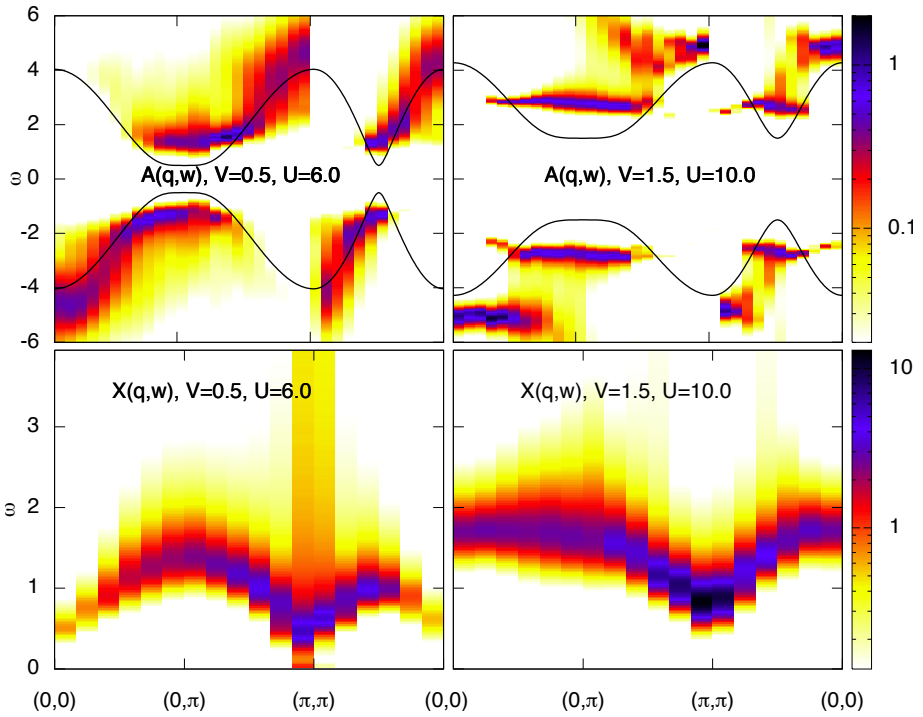

Figure 2.12: Top row: single particle spectral function in the presence (left) and absence (right) of AFM order. Bottom row: same as top row but for the spin spectral function. Results are computed on a $N = 2 \times 12 \times 12$ cluster at $\beta = 20$. Lines in the top panels are the corresponding energy bands when $U = 0$.

A deeper insight into the underlying low-energy physics in the Mott insulating phase can be gained by looking at the spectral functions resolved in momentum space. We show such functions in Fig. 2.12, where the color scale represents the spectral weight, the vertical axis is the energy, while the horizontal axis follows high symmetry lines of the first Brillouin zone.

Let us first focus on the case $\{V = 0.5, U = 6.0\}$ shown in the left panels. The upper left panel Fig. 2.12a shows the single-particle spectrum at small V,

at an interaction that ensures the Mott phase is fully attained. The black line represents the non-interacting exact result, in which we recognize the minimum gap $\Delta_0 = 2V$ at the points belonging to the Fermi surface $k_y = \pm\pi(1 - |k_x|)$. In spite of being of the order of magnitude of the bandwidth, the interaction mainly shifts the spectral functions as the gap becomes larger, so that no significant transfer of spectral weight is noticed between the two insulating phases. The lower left panel shows the spin wave dispersion at the same point of the phase diagram. The standard dispersion expected for an antiferromagnet is retrieved, with the gap closing at the instability point (π, π).

A sharp contrast to this first example is offered by looking at another point of the Mott phase, but this time in the region were no magnetic order is possible and at larger interaction $\{V = 1.5, U = 10.0\}$. The single-particle spectrum shown in the upper right panel displays –in addition to the already stated broadening of the gap with respect to the non-interacting value– a strong important flattening of the bands. This tendency can be accounted for by the fact that the local interaction attenuates the peculiarity of the non-interacting dispersion due to the hopping pattern. The spin wave dispersion (lower right panel) also differs from the magnetic phase of the Mott insulator in that no closing of the spin gap is anymore in the disordered region.

2.7 Conclusions

The results we presented above can be summarized in the phase diagram shown in Fig.2.13. Finite-size extrapolation of the magnetic structure factor allowed us to determine the boundary where antiferromagnetic long-range order sets in. Although we were not able to establish this phase boundary above $V = 1.0$ because of the large critical interaction involved, the asymptotic behavior can be deduced from the infinite-U case where no long-range order can be achieved beyond $V_c \approx 1.59$. The evolution of local moments upon increasing the interaction was shown to display an inflexion point we attributed to the Mott transition. While at moderate V the inflexion point coincides with the magnetic transition, these two markers decouple from $V = 1.0$, thus leading to an intermediate paramagnetic Mott insulator. Even though a further characterization of this intermediate phase was beyond the possibilities of this study, the strong local antiferromagnetic coupling between the bands in that region of the phase diagram hints at a Kondo insulating state. The single-particle gap evolution unequivocally eliminated the possibility of an intermediate metallic phase between the band insulating and the Mott insulating phases, underlining the importance of spatial correlations in the dynamics of this model.

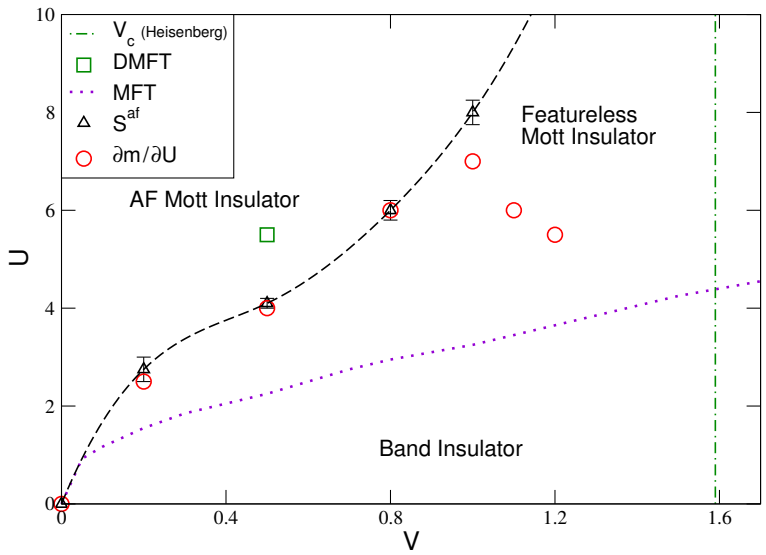

Figure 2.13: Phase diagram we obtained for the correlated band insulator, including results found with other methods. The transition line computed with DQMC (dashed) and MFT (dotted). The vertical line corresponds to the critical V, predicted by studies on the Heisenberg model, above which no magnetic long order is possible. Circles correspond to maxima in dm/dU as a function of U at constant V (see Fig. 2.8).

Chapter 3

Finite bandwidth in a heavy-fermion model

3.1 Introduction

The work presented in this chapter is related to the field of heavy-fermion materials which represents an important part of condensed matter physics. Although we are going to introduce some basic concepts that are essential for the comprehension of the results we present, an extensive review of this complex field falls clearly beyond the scope of this work. We therefore refer the reader to more comprehensive works, like the early article by Fisk *et al.* [54], the book by Hewson [55] on the Kondo problem, the review of results in the limit of infinite dimensions by Georges *et al.* [20], and the other references given throughout the chapter.

3.1.1 Resistivity minimum

In most materials the electrical resistivity can be accounted for by the scattering of the conduction electrons by phonons, the vibrations of the underlying ionic lattice. Because the phonon modes associated with these vibrations become more accessible when thermal fluctuations are important, this scattering process leads usually to a resistivity that decreases monotonically upon lowering the temperature. However, in the early thirties, materials were discovered displaying a resistivity minimum at finite temperature [56, 57], associated with the presence of magnetic impurities. The increase of resistivity at very low temperature was not understood, hence calling for further development of the theory.

The theoretical breakthrough came in 1964 from the work of Jun Kondo [58], who by taking into account spin flip scattering and computing higher order corrections unveiled a logarithmic contribution to the resistivity. This calculation led to an impressive agreement with experimental data, as illustrated in Fig. 3.1. The basic concept behind this phenomenon is the coupling of magnetic *local moments* to the conduction electrons through quantum tunneling, resulting in singlet bound states and therefore an increase of the resistivity.

Figure 3.1: In dilute AuFe alloys the resistivity increases at low temperature. The comparison of experimental data and the theoretical expression derived by Kondo leads to excellent agreement. From [58].

The energy scale below which the "free" magnetic moments will be screened by the conduction electron is known as the Kondo temperature

$$T_K \sim W e^{-\frac{1}{2\rho J}}, \tag{3.1}$$

where W is the bandwidth of the conduction sea, ρ is the density of states at the Fermi level and J the coupling between the impurities and the conduction electrons.

3.1.2 Heavy-fermions

The coupling of local moments to conduction electrons attracted attention a decade later following the discovery of Cerium based compounds (for instance $CeAl_3$) with unexpected lack of magnetic order, and displaying huge effective masses at low temperature that are typically of the order of 100 times the free electron mass [59]. Other intriguing properties are observed in these materials, such as magnetism and unconventional superconductivity [54]. Theoretical

insight into this problem was gained by studying models in which each unit cell is coupled to a magnetic moment localized in the vicinity of the nuclei, forming a dense array of Kondo-like impurities known as the Kondo lattice [60]. The possibility for localized electrons to tunnel into the conducting band creates a resonance in their density of states that leads to the rich physics observed in these rare-earth or actinide materials.

As in the single impurity problem, the temperature plays an important role in the phenomenology of heavy-fermion compounds. When the temperature is larger than the Coulomb repulsion $T > U$, the thermal fluctuations dominate the overall behaviour. As the temperature is decreased, the interaction will prevent charge fluctuations and thus lead to the formation of well localized moments, and, under certain conditions, to magnetic long-range order. Upon cooling the system further below the Kondo temperature, the spin will tunnel to the conduction sea and generate an entangled state that screens the local moments. This strong temperature dependence will be illustrated in a following section by studying the *periodic Anderson model* (PAM).

An important framework for the understanding of heavy-fermion phenomenology is the Kondo lattice model (KLM) [60], which describes a periodic array of spins that interact with a conduction band through a Heisenberg interaction J:

$$\hat{\mathcal{H}}_K = \sum_{\mathbf{k}\sigma} \varepsilon_{\mathbf{k}} c^\dagger_{\mathbf{k}\sigma} c_{\mathbf{k}\sigma} + J \sum_i \mathbf{S}_i \cdot \mathbf{s}_i, \tag{3.2}$$

where $\varepsilon_{\mathbf{k}}$ is the dispersion relation of the conduction band. This model can be derived in the strong coupling limit from the PAM by mean of a Schrieffer-Wolff transformation [61]. Quantum Monte Carlo studies of the KLM have been performed in the last decade both in the absence [62] or presence [63] of an external magnetic field. As was found by Doniach [60], a weak antiferromagnetic interaction between the spins is mediated by the conduction band. In the case of the square lattice, the nesting of the Fermi surface makes the system unstable to antiferromagnetic excitations and long-range order is therefore induced by this interaction. This indirect interaction is named after Ruderman-Kittel-Kasuya-Yosida (RKKY), and was first discussed in the context of nuclear physics.

The model we will consider throughout this chapter is the following two-

band fermionic Hubbard Hamiltonian:

$$\begin{aligned}\hat{\mathcal{H}} = & - \sum_{\langle \mathbf{j},\mathbf{k}\rangle l\sigma} t_l \, (c^{\dagger}_{\mathbf{j}\, l\, \sigma} c_{\mathbf{k}\, l\, \sigma} + \text{h.c.}) \\ & - V \sum_{\mathbf{j},\sigma} (c^{\dagger}_{\mathbf{j}\, f\, \sigma} c_{\mathbf{j}\, d\, \sigma} + \text{h.c.}) \\ & + \sum_{\mathbf{j}\, l} U_l (n_{\mathbf{j}\, l\uparrow} - \frac{1}{2})(n_{\mathbf{j}l\downarrow} - \frac{1}{2}) - \mu \sum_{\mathbf{j}\, l\, \sigma} n_{\mathbf{j}\, l\, \sigma}.\end{aligned} \tag{3.3}$$

Equation (3.4) describes a two-dimensional square lattice with electronic bands $l = d$ and $l = f$. The coordinates $(\mathbf{j}, l)$ label the spatial site and the band, respectively; $\sigma \in \{\uparrow, \downarrow\}$ denotes the spin of the electron. The first two terms are respectively the intra-band and inter-band kinetic energies. The nearest-neighbor hopping matrix element in the d-band will be chosen to be the unit of energy in the remainder of this work, $t_d = 1$, while its f-band counterpart, t_f, will be allowed to vary. The inter-band hybridization, V, controls the singlet formation and will be another tunable parameter. The on-site repulsion U_l is chosen to be constant within a band: the f-band will include a moderate repulsive interaction, $U_f > 0$, while the d-band will be non-interacting, $U_d = 0$. The chemical potential μ is set to zero, the system being then at commensurate filling for both bands d and f. This latter choice emphasizes Mott and antiferromagnetic physics, and also avoids any sign problem in our DQMC simulations.

3.2 The Periodic Anderson Model

When the nearest-neighbor hopping in the f-band is chosen to be zero, $t_f = 0$, the hamiltonian in Eq. (3.4) describes the periodic Anderson model (PAM). Even though the properties of this model are well known (see for instance [64]), we will briefly present, for pedagogical purpose, a few results we obtained at a moderate interaction $U = 4$ for a small lattice $N = 8 \times 8$, in a broad range of temperatures.

At $V = 0$, the d-orbital is a metal while the f-orbital is made of independent electrons, insulating and not ordered. As we already observed in the bilayer model studied in Chapter 2, the hybridization V between the orbitals favors the formation of two-site singlets that are characterized by an antiferromagnetic coupling. This tendency is observable in Fig. 3.2, in which the inter-band spin correlation, $c_{\perp} = \langle \sigma^x_{i,f} \sigma^x_{i,d} \rangle$ [1], is represented as a function of V for several inverse

[1] The spin operator σ^x was defined in Eq.1.42.

temperatures β. While at high temperature singlet formation is impaired by thermal fluctuations, the low temperature limit shows a rapid appearance of an AF correlation that saturates at large V.

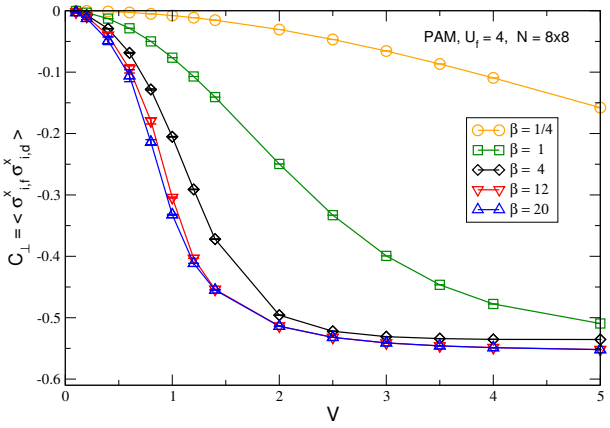

Figure 3.2: The inter-band hopping V drives a phase transition in the PAM from an antiferromagnetic ordered state to a singlet phase.

The magnetic properties of the PAM can be quantified by looking at the antiferromagnetic structure factor $S^{\rm af}$ that we defined in Eq.(1.43). Although we will not perform an extrapolation to the thermodynamic limit, the consideration of that small cluster is sufficient to capture the general tendencies of the model. As we previously mentioned, the RKKY interaction is a weak coupling between the magnetic moments mediated by the conduction electrons, and favors AF order. Two phenomena will tend to destroy this tendency toward magnetic order, namely thermal fluctuations and singlet formation. Consequently, while the zero-temperature phase diagram predicts the magnetic phase to exist in the whole $V = [0, V_c]$ region prior to the appearance of singlets, the AF structure factor vanishes also in the small V limit where the RKKY coupling $J_{RKKY} \sim V^4/U_f^2 W$ is small (here W is the bandwidth). As a result, the AF structure factor at finite temperature is characterized by a peak below V_c, that broadens toward small V as the temperature is decreased.

The role of temperature is made clearer by investigating the spectral functions[2] corresponding to single-particle excitations in the f-band, $A_f(\omega)$. At first, as the temperature is decreased, the Hubbard gap separating the bands and corresponding to the cost of double occupancy appears. From $\beta = 4$, a peak at the Fermi energy signals the Kondo resonance due to the coupling of moments to the conduction band. Finally, as the temperature is further lowered below the RKKY temperature, the Kondo peak gets split by a small

[2]Please refer to Eq.(1.54) for the definition of $A(\omega)$.

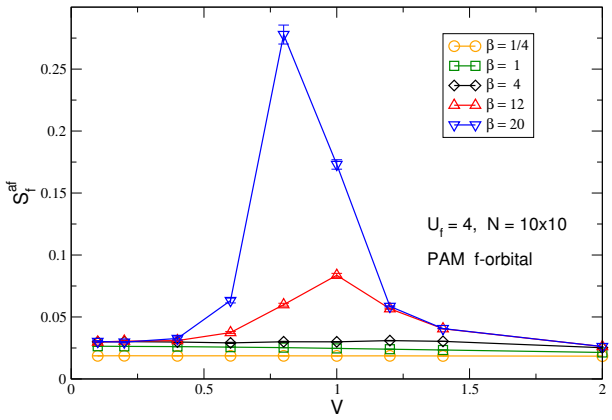

Figure 3.3: At small V, thermal effects destroy the magnetic order favored by the indirect RKKY coupling. At large V, it is the singlet formation that prevents magnetic order.

gap due to antiferromagnetic order. The temperature at which this gap forms is concomitant with the magnetic ordering that we previously deduced from the peak in the AF structure factor.

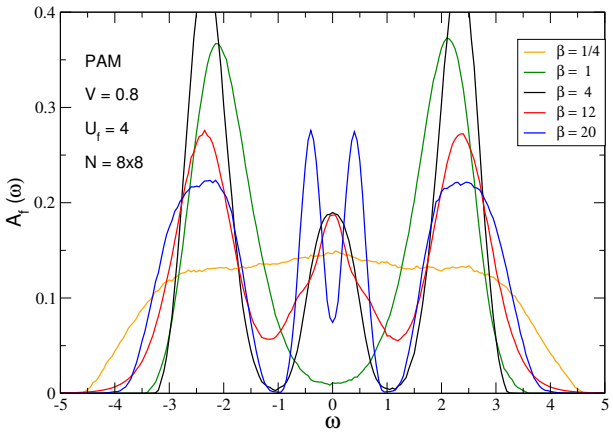

Figure 3.4: Density of states $A_f(\omega)$ of interacting band in the PAM. As the temperature is decreased, fine structure becomes apparent: the initial gap in between the broad Hubbard bands is followed by the onset of a Kondo resonance at the Fermi level, which is eventually split as magnetic order emerges. Parameters are $V = 0.8$, $U = 4$, and the lattice size is $N = 10 \times 10$.

3.3 Finite f-orbital bandwidth

The PAM is *a priori* a richer model than its infinite-U_f limit, the Kondo lattice model, allowing, in particular, charge fluctuations in the correlated band. However, the choice $t_f = 0$ leads to a flat band, a peculiar case that is not necessarily seen in real compounds. An important point to be considered is that a non-zero hopping t_f will allow antiferromagnetism to appear through *direct exchange*. It is then natural to address the question of how this alternate magnetic coupling will affect the tendency to order, which is already favored in the PAM by the indirect RKKY coupling.

The hamiltonian we will consider further is the one given in Eq.(3.4). For convenience, we introduce the ratio between the bandwidths $\alpha = t_f/t_d$. Several numerical studies have been performed on this model with $t_f \neq 0$ (sometimes called "actinide hamiltonian"). To our knowledge, the first paper on it was by Continentino *et al.* who computed the thermodynamic properties beyond the mean-field level [67], but without discussing the specific role played by the f-orbital bandwidth.

It was subsequently studied, within the single-site DMFT and the numerical renormalization group (NRG) methods, by Shimizu *et al.* [68] who considered the cases of both positive and negative α. As we shall discuss in the next section, these choices lead to very distinct non-interacting limits: when $\alpha > 0$ there is a metal-insulator transition at finite hybridization V, while $\alpha < 0$ has a band gap at any V. At half-filling, they found that these features of the density of states are not modified in the interacting case, the widths of the gaps being merely renormalized. As our results will show, this is not always true when one accounts for the spatial correlations (or equivalently the momentum dependence of the self-energy, in the DMFT language). In another single-site DMFT study [69], de' Medici *et al.* found that, whenever the interband hybridization is nonzero, $V > 0$, there is no longer a Mott transition in the f-band at $T = 0$. At finite-T, the first-order transition is still present. Some important discrepancies with our framework should be noted, making cumbersome a direct comparison with our results. First, the model used in this paper has a nonzero critical interaction $U_f^c > 0$; second, single-site DMFT forbids any magnetism to be accounted for.

A few works have compared results from this model to experimental values. For example, Sakai *et al.* included the effect of the crystal field and the spin-orbit coupling, and were able to retrieve the Kondo temperature of Cerium-based compounds [70]. The relative importance of the inter-band hybridization V and the f-band hopping t_f was also evaluated [71], estimating that $V > t_f$ in several elements of the actinide series. Finally, interband interaction was

recently shown to engender a charge density wave (CDW) phase analogous to the one find in several compounds [72].

3.3.1 Non-interacting Limit

In the non-interacting limit, $U_f = 0$, the regions with positive and negative t_f/t_d have quite distinct behavior. The former is a metal with two overlapping bands, up to a critical inter-orbital hybridization above which it crosses into a band insulator, while the latter is always a band insulator. Such behavior is easily understood in terms of the dispersion and ensuing crossing of the independent f and d bands.

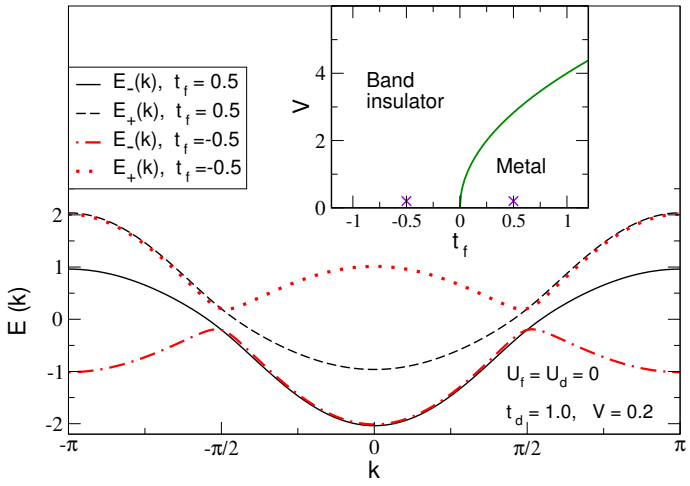

Figure 3.5: Non-interacting band structure of the Hamiltonian given in Eq. (3.4), in the 1D case. It illustrates the distinct behavior of the two cases when t_d and t_f have same or opposite signs. In the former situation (black curves), there are two overlapping bands as long as the interband hopping V is not too large, and the half-filled system is a metal up to a critical V_c. In the latter case (red curves), a gap opens between the bands and the system is an insulator at half-filling for all V.

For simplicity, we define $x(k) = \cos k_x + \cos k_y$. The two bands are then given by

$$E_{\pm}(k) = -(t_f + t_d)x \pm \sqrt{(t_d - t_f)^2 x^2 + V^2} \tag{3.4}$$

As in our previous models, a particle-hole symmetry enforces half-filling at $\mu = 0$, and the system is metallic only if the equation $E_{\pm}(k) = 0$ is satisfied for some value of k. For this to happen, this equation must possess a real

solution $x(k)$ such that $x^2 < 4$, that is

$$\begin{cases} t_f/t_d > 0 \\ 2|V| < \sqrt{W_1 W_2} \end{cases} \tag{3.5}$$

where W_1 and W_2 are the bandwidths of the two distinct layers. For the two dimensional case, Eq. (3.4) implies that the metal-insulator transition happens when $|V_c| = 4\sqrt{t_f}$. The Fermi surface is given by the equation

$$\pm 2\sqrt{t_f t_d}(\cos k_x + \cos k_y) = |V| \tag{3.6}$$

There is a (π, π) nesting between the two branches of the Fermi surface. Consequently, the metal is expected to be highly susceptible to the formation of long-range magnetic order at $T = 0$ and for arbitrarily weak repulsion, as was previously discussed for the 2D Hubbard model.

The non-interacting phase diagram is illustrated in the inset of Fig. 3.5, while the main panel shows the dispersion relation, for one dimensional geometry, at two particular points. At $\{t_f = 0.5, V = 0.2\}$, the hybridization is below the transition V_c and the two bands overlap, leading to metallic properties. At $\{t_f = -0.5, V = 0.2\}$, the two intra-orbital hopping terms have opposite signs, and consequently the bands are separated by a gap for an arbitrarily small hybridization.

3.3.2 Mean field theory

The finite-temperature statistical properties of this system will be computed with two methodologies. The first is the QMC method we already presented in Chapter 1, the second is mean field theory (MFT) that we shall briefly describe now.

The method consists of decoupling the on-site interaction

$$U n^{\uparrow} n^{\downarrow} \to U(\, n^{\uparrow}\langle n^{\downarrow}\rangle + \langle n^{\uparrow}\rangle n^{\downarrow} - \langle n^{\uparrow}\rangle\langle n^{\downarrow}\rangle), \tag{3.7}$$

with mean-field ansatz

$$\begin{cases} \langle n^{\uparrow}_{i\alpha} n^{\downarrow}_{i\alpha}\rangle & = 0 \\ \langle n^{\uparrow}_{i\alpha}\rangle + \langle n^{\downarrow}_{i\alpha}\rangle & = 1 \\ \langle n^{\uparrow}_{i\alpha}\rangle - \langle n^{\downarrow}_{i\alpha}\rangle & = 2m_{\alpha}. \end{cases} \tag{3.8}$$

By introducing the mean-field eigenvalues of a single layer

$$E_{k\pm} = \pm\sqrt{\varepsilon_k^2 + (Um)^2}, \tag{3.9}$$

we can conveniently express those of the bilayer as

$$\lambda = \pm\frac{1}{2}\left[E_{k,d}^2 + E_{k,f}^2 + 2V^2 \pm \sqrt{(E_{k,d}^2 - E_{k,f}^2)^2 + 4V^2\mathcal{E}^2}\right]^{1/2} \tag{3.10}$$

where we omitted the $\pm$ subscript (since $E_{k\pm}$ always enter as squares) and we defined

$$\mathcal{E}^2 = \left(\sum_\alpha \varepsilon_{k,\alpha}\right)^2 + \left(\sum_\alpha m_\alpha U_\alpha\right)^2 . \tag{3.11}$$

It is easy to verify that when $m_f m_d < 0$ (antiferromagnetic order) the equation $\lambda = 0$ does not admit any real solution regardless of the value of k. This implies that the Fermi surface is fully gapped and suggests that such an antiferromagnetic solution is the correct mean field solution at moderate U values.

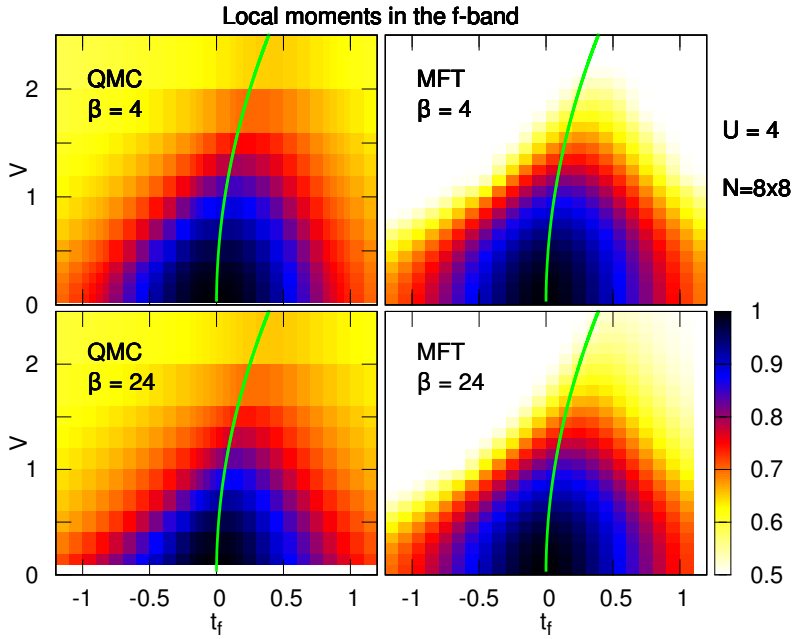

Figure 3.6: Evolution of the local f moment, m_f, with t_f and V. Results are at $U_f = 4t$, and were obtained by QMC (left panels) and MFT (right panels). At $\beta t = 4$ (top panels), the moments are mostly formed and decreasing the temperature to $\beta = 24$ has no significant effect. m_f is largest for small values of these two kinetic terms, since this minimizes the quantum fluctuations. The asymmetry with respect to the PAM limit, $t_f = 0$, reflects the non-interacting metal-insulator boundary (green line).

3.4 Magnetic properties

The key ingredient for magnetism is the formation of magnetic moments. We recall that the local moment on the f-band, m_f, is related to the double occupancy D by:

$$m = \frac{1}{N}\sum_{\mathbf{j}}\langle(\sigma^z_{\mathbf{j}f})^2\rangle = 1 - \frac{2}{N}\sum_{\mathbf{j}}\langle n^{\uparrow}_{\mathbf{j}f} n^{\downarrow}_{\mathbf{j}f}\rangle = 1 - 2D. \tag{3.12}$$

The evolution of m_f as a function of the nearest-neighbor hopping t_f and of the hybridization V is presented in Fig. 3.6. The results obtained by both MFT and QMC are shown for two temperatures, $\beta = 4$ and $\beta = 24$. A first observation is that there is almost no difference when the temperature is decreased, showing that at $\beta = 4$ the moments have already converged to their ground-state value. A second striking feature is that MFT captures the general behavior of moments, and little difference is seen with respect to the QMC data. However, the transition is made artificially abrupt by the mean field treatment, which also leads to the uncorrelated value $m_f = 1/2$ at large $\{t_f, V\}$ while the effect of correlation is still visible in the QMC results.

Local moments in the f-band are found to be fully formed when both t_f and V are small. Indeed, when the kinetic terms are much smaller than the interaction, the f-orbital is almost a two-dimensional Heisenberg model with localized spins. At fixed t_f, moments are monotonically suppressed upon increasing the hybridization that tends to create entangled singlet pairs. At constant hybridization V, increasing $|t_f|$ amounts to diminish the effective repulsion since the bandwidth is made larger, which consequently delocalizes the electrons. This evolution of the moments reaches a maximum at small positive t_f, and these maxima roughly follow the non-interacting metal-insulator boundary. We shall see this asymmetry is also present in long-range magnetic correlations.

We now move to the nearest-neighbor spin correlation in the f-band, $\langle\vec{\sigma}_{\mathbf{j}f}\cdot\vec{\sigma}_{\mathbf{j}+1,f}\rangle$ [3]. The QMC results for these short-range correlations are plotted in Fig. 3.7, showing three temperatures $\beta = \{4, 12, 36\}$. We first underline the fact that at large t_f and V, the absence of localized moments prevents any spin correlation. Beyond this observation, the behavior of this correlation differs in several ways from the evolution of the moments.

In the limit $V = t_f = 0$, the localized spins are completely decoupled and there is consequently no correlation between neighbors. On the constant $V = 0$ line, increasing the bandwidth allows the spin to couple through a direct exchange $J \sim t_f^2/U_f$ that favors antiferromagnetism, independently from

[3] The spin components were defined in Eq. (1.42).

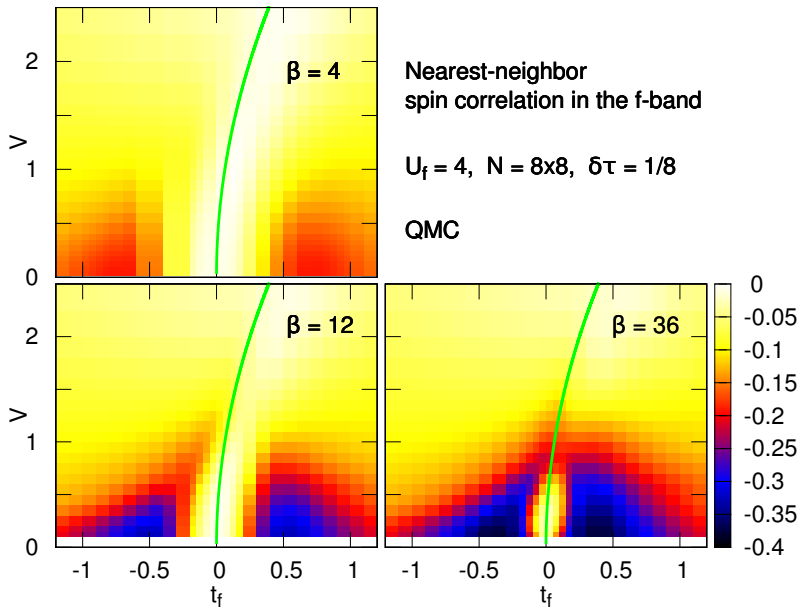

Figure 3.7: Near neighbor spin correlations in the f-band. The hopping term t_f provides an exchange interaction in the f-band, which leads to antiferromagnetic correlations. V also causes antiferromagnetic interactions, but by a weaker RKKY coupling. There is significant growth in the spin correlations as β increases, even well after the local moments have saturated (Fig. 3.6).

the sign of t_f. At large $|t_f|$, the interaction becomes weak with respect to the kinetic energy and the correlation is thus suppressed. At $t_f = 0$, no direct exchange is possible between the moments, and the antiferromagnetic correlation if mediated by the conduction electrons. At low temperature, this indirect RKKY exchange is at first enhanced by increasing the hybridization between orbitals, but is eventually stopped when singlets form. The temperature dependence is much larger than for moments, because the energy scales of the exchange interactions are both smaller than the interaction U_f that prevents double occupancy.

Beyond these nearest-neighbor correlations, it is interesting to track the magnetic long-range correlations in the f-band. We define

$$S_f \;=\; \frac{1}{3N'}\sum_{\mathbf{j},\mathbf{k}}{}' \langle\, \sigma^z_{\mathbf{k}\,f}\sigma^z_{\mathbf{j}\,f} + 2\,\sigma^-_{\mathbf{k}\,f}\sigma^+_{\mathbf{j}\,f}\,\rangle\,(-1)^{|\mathbf{k}-\mathbf{j}|}. \tag{3.13}$$

This quantity is related to the antiferromagnetic structure factor, which was defined in Eq. (1.43). However the prime symbols in the sum and in the number of sites N' indicate that we omitted contributions from local and nearest

neighbor correlations in order to better single out the long range behaviour.

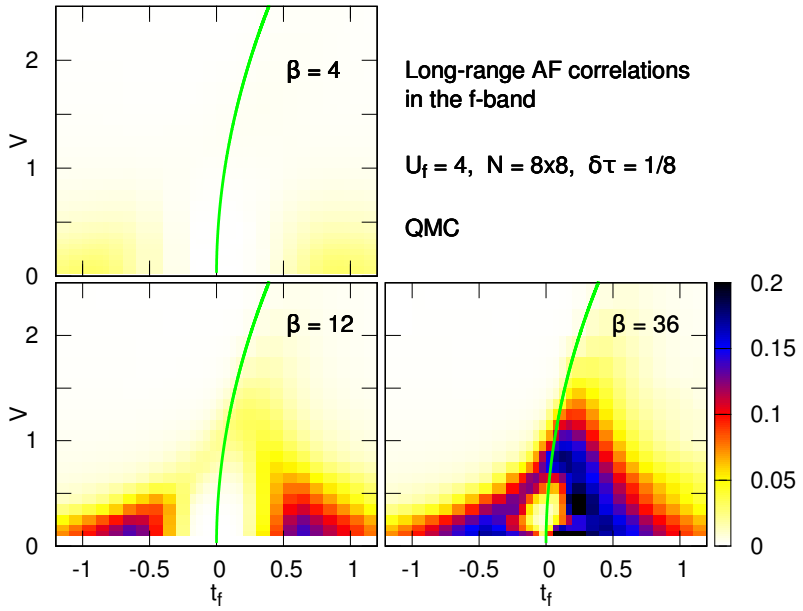

Figure 3.8: The f-band long-range antiferromagnetic correlations shown in the t_f-V plane for different inverse temperatures β. Because S_f probes spin ordering at large distance, the convergence with increasing β is more gradual than for the near-neighbor spin correlations. As β increases, the paramagnetic region where V and t_f are both small, and hence so too are the AF energy scales, shrinks. As with the local moment S_f is peaked at small, positive t_f.

The temperature dependence of the long-range magnetic correlations is stronger than in the nearest-neighbor case. At $\beta = 4$, S_f is essentially zero in the whole $t_f - V$ plane, and magnetic order is still not completely settled at $\beta = 24$. Even though we did not finely determined the magnetic boundary by performing an extrapolation to the thermodynamic limit, the behavior of the truncated structure factor on this small $N = 8 \times 8$ cluster is sufficient to capture its dominant features.

As for nearest-neighbor correlations, we can relate the vanishing of magnetism when t_f or V are large to the suppression of local moments. The hybridization V destroys AF order by forming singlets, while large $|t_f|$ delocalizes the electrons and consequently also defeats magnetic order. The asymmetry relative to $t_f = 0$ is also noticeable here, leading to a stronger magnetic order around $t_f = 0.2$. The "hole" when t_f and V are both small can be understood from a strong coupling perspective. Decreasing the bandwidth weakens the direct exchange between moments, while decreasing the hybridization suppresses

the indirect exchange mediated by the d-band. Consequently, magnetic order should be found for arbitrary small kinetic energies in the $T = 0$ limit only.

3.5 Spectral functions

As we have discussed in the beginning of this chapter, the spectrum of excitations of the PAM at half-filling displays complex features that reflect the interplay of antiferromagnetic order, the formation of a Mott insulator, and the emergence of Kondo singlets. The former two effects suppress the density of states at the Fermi level, giving rise to a gap. In the latter phenomenon, the screening of local moments in the f-band is associated with a Kondo resonance (peak) at the Fermi level. The temperature affects these competing possibilities. For example, a Kondo resonance might first form as T is lowered, followed by a splitting of that resonance as AF order becomes established. In addition to such correlation effects, the spectral function of our Hamiltonian also exhibits the influence of the non-interacting band structure which can be either gapped or metallic. In order to understand how the energy spectrum of the PAM is modified by a finite bandwidth, we will present in what follows results for the single-particle spectral function in the f-band, $A_f(\omega)$[4].

In Fig. 3.9 is presented $A_f(\omega)$ at a "high" temperature, $\beta = 2$, for which we proved there is no magnetic order. Four values of the hopping t_f are shown, $\{-0.9, -0.2, +0.2, +0.9\}$, for each one of which the results are compared for two values of the interaction $U_f = \{4.0, 8.0\}$. In green we plot the edges of the non-interacting bands, defined by $\mathrm{Max}\,[E_-(\mathbf{k})]$ and $\mathrm{Min}\,[E_+(\mathbf{k})]$, which delimit the band gap at $U = 0$. At large V, for both $U_f = 4$ and $U_f = 8$, this non-interacting gap is not significantly altered by the interaction. In the $V = 0$ limit, the f-band is a simple 2D Hubbard model and a Mott gap is expected at any non-zero repulsion because of the nesting of the Fermi surface and the divergence of the non-interacting density of states (DOS). This Mott gap is clearly visible in the $|t_f| = 0.2$ panels, separating by the energetic cost of double occupancy the two bands centered at $-U_f/2$ and $+U_f/2$. At finite V, a Kondo peak appears around $\omega = 0$. This resonance is eventually destroyed at larger V, when the systems goes to the paramagnetic singlet phase. Strikingly, little difference is observed at small V between the $t_f \pm 0.2$ cases, in spite of their difference in the non-interacting limit where one is metallic and the other insulating. Since the interaction localizes the electrons in f-band, the screening by the d-band is largely independent of the sign of the hopping t_f.

The situation is clearly different at $t_f \pm 0.9$. At $U_f = 4$, a peak at the

[4] $A_f(\omega)$ was defined in Eq. (1.54).

Fermi energy is visible all the way down to the decoupled limit $V = 0$, and the lobes at $-U_f/2$ and $+U_f/2$ are barely distinguishable. This indicates that, at $U_f = 4$, the temperature $\beta = 2$ is too high for the local moments to form and the Mott gap to appear. This interpretation is supported by the fact that, upon increasing the interaction up to $U_f = 8$, the Mott gap becomes visible. The differences in the non-interacting limit between positive and negative t_f persist when the interaction is plugged in. At $t_f \pm 0.9$, a negative t_f leads to a band gap at any V, while a positive value keeps system metallic up to a critical hybridization $V_c \approx 3.8$. This observation can be made clearer by looking at the low temperature spectra.

The upper panels in Fig.3.10 are the $\beta = 24$ counterpart of the previous figure, at $U_f = 4$. At $t_f = 0.2$, the Kondo resonance is now split, concomitantly with the establishment of long-range magnetic order. We already observed this phenomenon in the PAM, and a small positive hopping in the f-band leaves it qualitatively unchanged. At larger bandwith, for instance $t_f = 0.9$, there is a broader range where free electrons can screen local moments, leading to a split resonance that survives up to $V \approx 3.8$. When the hopping term is negative, the gap in the non-interacting density of states prevents the scattering of conduction electrons into f-band.

The mean field results shown in the lower panels of Fig.3.10 show an overall agreement with the QMC results. A notable difference is the gap at moderate V, which in the case of MFT is not independent of the value of V, and is larger than the gap extracted from QMC. This can be explained by the fact that MFT can not access to the Kondo screening and thus captures only an antiferromagnetic Mott insulator.

3.6 Conclusion

Starting from a standard model for heavy-fermion physics, the periodic Anderson model, this part was devoted to study how a finite bandwidth in the interacting band modifies the magnetic and spectral properties. After introducing a few basic notions of the field, we presented some results we obtained for the PAM, underlining how tuning the temperature reveals the different energy scales of the model. We then reported several studies previously done on similar hamiltonians, before discussing the results we obtained by way of Determinant QMC and mean field theory (MFT). By allowing the sign of the nearest neighbor hopping in the f-band, t_f, to have the same or opposite as the hopping in the non-interacting d-band, we started from a rich non-interacting phase diagram. In the latter, a metal-insulator transition upon increasing the

interband hybridization V exists only for positive t_f, while the negative case leads to a band gap at any V. The interacting phase diagram reflected this non-trivial starting point. In particular, it was shown that both local moments and long-range antiferromagnetic correlations are maximized at small positive t_f, in correspondance with the $U = 0$ metal-insulator transition. Finally, the single-particle spectral functions reveals several features that come on top of the non-interacting band structure. While most properties are captured by a mean field treatment, a Kondo resonance is found by DQMC at intermediate temperature for both negative and positive t_f. This resonance gets eventually split at lower T, for positive t_f only.

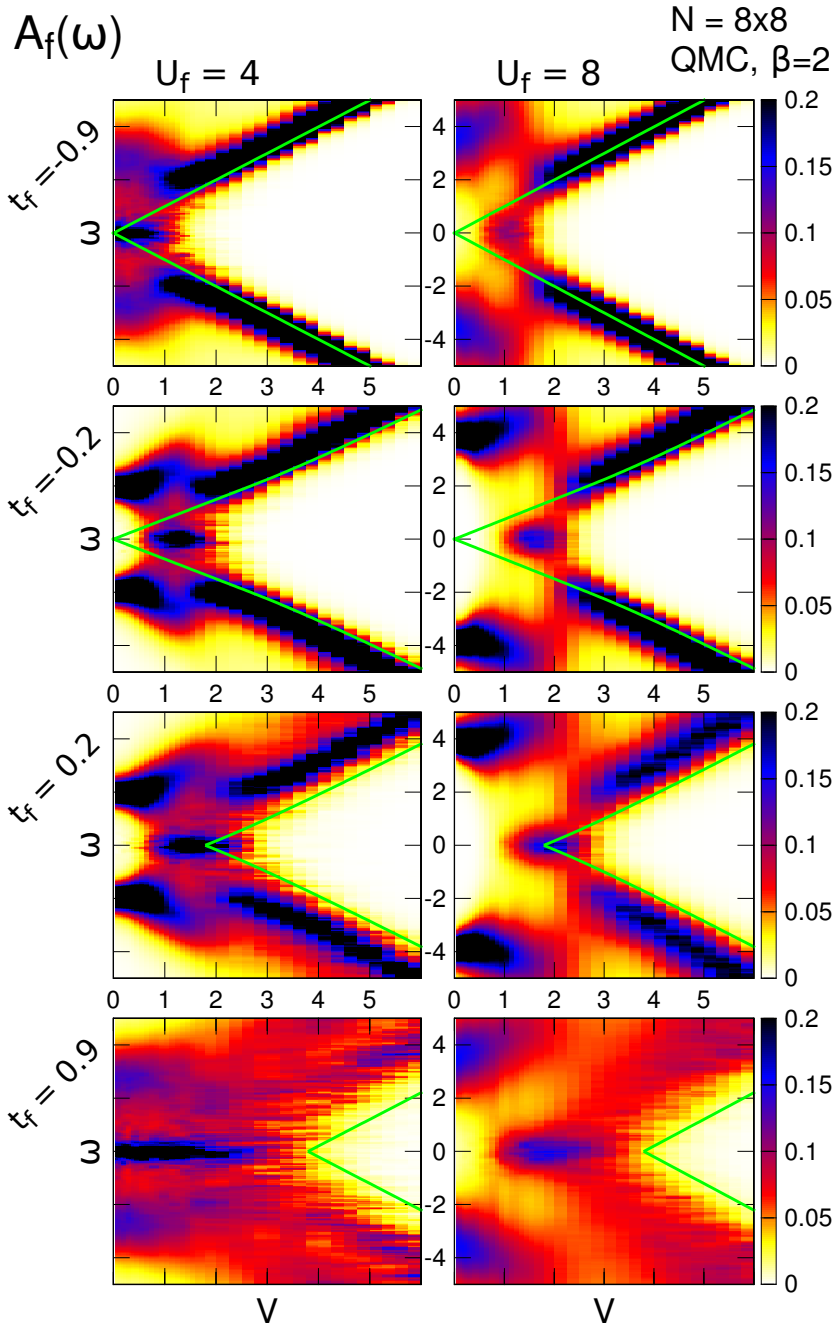

Figure 3.9: The spectrum of the f-band at $U_f = 4, 8$ (left and right panels respectively) as a function of interband hybridization V for inverse temperature $\beta = 2$. Four values of f-band hopping t_f are shown. The green lines correspond to the edge of the non-interacting density of states, which delimit the band gap. At $t_f = \pm 0.2$, two bands are separated at small V by a Slater gap of width U_f corresponding to the cost of double occupancy. At larger V, a Kondo peak is visible at $\omega = 0$ below a critical threshold V_c. The triangular shaped regions at large hybridization correspond to the singlet formation that prevents the Kondo resonance and leads to a gap that is well described by the non-interacting dispersion relation.

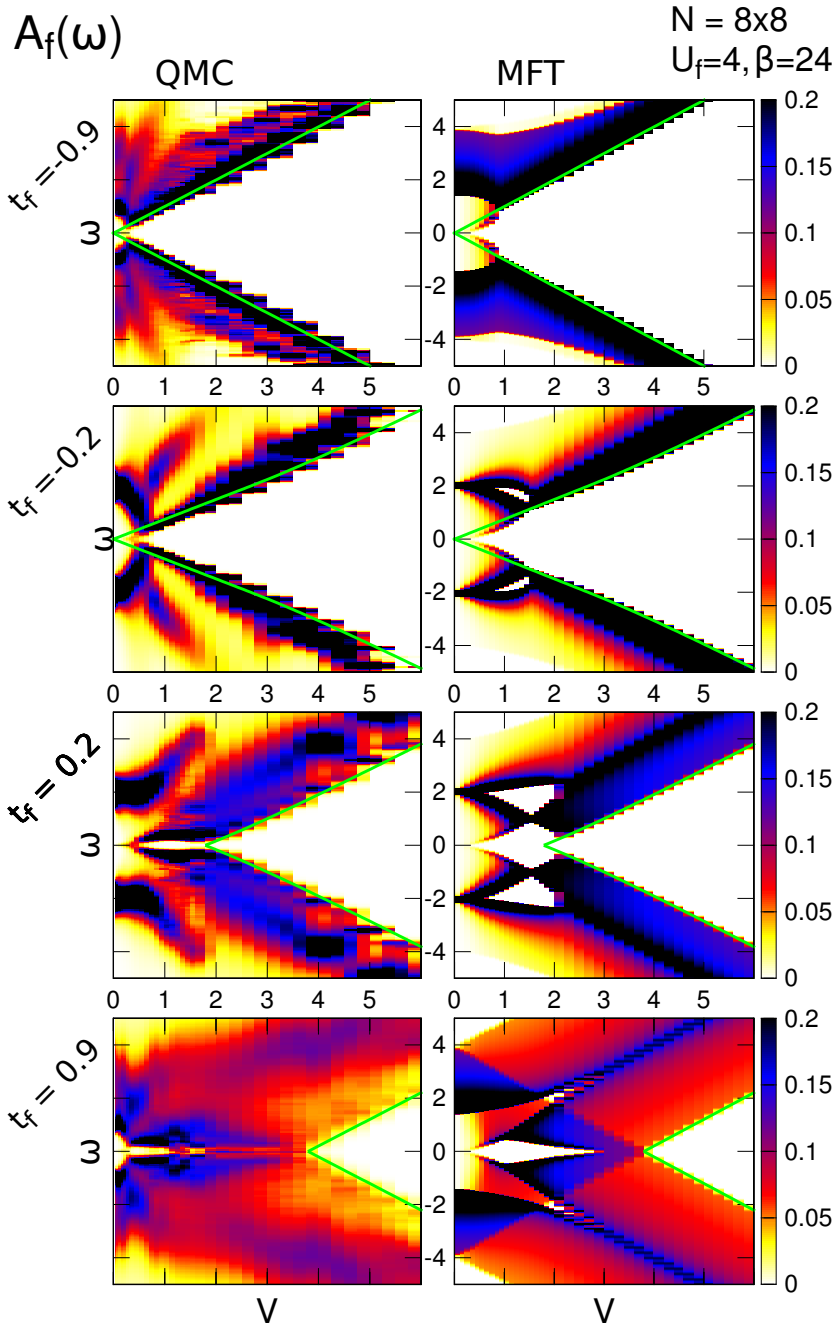

Figure 3.10: The left panels are the same as Fig. 3.9, except at much lower temperature $\beta = 24$. The smearing of the band gaps is greatly reduced. In addition, the Kondo resonance has been split by a gap associated with the formation of AF order. The insulating character of the $t_f < 0$ case for all V is more apparent at this lower temperature. The right panels show the MFT results for same parameters. These mean field results capture correctly most of the spectral properties, except the narrow constant gap at intermediate V when t_f is positive.

Chapter 4

Metal-Mott insulator Interface

4.1 Introduction

In material science, surfaces are often known to bear physical properties that differ considerably from that of the bulk because of so-called *structural reconstruction*. Since the specific arrangement of the atoms in a bulk crystal arises from the minimization of the energy due to interactions between neighboring sites, it is natural to expect this structure to change at a surface where the local environment is modified and the coordination number is reduced. Such modifications of the lattice structure can obviously alter the electronic properties of the surface, a change in the inter-atomic distances resulting, for instance, in a smaller overlap of orbitals and therefore in a different hopping matrix element. By analogy with its lattice counterpart, the term *electronic reconstruction* was coined [73, 74] to describe the modifications of electronic properties at surfaces in comparison with those of the bulk. It was for example found that in the $Ca_{1.9}Sr_{0.1}RuO_4$ compound, the Mott transition occurs at a lower temperature at the surface due to the lattice distortion at the boundary [75]. At interfaces, where materials with different intrinsic properties are in contact, the local environment is also modified at the surfaces. The problem can consequently become more complex than in the decoupled materials and the interfacial phase diagram is *a priori* non-trivial.

We shall review below some recent progress done in the field of correlated heterostructures, with particular emphasis on the metal-Mott insulator structures that resemble the one we studied numerically. For more complete surveys of the field, the reader can refer to the following works [76, 77, 78, 79], and to the additional references provided below.

Interfaces are at the core of integrated electronics, with metal oxide semiconductor field-effect transistors (MOSFETs) as main building blocks. The miniaturization of these components is currently hitting the bottleneck of quantum mechanics, in particular because of the direct tunneling of the electrons through the thin SiO_2 dielectric layers in the components. Although recent achievements in semiconductor manufacturing -for example the integration of materials displaying better dielectric properties [80]- have broadened the possibilities of "standard" microelectronics, these improvements will not allow to

bypass the intrinsic limitations of the nanometer scale. Overcoming these difficulties is a major technological challenge that requires a deeper understanding of the many-body properties of strongly correlated electronic systems as well as the improvement of the technological ability to synthesize and control them.

The field of strongly correlated electronic systems offers a huge diversity of quantum phases, whose transport and magnetic properties are expected to lead to technological application. Phase transitions offer the advantage of accessing phases with very different physical properties within the same material by tuning a simple parameter, for instance magnetic or electric fields [81], the carrier densities or hydrostatic pressure. The last decades have seen considerable advances in this field, eventually leading to mainstream applications.

The giant magnetoresistance (GMR) effect offers a striking example of how fundamental magnetic properties of materials can find application in mass-market technology. Discovered independently in 1988 by Fert [82] and Grünberg [83], the GMR takes advantage of the spin polarization shown by some ferromagnets, namely in which the two spin species display different densities of states at the Fermi level. It was shown by these early works that electrical conductivity in layered heterostructures (grown epitaxially or by simple sputtering) alternating such ferromagnets with nonmagnetic layers, shows strong magnetic-field dependence. These structures work as "spin valves" that allow to switch electric current by varying the applied magnetic field and have led in 1997 to the release by IBM of the first hard drive disk using a GMR head. More extensive reviews on "spintronics" can be found among the many works that have been published in the field lately (for instance see [80, 84, 85]).

The growth of thin films has attained high precision with deposition techniques such as pulsed laser deposition and molecular beam epitaxy (MBE). The latter consists of sublimating elements that will eventually condense on a substrate waffer. This process can be monitored through reflection high-energy electron diffraction or other techniques [86] and leads to the fabrication of heterostructures made of layers whose thickness is controlled with great precision. In addition, detailed stuctural properties such as the crystalline orientation or the epitaxial strain can be chosen during the growth [87], leading to a great number of accessible functional properties.

In order to illustrate the current possibilities of thin-film oxyde heterostructures, we shall briefly review the case of $LaTiO_3/SrTiO_3$ and related junctions, which have been under close scrutiny during the last decade. In the bulk limit, $SrTiO_3$ and $LaTiO_3$ are both insulators. While in the former insulating properties arise from the band structure and is consequently a conventional band insulator, the latter is a Mott insulator in which transport vanishes because of the strong Coulomb repulsion between electrons. Ohtomo *et al.* [88] built

heterostructures alternating thin films of these two materials by pulsed laser deposition. This technique allowed them to design superlattices in which the thickness of the films are controlled down to the unit cell scale (Fig.4.1). It was later discovered that in the similar heterostructure, $LaAlO_3/SrTiO_3$, a two-dimensional electron gas with high carrier mobility can be created by electron-doping the interface, while its hole-doped counterpart is insulating [89]. The conductivity of this 2D state can be tuned by applying a gate voltage that drives a metal-insulator transition [90], opening the door for possible applications. Superconductivity was also discovered at that interface, with an unexpected increase of the critical temperature by applying an external magnetic field [91].

Figure 4.1: Annular dark field image of an heterostructure alternating layers of $LaTiO_3$ (bright) and $SrTiO_3$. The numbers indicate the thickness of the $LaTiO_3$ layers, which is controlled down to the unit cell scale. The top panel is a zoom on a sequence of 1×5 layers. From [88].

4.1.1 Theoretical methods

On the theoretical side several methods are in principle available, but each has advantages and limitations. Among the most successful are techniques related to the density functional theory such as the local density approximation (LDA), which can make allowance for local Coulomb interaction in the so-called LDA+U method [92]. The latter has led to results showing good agreement with experiments [93]. Regarding model Hamiltonians such as the Hubbard model, dynamical mean field theory (DMFT) can be applied to interfaces or heterostructures involving a large number of atomic layers [94], while its cluster extensions allow, to a certain extent, to take into account spatial correlations.

These spatial correlations are described better by way of Quantum Monte Carlo techniques, but a major obstacle is the number of sites available to simulations. While the single band Hubbard model in two-dimensions has been extensively studied by means of QMC methods, little has been done in the field of heterostructures. Recent progress in both the numerical efficiency of algorithms and the computational power of workstations has made it possible to deal with the case of multi-orbital 2D systems, such as the periodic Anderson model. In principle, such a plane involving two electronic orbitals can equivalently describe the coupling of two adjacent planes in which only one orbital is taken into account. It is then tantalizing to go further and try to understand the properties of thicker systems involving more than two atomic planes. Even though the accessible geometries are restricted, by numerical limitations, to a few layers, the perspectives offered by these models to understand better the electronic properties at interfaces or other heterostructures that are already accessible experimentally, make this field very exciting. Because theoretical models allow to explore systematically vast regions of the phase diagrams, such studies could potentially lead to the design of thin films with novel properties.

4.1.2 Metal-Mott Insulator Interface

The properties of the metal-semiconductor junction have been understood since 1938 [95] in terms of a Schottky potential barrier that originates from the difference between the Fermi energy and the valence band of the insulator, and which have been massively applied in electronics for diode fabrication. Much less is known about the interface of a metal with a strongly correlated Mott insulator. This question was addressed for the one-dimensional case by Yonemitsu *et al.* in 2007 [96]. In this work, a strong suppression of the potential barrier was observed when the band insulator is replaced by an organic Mott insulator, and explained by way of a simple 1D Hubbard model. The same

model was recently examined through density-matrix renormalization-group (DMRG) calculations [97] in order to understand the transport properties across the junction, motivated by potential applications of strongly correlated materials to solar cells. This last study found the charge transfer at the interface to be enhanced over the metal-band insulating case. Another DMRG paper had previously unveiled the possibility of creating a two-dimensional electron gas in the proximity of that interface [98].

This interface was subsequently studied in the three dimensional case in terms of a Hubbard model on a cubic lattice at half-filling. The single-site DMFT analysis [99] by Helmes *et al.* has shown the appearance of a quasiparticle peak at the Fermi level in the correlated side that propagates a few unit-cells deep, opening the possibility for an insulator-metal transition driven by the interfacial coupling. They, however, concluded this "Kondo proximity effect" would be eventually defeated by magnetism, which they could not account for through their single-site technique. A spin-wave analysis of a similar $t-J$ Hamiltonian later found an induced magnetic order in the non-interacting side, decaying exponentially from the junction with a correlation length of a few unit cells [100]. Another peculiar feature was found in epitaxially grown superlattices made up of thin layers of the paramagnetic metal $CaRuO_3$ and the antiferromagnet $CaMnO_3$, were ferromagnetism appears [101]. Although controversial, the explanation for this phenomenon was claimed to involve double-exchange, and thus our simple Hubbard model is unlikely to capture this property.

Transport properties at junctions between metals and strongly correlated transition metal oxydes have also attracted much attention in the context of solid-state memory applications, where a resistance switching could be controlled by an electric field. This colossal electroresistance effect was experimentally demonstrated for a broad class of materials [102, 103], and it was also shown that its properties can be tuned by carrier doping [104]. In a recent experiment on a Cu/CuO interface [105], Munakata and coworkers surmised from magnetoresistance measurements showing a quenching of magnetic impurities that a magnetic ordering in the metallic copper side was plausible, and could be explained by a RKKY magnetic interaction mediated by the conduction band.

In the past few years, theoretical work has also investigated a related system, namely a few lattice sizes thick Mott insulating barrier inserted in between two semi-infinite metallic leads. In 2007, a first inhomogeneous DMFT study by Okamoto [106] showed that a paramagnetic Mott insulating barrier in the strong coupling regime has current-voltage characteristics that resemble those of the metal-semiconductor-metal heterostructures. Another DMFT work later

found the appearance of a Fermi liquid phase in the correlated barrier at zero temperature, but also showed this phase was fragile against perturbation, such as disorder and voltage or thermal fluctuations [107], this fragility offering numerous possibilities for applications. In-plane spatial correlations for this model were recently considered in the framework of the Hartree-Fock method [108]. This work showed that in the vicinity of the junction the gap closes in the Mott phase, this effect being suppressed as the Coulomb repulsion U or the thickness of the barrier are increased.

4.2 Metal-Mott insulator interface

In the previous section, we reviewed several works done on the Metal-Mott insulator interface, their most striking feature being the diversity of the results obtained. This is not a surprise, considering that the models and ranges of parameters studied vary considerably. Of similar importance are the peculiarities of the different methods employed, which in general involve intrinsic approximations that are known to generate irrelevant (or even deceptive) features.

Despite its own limitations, the Determinant QMC offers a complementary insight into the field. It can in particular compute the exact thermodynamic properties of the Hubbard model at finite temperatures on finite clusters. The single fact that it often leads, for similar models, to different conclusions than DMFT calculations is valuable, since it allows a critical evaluation of the results produced by both methods. Even though the particular system we will study below does not necessarily bear every feature that should be accounted for in a realistic model, the observation of non-trivial phase transitions in that simple model offers the perspective of further developments.

4.2.1 Hamiltonian

The interface we consider is described by the following Hamiltonian:

$$\begin{aligned}\hat{\mathcal{H}} = & - \sum_{\langle ij\rangle,l,\sigma} t_l\,(c^\dagger_{il\sigma}c_{jl\sigma} + \text{h.c.}) - \sum_{i,\langle ll'\rangle,\sigma} t_{ll'}(c^\dagger_{il\sigma}c_{il'\sigma} + \text{h.c.}) \\ & - \sum_{i,l,\sigma} \mu_l\, n_{il\sigma} + \sum_{i,l} U_l\,(n_{il\uparrow} - \frac{1}{2})(n_{il\downarrow} - \frac{1}{2}).\end{aligned} \tag{4.1}$$

This equation describes, in the grand-canonical formalism, electrons of spin $\sigma \in \{\uparrow,\downarrow\}$ on a cubic lattice whose coordinates are labelled by indeces (i,l) that indicate a site on the layer l with in-plane coordinates i. The layers on the metal side will be labelled with negative integers $l \in \{-1,-2,\dots\}$ while the

correlated layers will bear a positive label $l \in \{+1, +2, \dots\}$. The intra-plane hoppings t_l are chosen to be homogeneously equal to 1 and will be taken as the unit of energy through this chapter. The interlayer hybridizations between sites belonging to adjacent layers $t_{ll'}$ will be chosen to be equal to 1, with the exception of the interface where we define $t_{-1,+1} = V$, which will be the main tunable parameter we will consider. The local Coulomb interaction is zero on the metallic side $U_{l<0} = 0$ and positive on the correlated side $U_{l>0} > 0$. Finally, the chemical potential will be homogeneously set to zero $\mu_l = 0$, putting the system at half-filling and avoiding any numerical sign problem in this work. Unless otherwise mentioned, the case of two non-interacting layers coupled to two interacting ones will be considered. For the sake of clarity, a sketch of the geometry is drawn in Fig.4.2.

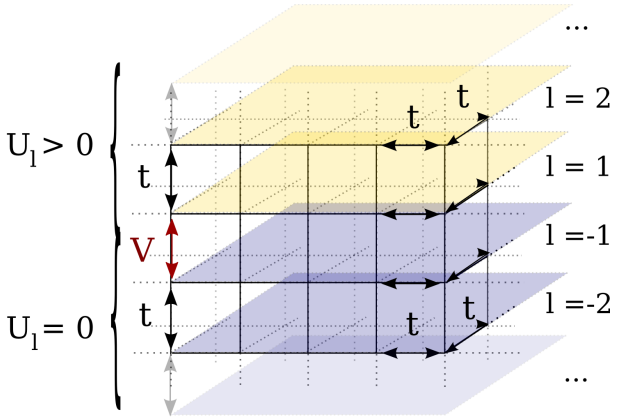

Figure 4.2: Schematic representation of the systems we consider. Nearest-neighbor hoppings are equal to 1 everywhere but across the interface where it is labelled V. Layers with negative indices $l = -1, -2, \dots$, are non-interacting and thus metallic at $V = 0$. A non-zero repulsive interaction $U_l > 0$ is set in the layers with positive indices $l = +1, +2, \dots$. This side is therefore insulating and antiferromagnetically ordered at $V = 0$.

4.3 Spin correlations and singlet formation

In order to understand the major trends in that interface we start by examining the nearest-neighbor spin correlator between layers l and l' (we recall the spin operator σ^x was defined in Eq.(1.42)):

$$c_\perp(l, l') = \langle \sigma^x_{i,l} \sigma^x_{i,l'} \rangle, \tag{4.2}$$

shown in Fig.4.3. Starting from the trivial $V = 0$ case where the two sides are not correlated, the layers right at the interface $(l, l') = (-1, 1)$ acquire an

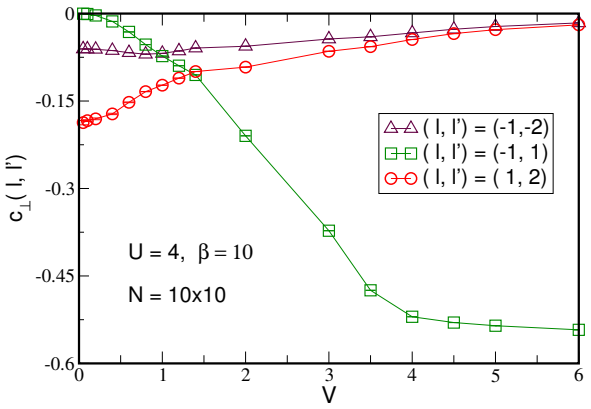

Figure 4.3: Interlayer correlators $c_\perp(l, l')$ as a function of the interface hopping V. As V is increased, the correlator $c_\perp(-1, 1)$ drops, signalling the formation of an interfacial state decoupled from the "bulk". Each layer is 10×10, half filled and at $\beta = 10$.

antiferromagnetic coupling as V is increased. As pairs form, this correlation converges to a value that characterizes the singlet state formed between each pair of sites across the interface. This singlet formation goes along with the decoupling of the outer layers: the spin correlation with the adjacent interfacial layer starts from a non-zero value at $V = 0$, this value being higher on the correlated side because of its antiferromagnetic order. As V is increased and singlets are formed, the spin correlation vanishes on both sides. This leads us to the picture, at large V, of a two-layer strongly coupled interface that does not "see" the bulk anymore.

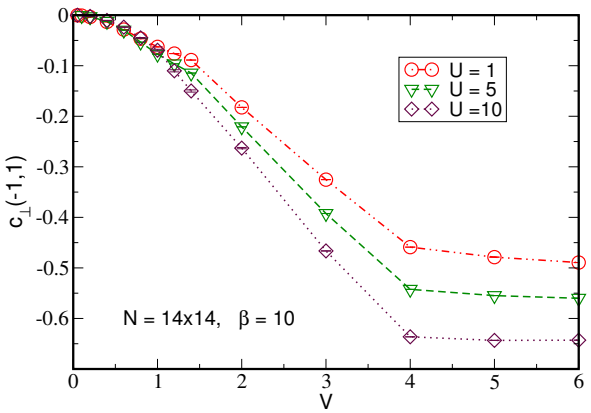

Figure 4.4: Spin correlation between sites across the interface $c_\perp(-1, 1)$ for different values of the interaction U. The spin correlation at large V depends on U, which suppresses double occupancy.

We draw in Fig.4.4 the spin correlations between sites across the interface for different values of the interaction U. It shows the striking feature that singlet formation does not strongly depend on the interaction, the antiferromagnetic correlation converging to its strong coupling value around $V = 4$. It is important to note that the singlet pairs that are formed in the large-V limit differ by their amount of double occupancy (or equivalently by the local moment formation), which is dependent on the strength of the interaction on the correlated side. When U is large, the antiferromagnetic coupling is thus larger because local moments are enhanced.

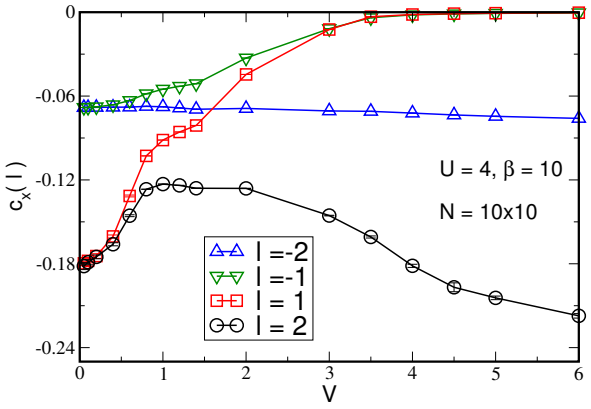

Figure 4.5: In-plane spin correlations as a function of V. In the outer metallic layer $l = -2$ correlations are not affected by the evolution of the interface, while in the outer interacting layer $l = 2$ correlations at first drop along with the interfacial layer $l = 1$ before decoupling. At large V both layers at the interface have vanishing in-plane correlation, signalling the dimers are decoupled from one another.

This scenario is confirmed by examining the near-neighbor spin correlator $c_x(l) = \langle \sigma^x_{i,l} \sigma^x_{i+1,l} \rangle$ within each layer l (Fig.4.5). When $V = 0$, the sites in the metal are only slightly antiferromagnetically coupled, which maximizes the kinetic energy since no hopping is possible between two neighbor electrons of the same species because of the Pauli principle. On the other side, the Mott insulator has a much larger antiferromagnetic correlation as expected in an ordered phase. Surprisingly, the spin correlations in both antiferromagnet layers at first drop upon increasing V. Right at the interface the in-plane correlation eventually becomes zero, signalling that in the strong coupling limit the singlets at the interface are independent of each other. Interestingly, the outer correlated plane experiences non-monotonic evolution in which, after first decreasing, it recovers its short-range antiferromagnetic correlation. The outer metal plane is not significantly affected by the tuning of the interfacial

hybridization.

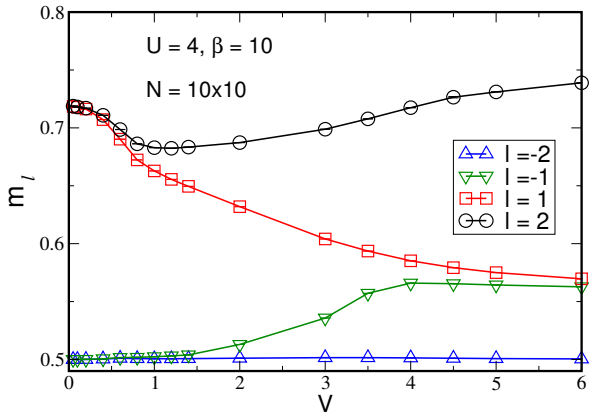

Figure 4.6: V-dependence of local moments, $m_l = \sum_i \langle (\sigma_{il}^z)^2 \rangle / N$, on each layer, when two metallic layers are coupled to two correlated ones. As dimers form at the interface, moments in the outer interacting layer increase due to the decoupling from the interface.

These observations are supported by the evolution undergone by the local moments (Fig.4.6). The layers at the interface are driven to a common value characteristic of the singlet pairs they form, the behavior of the outer Mott plane is non-monotonic with moments being at first suppressed before recovering, while electrons in the outer metallic plane remain essentially non-localized.

4.4 Suppression of magnetic order

We just saw how the short range correlations are modified upon tuning the hybridization across the interface. The next question we address is what happens to the long-range order that exists in the Mott phase prior to connecting it to the metal side. The antiferromagnetic structure factor (AFSF) was defined as $S^{\rm af}$ in Eq.(1.43), and characterizes the magnetic order. The dependence of $S^{\rm af}$ on V is plotted in Fig.4.7 for the case of a relatively large lattice ($N = 14 \times 14$). While the layers in the metal side $l < 0$ remain clearly disordered (not needing any finite-size scaling), the AFSF in the correlated side drops abruptly in both layers as soon as V is increased. After reaching a minimum around $V \approx 1.5$ the outer correlated layer $l = 2$ recovers a high signal as V gets larger. Concurrently, the interfacial correlated layer $l = 1$ remains disordered as singlet pairs destroy moments, thus preventing direct exchange.

As usual it is necessary to perform a finite-size scaling in order to determine whether the structure factor converges in the thermodynamic limit to a finite

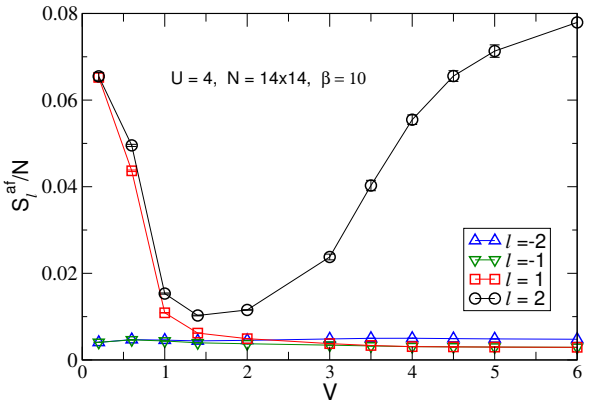

Figure 4.7: In-plane antiferromagnetic structure factors $S_l^{\rm af}$ is shown as a function of the interface hopping V. For $l = -1, -2$ (metallic sheets) S_l^{af} remains small for all V. For $l = 1, 2$, S_l^{af} decreases indicating suppression of AF order but then recovers for $l = 2$.

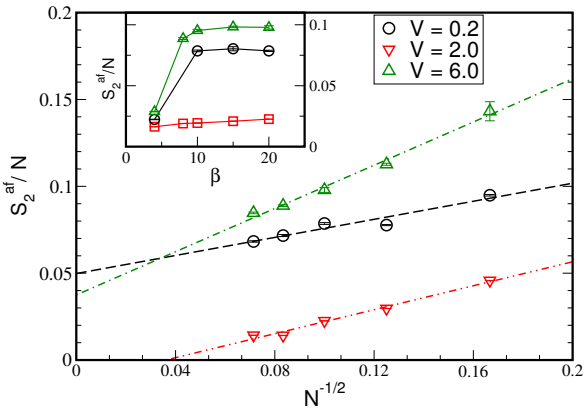

Figure 4.8: Finite size scaling of in-plane structure factor $S_2^{\rm af}$ of the correlated layer ($l = 2$) farthest from the interface. For small V, there is long range order in the thermodynamic limit which vanishes for intermediate V and is recovered for large V. The inset shows the inverse temperature dependence for a 10×10 layer. $S_2^{\rm af}$ reaches its ground state value at $\beta = 10$.

order parameter. This extrapolation for the outer correlated layer $l = 2$ is shown in the main panel of Fig.4.8. This analysis confirms the actual vanishing of magnetic order at $V = 2.0$, as well as its resurgence in the large coupling limit. The inset of Fig.4.8 shows the convergence of the AF structure factor upon decreasing the temperature, validating the choice of $\beta = 10$ for this study.

We also investigated whether this non-monotonic magnetic behavior of the outer Mott plane is found for other choices of the on-site repulsion $U_{l>0}$ in the

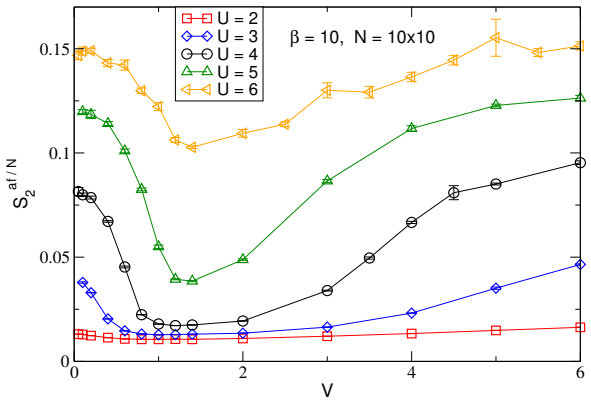

Figure 4.9: The behavior of the AF structure factor in the outer correlated layer S_2^{af} as a function of V depends on U, for $2+2$-layers systems. From $U \gtrsim 6$, the magnetic order does not vanish at intermediate V although it is somewhat suppressed. Each plane is 10×10 and half-filled with $\beta = 10$.

range $U \in [2t, 6t]$. As shown in Fig.4.9, this phenomenon is observed on a rather broad range. At weak interaction, thermal fluctuations make the AF structure factor small, including at small V, even though we know magnetic order is to be expected at any $U > 0$ because of the nesting of the Fermi surface. As U is increased, the range in which suppression of magnetic order occurs gets smaller. Although performing finite-size extrapolation was beyond the possibilities of this study, there seems to be no complete vanishing of order from $U \approx 6$ but, instead, a mere suppression of the order parameter. Since a derivation of one-band Hubbard models for Cu-O cuprate planes estimated the local Coulomb repulsion to be of the order of the bandwidth $W \approx 8t$ [109], the suppression of magnetism should be looked for in weaker Mott insulators, like organic compounds.

4.5 Spectral functions

The previous findings indicated the existence, at intermediate coupling, of a phase in which the whole system is disordered, including the planes that are not directly in contact with the interface. This phase is an intermediate state before the interface is driven into strongly correlated dimers that decouple from the outer layers. To characterize better the different phases, we now investigate the spectral functions $A_l(\omega)$ in each plane (Fig.4.10) for three values of V corresponding to each regime. The definition of the spectral function can be found in Eq.(1.54).

The outer correlated layer (Fig.4.10a) is initially gapped, as expected from

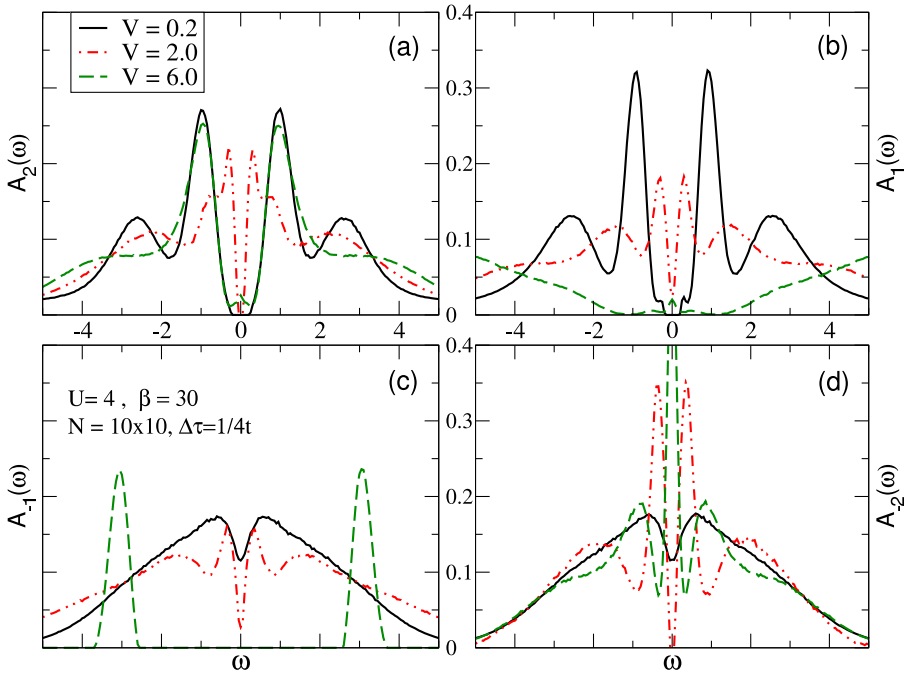

Figure 4.10: (a) Spectral function $A_2(\omega)$ in correlated layer $l = 2$. The Slater gap present at small V due to AF order vanishes at intermediate V and reappears at larger V. (b) In correlated layer $l = 1$, $A_1(\omega)$ resembles $A_2(\omega)$ but unlike $l = 2$ the large V behavior is a broader gap associated with the singlet energy scale. In both non-interacting layers $A_{-1}(\omega)$ (c) and $A_{-2}(\omega)$ (d) a gap opens as V increases. At large V, layer -2 recovers metallic properties while the singlet gap is visible in layer -1.

a Mott insulator. The two external peaks correspond to the Mott gap whose width corresponds to the energy cost of double occupancy $U = 4$. This gap is narrowed due to antiferromagnetic order to a so-called Slater gap. At intermediate $V = 2.0$, the plane remains insulating but the gap is smaller. Finally at strong coupling the initial gap is recovered as the plane decouples from the interface. In the interfacial correlated layer (Fig.4.10b) the evolution is at first similar: the Slater gap shrinks upon increasing V as the system becomes disordered. However, at strong coupling singlet formation leads to a large gap that corresponds to the amount of energy needed to break the singlet pairs $E \approx V$.

We turn now to the spectral properties on the metallic side. In the non-interacting two-dimensional case a Van Hove singularity is present at the Fermi level. Here at $V = 0.2$ a dip in the density of states foreshadows the appearance of a gap in the intermediate phase. At strong coupling the singlet gap is perfectly visible. The outer non-interacting plane shows roughly the same

behavior at small and medium coupling, while a peak at the Fermi level at $V = 6.0$ illustrates the decoupling from the interface and the recovery of metallic properties.

4.6 dc Conductivity

Since the dc conductivity, which was defined in Eq.(1.59), is experimentally measured within a whole sample, the in-plane conductivity in a monolayer of an heterostructure is not likely to be accessible. The total conductivity will involve the sum of all intra-layer and inter-layer contributions. However, accessing the in-layer conductivity is relevant in order to understand accurately the underlying microscopic transport properties.

The in-plane dc conductivities in each layer of the $(2+2)$-system are presented in Fig. 4.11, as a function of the interface hybridization V. These measurements were performed at several temperatures in order to check qualitatively the convergence in the low-temperature limit: when the conductivity increases upon lowering the temperature one expects a metallic ground-state, while if the conductivity decreases the ground-state should be insulating.

Let us first consider the conductivity in the non-interacting layer located right at the interface (Fig.4.11c). When the coupling to the interacting side is small ($V = 0.2$) the conductivity increases upon lowering the temperature from $\beta = 8$ to $\beta = 16$, signalling the metallicity of the layer. As the interface coupling is increased the conductivity drops down to small values, and now decreases with the temperature, thus clearly signalling an insulating state at $V = 1.0$. This insulating transition is concomitant with the magnetic transition we previously described. Interestingly, as the coupling at the interface is further enhanced the conductivity rises slightly and seems to tend to a small but finite value at low temperature. As the singlet gap opens around $V = 4.0$ the conductivity eventually goes to zero, since moving a particle in that regime requires a finite energy in order to break a dimer.

The outer non-interacting layer (Fig.4.11d) shows a similar drop in the conductivity as the interface hybridization is increased, the layer being driven from metallic to insulating. However, the intermediate small finite conductivity in the $V = 2.0$ vicinity is not observed, the conductivity decreases along with the temperature signalling the layer is insulating. As the singlet gap opens, the outer layer decouples from the interface and becomes conducting again. The values of the conductivity are significantly larger in that latter regime than at small V, which can be explained by the high density of carriers in the two-dimensional case because of the Van Hove singularity.

Fewer features are observed on the correlated side. The outer layer (Fig.4.11a) remains always insulating, the slight increase at $V = 4.0$ being likely a spurious artefact. At the interface (Fig.4.11b), the conductivity seems nonetheless to converge to a non-zero value in the range $V \approx [1.5, 3.5]$ as in the adjacent non-interacting layer, before entering in the gapped singlet regime. Even though a more careful analysis would be required to enable any strong statement on the nature of these phases, a disordered state made of strongly coupled dimers and displaying a small finite conductivity seems reminiscent of the large effective masses found in similar models describing heavy-fermion behaviour. It would be particularly interesting to study the temperature scaling of the resistivity, which is known to be linear over several decades of energy in these systems [110].

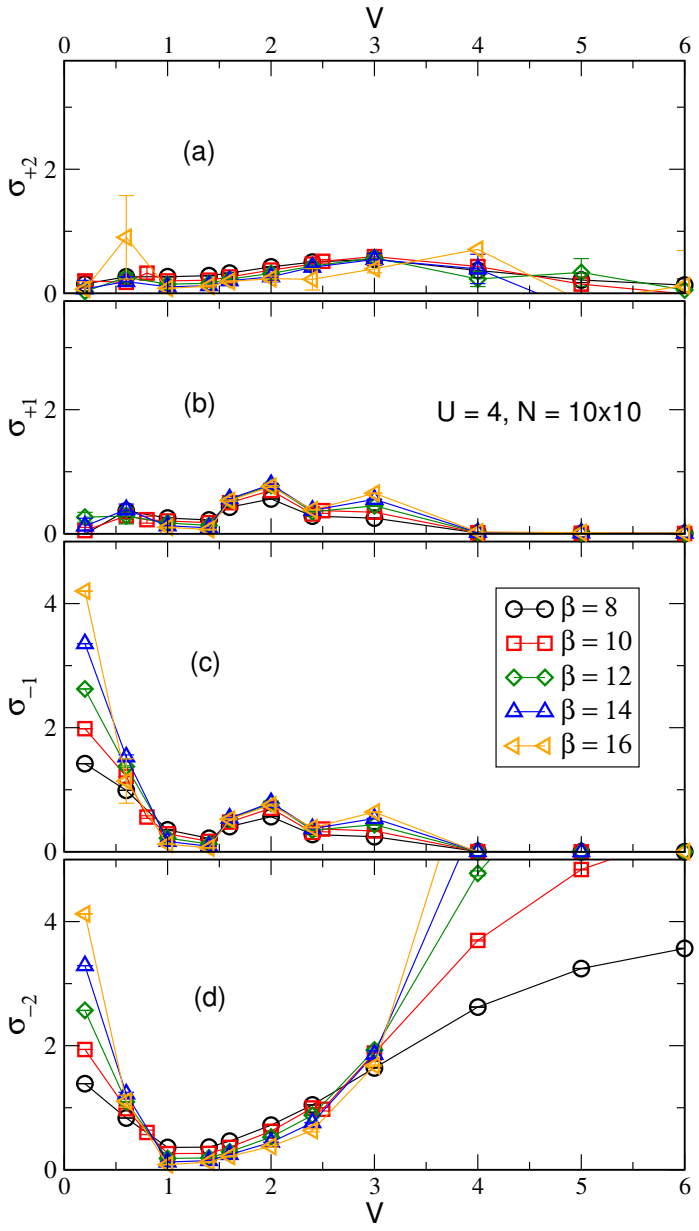

Figure 4.11: In-plane conductivities in the $2+2$-layer case as functions of V, at several inverse temperature β values: (a) The outer interacting layer σ_{+2} is always insulating, while in (b) the interacting layer at the interface the conductivity σ_{+1} seems, in the intermediate regime, to converge to a finite value in the low-T limit. Panel (c) shows the conductivity σ_{-1} in the metallic layer $l=-1$. At intermediate V is small but non-zero, but vanishes at $V \geq 4t$ due to dimer formation. (d) The in-plane conductivity σ_{-2}. This noninteracting layer becomes insulating for intermediate hybridization, $t \leq V \lesssim 3t$ and then recovers when the pairs are fully formed and pinned at the interface.

4.7 More layers

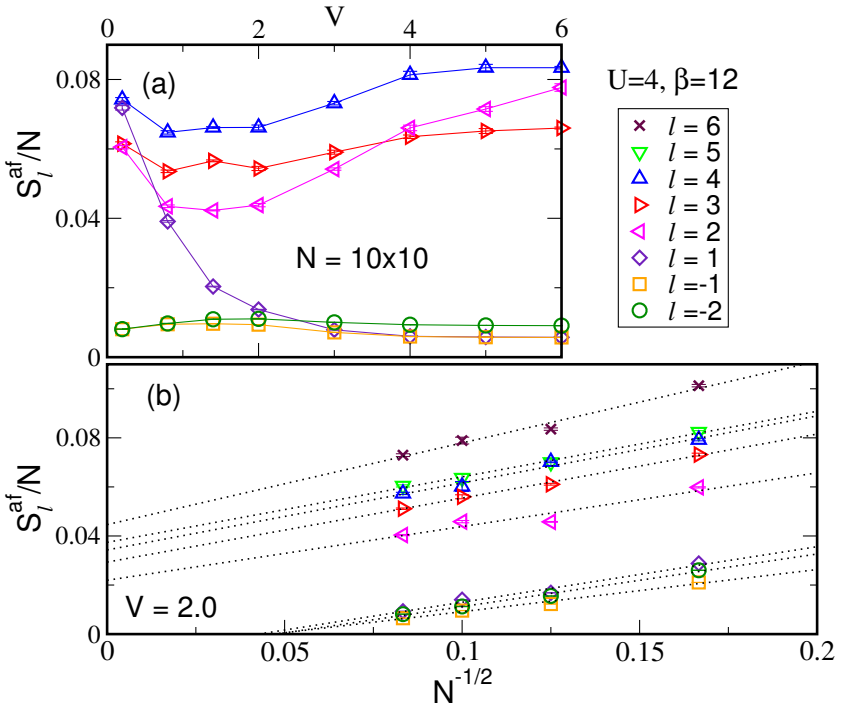

Figure 4.12: (a) In-plane structure factors $S_l^{\rm af}$ as functions of V for a system of four correlated layers coupled to two metallic ones. At intermediate V antiferromagnetic order is suppressed in every correlated layer. At large V the order recovers in every correlated layer but the one at the interface. (b) Finite-size scaling of the in-plane structure factors $S_l^{\rm af}$ for a system of six correlated layers coupled to two metallic ones, at $V = 2t$. A systematic reduction of spin correlations is evident as the metallic interface is approached from the correlated side. Long range magnetic order is completely destroyed in the correlated layer at the junction.

The model we presented so far is four atomic layers thick. Although we addressed the question of the finite-size effects in the xy-plane and believe to have demonstrated that this is under control, the possibility of exploring accurately the penetration of the phenomena we described into the bulk of the model material is well beyond our reach. Nevertheless, we have been able to measure static properties for systems made of up to six Mott insulating layers, while keeping the metal two-layers thin. The latter choice was driven by the observation that no major penetration was seen even in the second metallic layer, and consequently we believe the expansion of the metal side would not affect significantly the system.

Fig.4.12 represents the evolution of the AF structure when V is increased; we first focus on the Mott side. The layer right at the interface undergoes an evolution similar to the one depicted in the thin case: the AF signal drops until reaching a small value that excludes the possibility of long-range magnetic order. One might argue the convergence toward this limit is slower than in the case with only two Mott layers, but this statement would require an extrapolation to the thermodynamic limit. More interesting is the point that the decrease of the structure factor in the layer adjacent to the interfacial one is much reduced in comparison with the thinner case. The finite-size extrapolation presented in Fig.4.12 demonstrates that at $V = 2.0$ the order parameter is indeed suppressed at the interface but never vanishes, while magnetic order is restored upon entering the bulk.

No sign of enhanced order is observed in the metallic side; this is non-trivial since the additional interacting layers protect now the magnetism in the layer next to the interface: one could have instead envisaged, for instance, a consequent ordering in the metal. It is also interesting to note that in "outer" magnetic layers the AF structure factor takes a larger value than in "inner" layers. This is due to the fact magnetic correlations are enhanced at surface in comparison to the bulk, as it has previously shown experimentally [111].

4.8 Summary

In this chapter, we presented results obtained by determinant QMC simulations for a metal-Mott insulator interface model. Attention was mostly given to the case of two single non-interacting layers coupled to two Mott insulating layers and, among the large number of parameters of the problem, we mostly focused on the role of the hybridization V between sites across the interface (see Fig.4.13).

Two distinct phase transitions were found to occur upon increasing V. Starting from the decoupled system $V = 0$, in which the sides are respectively a paramagnetic metal and insulating antiferromagnet, increasing the interfacial coupling causes the magnetic order to vanish on the correlated side. This loss of magnetism is accompanied by a drop in the conductivity of the metallic side, leading to an intermediate state in which the whole thin interface is in a non-magnetic insulating state (Fig.4.14). It is particularly interesting that such a transition can be driven, by only tuning the interfacial coupling, into layers that are not directly located at the junction. The nature of this intermediate state is also intriguing, and differs strikingly from other theoretical predictions that forecasted instead an antiferromagnetic ordering in the metal

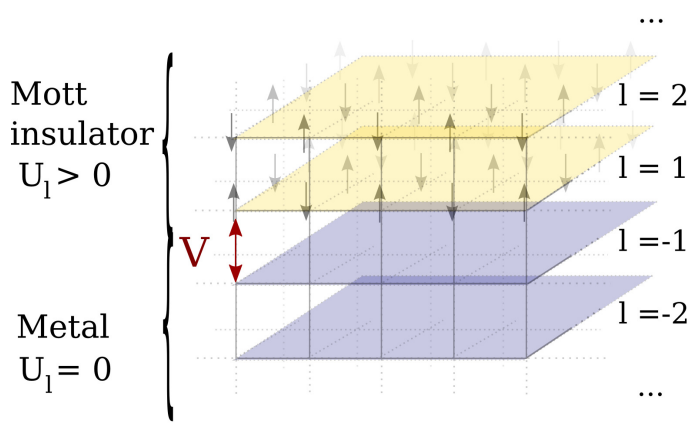

Figure 4.13: Sketch of the decoupled system at $V \ll 1$.

[100] and the appearance of a quasi-particle peak in the correlated material [99]. A further characterization of this phase could be achieved by performing different measurements (for example dimer-dimer correlations), or by examining the effect of doping which is expected to lead to heavy-fermion physics. Checking the behaviour of different geometries, like the honeycomb lattice, would also allow to understand to which extent this phenomenology is owed to the peculiarities of the cubic lattice.

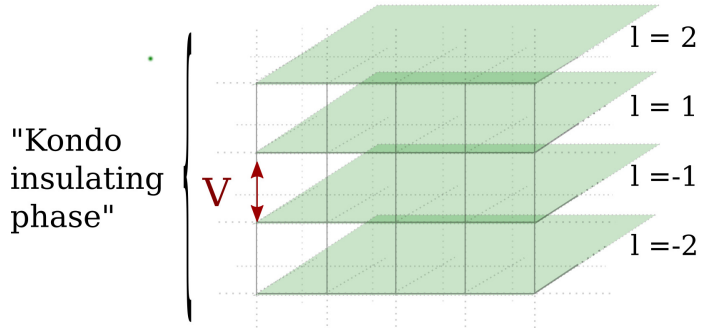

Figure 4.14: At $V \approx 1$, the four layers are disordered and insulating, despite the important difference of local moment formation between both sides.

When the hybridization V is further increased, pairs of adjacent sites at the interface form singlet dimers that are essentially decoupled one from another (Fig.4.15). While this singlet formation was to be expected, the simultaneous decoupling of the outer layers from the interface, accompanied by the recovering of their initial properties, is a non-trivial effect.

The suppression of the magnetism in the outer correlated layer was shown

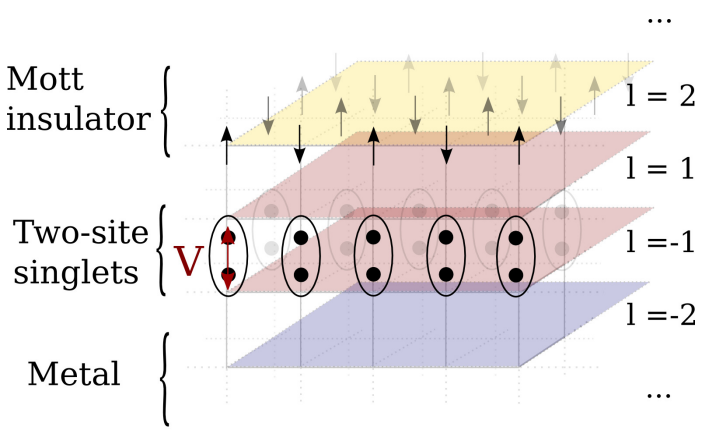

Figure 4.15: When the interlayer coupling at the interface V is large, dimers are former and lead to the decoupling of the interface from the exterior layers, the latter recovering their initial properties (respectively an uncorrelated metal and a magnetic insulator).

to occur within a relatively broad range of on-site repulsion, but that increasing this interaction eventually leads to a simple suppression of the antiferromagnetic order parameter instead of its vanishing. We finally considered the case of a thicker Mott insulating side by studying up to eight correlated layers coupled to two metallic one. The additional layers were observed to protect the magnetism in the vicinity of the interface, leading also to a suppression of the magnetism instead of its vanishing.

Conclusion

The focus of this work was to explore the properties of electrons in systems whose geometry consists of coupled layers. The motivation for studying such geometries arises from two fields. First, to describe the properties of two-dimensional systems in which more than a single electronic band is taken into account. Second, to understand the electronic reconstruction that happens when two complex materials are coupled at an interface. In that context, our approach consisted of studying numerically different systems based on the Hubbard model, a milestone in theoretical condensed matter physics, that had success in capturing fundamental behavior of some phase transitions found in strongly correlated materials, such as metal-insulator transitions driven by electron-electron interaction. The numerical method we use, the Determinant Quantum Monte Carlo (DQMC), allows to explore accurately this model in finite-size clusters. In spite of its limitations, mostly due to the so-called numerical sign problem, the possibility of accounting for spatial correlations was shown in Chapter 2 to be crucial, and offers a remarkable advantage of DQMC over other methods used in this field. The finite-temperature version we employ allows to describe the effect of thermal fluctuations in the phase diagram, providing a deeper insight into the physics of these systems as was illustrated in Chapter 3.

A simple example of a multi-band structure is a band insulator, whose Fermi energy lies in the finite gap that splits the valence and the conduction bands. The geometry we studied in Chapter 2 is a model of a correlated band insulator, in which the non-interacting gap can be tuned by a simple parameter. An electronic interaction, namely an homogeneous on-site Coulomb repulsion, is the other parameter whose effect we chose to explore. This model had recently attracted interest and had been claimed to display a shrinking of the single-particle gap upon increasing the electronic interaction. Such behavior is highly non-trivial, since in the textbook example of the Mott transition, the interaction is known to control the inverse transition by driving the non-interacting metal into an insulating state. However, the recent discovery of an intermediate metallic phase in a similar system with an identical non-interacting dispersion relation, the ionic Hubbard model (IHM), opened the door to this possibility. In spite of these results, our analysis showed unambiguously that the consideration of spatial correlations does not lead to a narrowing of the single-particle gap, but rather to its monotonic growth. However, the

spin gap was observed to shrink upon increasing the interaction, and eventually to close at the transition as magnetic order sets in. The evolution of the local moments, in which an inflexion point characterizes the Mott transition, was shown to decouple from the magnetic transition where long-range order settles. The possibility for an intermediate paramagnetic correlated phase was thus open, even though its characterization was beyond the scope of our study. The absence of an intermediate metallic phase is a striking difference with the IHM that is due to the spatial homogeneity of our model, in which the band gap stems from singlet formation.

Multi-band models are also known to be essential in order to capture the subtle physics found in heavy-fermion compounds. These materials are characterized by the presence of localized magnetic moments whose coupling to the conduction electrons gives rise to a Kondo resonance, leading to intriguing properties such as huge effective electronic masses. The standard framework used to account for these phenomena is the periodic Anderson model (PAM), in which a periodic array of interacting localized electrons is coupled to a non-interacting conduction band. In Chapter 3, we extended this model by systematically exploring the effect of a finite nearest-neighbor hopping t_f in the interacting band, thus interpolating the problem of the PAM with the case of a bilayer Hubbard model. By allowing t_f to have an opposite sign to the conduction band hopping, the non-interacting limit of this model was also directly connected to the band insulator we presented in Chapter 2. A complex phase diagram was unveiled, showing in particular how the direct exchange allowed by the finite bandwidth leads to maximize local and long-range magnetic properties at $t_f \approx 0.2$. The analysis of the spectral functions allowed to reveal how the different energy scales compete in the model, displaying in particular a splitting of the Kondo resonance when antiferromagnetic order settles.

The bilayer model we studied in Chapter 3 can equivalently be thought of as the junction between a correlated material and a metal, providing a direct connection to the problem of oxide heterostructures. Thus, it was tantalizing to address the question of how the evolution of the interface upon tuning the coupling will affect the properties deeper into the materials. In addition, similar realizations of metal-Mott insulator interfaces have been studied during the past years, unveiling non-trivial and controversial properties. Chapter 4 was consequently devoted to the study of this interface, fixing $t_f = 1$ for simplicity and focusing on the effect of the interfacial hybridization V. In contrast with previous work, we found that the magnetic order in the correlated side vanishes upon increasing V, while no order appears in the metal. This effect is observed to occur not only in the layer located at the interface, the adjacent layer also becomes paramagnetic. Upon further increasing V, singlet pairs form

across the interface as the outer correlated layer recovers its antiferromagnetic long-range order. The intermediate paramagnetic phase is also characterized by the appearance of a single-particle gap in the metallic side, leading to an intermediate homogeneous phase displaying no magnetic order and insulating properties. The role of the interaction strength on the correlated side was also investigated, and showed that a strong interaction leads to a suppression of magnetism instead of its vanishing. The case of a thicker correlated side was finally considered, showing that the additional correlated layers protect by proximity effect the magnetism in the vicinity of the interface.

These three studies demonstrate the broad variety of layered systems accessible through the Determinant Quantum Monte Carlo formalism. In spite of certain constraints such as the difficulty to investigate doped phases, the flexibility of this algorithm provides access to geometries that are beyond the reach of most analytical and numerical techniques. The ability to explore broad regions of the phase diagram of a given system allows to capture the qualitative behavior of, in principle, any observable of interest. Obviously, studying extensive sets of parameters puts limits to the size of the cluster, but performing finite size scaling for a few distinctive points allows to control the accuracy of the calculations.

Given the perspectives offered by the field of heterostructures, a number of extensions of our work are worth considering. For instance, the interface we studied had open boundary conditions in the direction orthogonal to the layers: by setting periodic boundary conditions, the problem of heterostructures made of periodic arrangement of layers could be addressed. The question of the transport properties across the layers could concurrently be studied. Synthesis and characterization of a wide variety of such structures are presently performed, and the choice of the geometry and parameters could aim at understanding specific experiments.

We restricted the geometries of our systems to the cubic lattice. Although configurations involving geometric frustration are not accessible to DQMC because of the numerical sign problem, considering other bipartite geometries could be interesting. In particular, the bidimensional honeycomb lattice offers the advantage of needing a finite critical interaction for the Mott metal-insulator transition. The role of the peculiarities of the square lattice could thus be determined. Additionaly, the honeycomb lattice bears its own characteristics, such as a linear dispersion in the vicinity of the Fermi energy that results in “Dirac cones”. The case of coupled graphene planes is an example of the problems that could be explored with this lattice.

Conclusion en français

> "Et cependant, notre prédiction s'est complètement réalisée, le bâton à physique a fait des merveilles [...]."
>
> — Alfred Jarry [1]

Ce travail a porté sur l'étude des propriétés d'électrons dans des systèmes composés de couches minces couplées. L'intérêt pour de telles géométries provient de deux domaines. D'une part, la description des propriétés de systèmes bidimensionnels dans lesquels plusieurs bandes électroniques sont prises en compte. Deuxièmement, comprendre les "reconstructions" électroniques qui ont lieu lorsque deux matériaux complexes sont en contact à une interface. Dans ce contexte, notre approche a été d'étudier numériquement différents systèmes basés sur le modèle de Hubbard, un important modèle en théorie de la matière condensée qui a permis de saisir le mécanisme fondamental de certaines transitions de phase des matériaux fortement corrélés, comme la transition métal-isolant engendrée par des interactions électron-électron. La méthode numérique que nous employons, le Monte Carlo Quantique du Déterminant (DQMC), permet d'explorer avec précision ce modèle pour des *clusters* de taille finie. Malgré certaines restrictions, dues pour la plupart au "problème du signe", nous avons montré que la possibilité de rendre compte des corrélation spatiales est cruciale, et offre un avantage remarquable par rapport à d'autres méthodes utilisées dans ce domaine. La version à température finie que nous utilisons permet la description l'effet des fluctuations thermiques dans le diagramme de phase, apportant une meilleure compréhension de la physique de ces systèmes comme nous l'avons illustré au Chapitre 3.

Un exemple simple de structure de bande électronique est l'isolant de bande, dans lequel l'énergie de Fermi se situe dans le *gap* d'énergie séparant les bandes de valence et de conduction. gap à interaction nulle peut être ajusté au moyen d'un simple paramètre. Une interaction électronique, plus précisément une répulsion Coulombienne sur site, est l'autre paramètre dont nous avons étudié l'effet. Ce modèle a été récemment étudié, et il a été en particulier affirmé que la largeur du gap pouvait être réduite en augmentant la valeur de l'interaction électronique. Un tel scénario est hautement non-trivial, les interactions étant connue dans l'exemple classique de la transition de Mott pour au contraire rendre isolant un système métallique. Cependant, la découverte récente d'une phase conductrice intermédiaire dans un système similaire

et ayant une relation de dispersion identique, le modèle ionique de Hubbard (IHM), avait ouvert la porte à une telle eventualité. Malgré ces résultats, notre analyse a montré sans ambiguïté que la prise en compte des corrélations spatiales ne conduit pas à un rétrécissement du gap, ce dernier croissant de façon monotone. Cependant, nous avons montré que le gap de spin se réduit lorsque l'interaction est augmentée, pour finalement se fermer lorsque la transition magnétique a lieu. L'évolution du moment magnétique, au cours de laquelle un point d'inflexion signale la transition de Mott, se découple de la transition magnétique caractérisée par un ordre à longue distance. La possibilité d'une phase intermédiaire paramagnétique est donc envisageable, bien que sa caractérisation ait été hors de la portée de notre étude. L'absence d'une phase métallique intermédiaire constitue une différence frappante par rapport au IHM due à l'homogénéité spatiale de notre modèle, pour lequel le gap d'énergie provient de la formation de singulets entre les bandes.

Les modèles comprenant plusieurs bandes électroniques sont également importants pour saisir la physique des composés à "fermions lourds". Ces matériaux sont caractérisés par la présence de moments magnétiques locaux dont le couplage avec la bande de conduction entraîne une "résonance de Kondo", conduisant à des propriétés telles que des masses effectives considérables. Le cadre habituel pour rendre compte de ces phénomènes est le modèle périodique de Anderson (PAM), dans lequel un réseau périodique d'électrons localisés par une interaction est couplé à une bande conductrice sans interaction. Dans le Chapitre 3, nous avons étendu ce modèle en explorant systématiquement l'effet d'un terme de saut entre plus proches voisins t_f dans la bande avec interaction, ce qui correspond à interpoler le PAM avec un modèle de Hubbard à deux bandes. En permettant à t_f de prendre un signe opposé à celui de la bande de conduction, la limite sans interaction de ce modèle a été directement reliée au problème de l'isolant de bande présenté au Chapitre 2. Nos résultats ont conduit à un diagramme de phase complexe, montrant comment le couplage direct permet de maximiser les corrélations magnétiques locales et à longue distance aux alentours de $t_f \approx 0.2$. L'étude des fonctions spectrales révèle les différentes échelles d'énergie en jeu dans le modèle, avec en particulier l'apparition d'un gap divisant la résonance de Kondo lié à l'établissement de l'ordre antiferromagnétique.

Le modèle bicouche que nous avons étudié au Chapitre 3 peut décrire de façon équivalente la jonction entre un matériau corrélé et un métal, fournissant une connection directe avec le problème des hétérostructures d'oxydes. Il était donc tentant de poser la question de comment l'évolution d'une telle interface affecte les propriétés à l'intérieur des matériaux. De plus, des réalisations d'interfaces métal-isolant de Mott ont été étudiées au cours des dernières an-

nées, laissant entrevoir des propriétés non-triviales et controversées. Nous avons donc étudié cette interface dans le Chapitre 4, en choisissant pour simplifier $t_f = 1$ et en se concentrant sur le rôle du couplage à l'interface V. En contradiction avec certains travaux réalisés précédemment, nous avons observé que l'ordre magnétique du côté corrélé est détruit lorsque V est augmenté, tandis que le côté métallique reste désordonné. Cet effet est visible non seulement dans la couche située directement à l'interface, mais également dans la couche corrélée adjacente qui devient elle aussi paramagnétique. Lorsque la valeur de V est encore augmentée, des singulets sont formés à travers l'interface tandis que la couche corrélée extérieure retrouve ses propriétés antiferromagnétiques. L'état paramagnétique intermédiaire est également caractérisé par l'apparition d'un gap d'énergie dans le côté métallique, résultant en une phase intermédiaire homogène qui est isolant et dépourvue d'ordre magnétique. Le rôle de la valeur de l'interaction a également été étudié, montrant qu'une forte interaction conduit à une diminution de l'ordre magnétique au lieu de sa disparition. Le cas d'une épaisseur plus importante du côté corrélé a finalement été considéré, montrant que les couches corrélées supplémentaires protègent par un "effet de proximité" le magnétisme au voisinage de l'interface.

Ces trois études démontrent la grande diversité de systèmes en couches accessible par la méthode du DQMC. Malgré certaines contraintes, en particulier la difficulté à explorer les phases dopées, la flexibilité de cet algorithme permet d'accéder à des géometries hors d'atteinte de la plupart des méthodes analytiques et numériques existantes. La possibilité d'explorer de vastes région du diagramme de phase d'un système donné permet de saisir le comportement qualitatif de n'importe quelle observable d'intérêt. Naturellement, l'étude de nombreux jeux de paramètres implique de limiter la taille des clusters considérés, mais la possibilité d'extrapoler dans la limite thermodynamique pour certains points particuliers permet de contrôler la validité de ces résultats.

Au regard des possibilités offertes par le domaines des hétérostructures, différentes extensions de ce travail sont à considérer. A titre d'exemple, l'interface que nous avons étudié avait des conditions aux bords ouvertes dans la direction perpendiculaire aux couches minces. En imposant des conditions périodiques, le problème d'hétérostuctures constituées d'arrangements périodiques de couches pourrait être attaqué. La question des propriétés de transport à travers ces couches pourrait être étudiée en parallèle. La synthèse et la caractérisation d'une grande variété de telles structures étant actuellement en cours, le choix d'une géométrie et de paramètres pourrait viser à comprendre certaines expériences.

Nous avons restreint les géométries des systèmes considérés au cas du réseau cubique. Bien que les configurations qui impliquent une frustration

géométrique ne soient pas accessibles par la méthode du DQMC à cause du problème du signe, l'étude d'autres réseaux bipartites serait intéressante. En particulier, le réseau "en nid d'abeille" offre l'avantage d'une transition de Mott à interaction finie. Le rôle joué par les spécificités du réseau carré pourraient par conséquent être déterminées. De plus, le réseau "en nid d'abeille" possède ses propres particularités, comme une relation de dispersion linéaire au voisinage de la surface de Fermi qui entraîne l'existence de "cônes de Dirac". Le cas de plans de graphène couplés pourrait par exemple être étudié.

Bibliography

[1] A. Jarry. *Ubu roi: drame en cinq actes*. E. Fasquelle, 1963. (Cited on pages 5 and 91.)

[2] G.D. Mahan. *Many Particle Physics*. Physics of Solids and Liquids. Springer, 2000. (Cited on page 10.)

[3] P. Coleman. *Introduction to Many Body Physics*. Cambridge University Press, 2013. (Cited on page 10.)

[4] P. Fulde. *Correlated electrons in quantum matter*. World Scientific Publishing Company, Incorporated, 2012. (Cited on page 14.)

[5] A. Auerbach. *Interacting electrons and quantum magnetism*. Graduate Texts in Contemporary Physics Series. Springer New York, 1994. (Cited on page 15.)

[6] R. Blankenbecler, D. J. Scalapino, and R. L. Sugar. Monte Carlo calculations of coupled boson-fermion systems. I. *Phys. Rev. D*, **24**:2278–2286, Oct 1981. (Cited on pages 18 and 26.)

[7] EY Loh Jr and JE Gubernatis. Stable numerical simulations of models of interacting electrons in condensed-matter physics. *Modern Problems of Condensed Matter Physics*, **32**:177, 1992. (Cited on page 18.)

[8] S. R. White, D. J. Scalapino, R. L. Sugar, E. Y. Loh, J. E. Gubernatis, and R. T. Scalettar. Numerical study of the two-dimensional Hubbard model. *Phys. Rev. B*, **40**:506–516, Jul 1989. (Cited on page 18.)

[9] J.W. Negele and H. Orland. *Quantum Many-particle Systems*. Advanced book classics. Perseus Books, 1998. (Cited on page 19.)

[10] E. Y. Loh, J. E. Gubernatis, R. T. Scalettar, S. R. White, D. J. Scalapino, and R. L. Sugar. Sign problem in the numerical simulation of many-electron systems. *Phys. Rev. B*, **41**:9301–9307, May 1990. (Cited on page 20.)

[11] Ghassan George Batrouni and Philippe de Forcrand. Fermion sign problem: Decoupling transformation and simulation algorithm. *Phys. Rev. B*, **48**:589–592, Jul 1993. (Cited on page 20.)

[12] C. Gros. The boundary condition integration technique: results for the Hubbard model in 1D and 2D. *Z. Phys. B*, **86**:359, 1992. (Cited on page 21.)

[13] J. E. Gubernatis, Mark Jarrell, R. N. Silver, and D. S. Sivia. Quantum Monte Carlo simulations and maximum entropy: Dynamics from imaginary-time data. *Phys. Rev. B*, **44**:6011–6029, Sep 1991. (Cited on page 26.)

[14] Anders W. Sandvik. Stochastic method for analytic continuation of quantum Monte Carlo data. *Phys. Rev. B*, **57**:10287–10290, May 1998. (Cited on page 26.)

[15] K.S.D. Beach. Identifying the maximum entropy method as a special limit of stochastic analytic continuation. *arXiv cond-mat/0403055*, 2004. (Cited on page 26.)

[16] S.W. Lovesey. *The theory of neutron scattering from condensed matter*. Oxford science publications. Clarendon Press, 1986. (Cited on page 27.)

[17] Mohit Randeria, Nandini Trivedi, Adriana Moreo, and Richard T. Scalettar. Pairing and spin gap in the normal state of short coherence length superconductors. *Phys. Rev. Lett.*, **69**:2001–2004, Sep 1992. (Cited on page 29.)

[18] Nandini Trivedi and Mohit Randeria. Deviations from Fermi-Liquid Behavior above T_c in 2D Short Coherence Length Superconductors. *Phys. Rev. Lett.*, **75**:312–315, Jul 1995. (Cited on page 29.)

[19] Antoine Georges, Luca de' Medici, and Jernej Mravlje. Strong Correlations from Hundâs Coupling. *Annual Review of Condensed Matter Physics*, **4**(1):137–178, 2013. (Cited on page 29.)

[20] Antoine Georges, Gabriel Kotliar, Werner Krauth, and Marcelo J. Rozenberg. Dynamical mean-field theory of strongly correlated fermion systems and the limit of infinite dimensions. *Rev. Mod. Phys.*, **68**:13–125, Jan 1996. (Cited on pages 30, 36 and 49.)

[21] G. E. Moore. Cramming more components onto integrated circuits. *Electronics*, **38**:114–117. (Cited on page 31.)

[22] P. W. Anderson. Absence of Diffusion in Certain Random Lattices. *Phys. Rev.*, **109**:1492–1505, Mar 1958. (Cited on page 32.)

[23] L. Fleishman and P. W. Anderson. Interactions and the Anderson transition. *Phys. Rev. B*, **21**:2366–2377, Mar 1980. (Cited on page 32.)

[24] Patrick A. Lee and T. V. Ramakrishnan. Disordered electronic systems. *Rev. Mod. Phys.*, **57**:287–337, Apr 1985. (Cited on page 32.)

[25] D. Belitz and T. R. Kirkpatrick. The Anderson-Mott transition. *Rev. Mod. Phys.*, **66**:261–380, Apr 1994. (Cited on page 32.)

[26] V. Dobrosavljevic, N. Trivedi, and J. James M. Valles. *Conductor Insulator Quantum Phase Transitions*. OUP Oxford, 2012. (Cited on page 32.)

[27] Bhargavi Srinivasan, Giuliano Benenti, and Dima L. Shepelyansky. Delocalizing effect of the Hubbard repulsion for electrons on a two-dimensional disordered lattice. *Phys. Rev. B*, **67**:205112, May 2003. (Cited on page 32.)

[28] P. B. Chakraborty, P. J. H. Denteneer, and R. T. Scalettar. Determinant quantum Monte Carlo study of the screening of the one-body potential near a metal-insulator transition. *Phys. Rev. B*, **75**:125117, Mar 2007. (Cited on page 32.)

[29] Geneviève Fleury and Xavier Waintal. Many-Body Localization Study in Low-Density Electron Gases: Do Metals Exist in Two Dimensions? *Phys. Rev. Lett.*, **101**:226803, Nov 2008. (Cited on page 32.)

[30] Elihu Abrahams, Sergey V. Kravchenko, and Myriam P. Sarachik. Metallic behavior and related phenomena in two dimensions. *Rev. Mod. Phys.*, **73**:251–266, Mar 2001. (Cited on page 32.)

[31] D. Tanasković, V. Dobrosavljević, E. Abrahams, and G. Kotliar. Disorder Screening in Strongly Correlated Systems. *Phys. Rev. Lett.*, **91**:066603, Aug 2003. (Cited on page 32.)

[32] M. C. O. Aguiar, V. Dobrosavljević, E. Abrahams, and G. Kotliar. Effects of disorder on the non-zero temperature Mott transition. *Phys. Rev. B*, **71**:205115, May 2005. (Cited on page 32.)

[33] Miloš M. Radonjić, D. Tanasković, V. Dobrosavljević, and K. Haule. Influence of disorder on incoherent transport near the Mott transition. *Phys. Rev. B*, **81**:075118, Feb 2010. (Cited on page 32.)

[34] Richard T. Scalettar, Joel W. Cannon, Douglas J. Scalapino, and Robert L. Sugar. Magnetic and pairing correlations in coupled Hubbard planes. *Phys. Rev. B*, **50**:13419–13427, Nov 1994. (Cited on page 32.)

[35] K. Bouadim, G. G. Batrouni, F. Hébert, and R. T. Scalettar. Magnetic and transport properties of a coupled Hubbard bilayer with electron and hole doping. *Phys. Rev. B*, **77**:144527, Apr 2008. (Cited on page 32.)

[36] B.D. Napitu and J. Berakdar. Traces of the evolution from Mott insulator to a band insulator in the pair excitation spectra. *The European Physical Journal B*, **85**(2):1–10, 2012. (Cited on page 32.)

[37] Liang Du, Li Huang, and Xi Dai. Metal-insulator transition in three-band Hubbard model with strong spin-orbit interaction. *The European Physical Journal B*, **86**(3):1–8, 2013. (Cited on page 33.)

[38] N. Paris, K. Bouadim, F. Hebert, G. G. Batrouni, and R. T. Scalettar. Quantum Monte Carlo Study of an Interaction-Driven Band-Insulator–to–Metal Transition. *Phys. Rev. Lett.*, **98**:046403, Jan 2007. (Cited on pages 33 and 34.)

[39] J. Hubbard and J. B. Torrance. Model of the Neutral-Ionic Phase Transformation. *Phys. Rev. Lett.*, **47**:1750–1754, Dec 1981. (Cited on page 33.)

[40] J. B. Torrance, A. Girlando, J. J. Mayerle, J. I. Crowley, V. Y. Lee, P. Batail, and S. J. LaPlaca. Anomalous Nature of Neutral-to-Ionic Phase Transition in Tetrathiafulvalene-Chloranil. *Phys. Rev. Lett.*, **47**:1747–1750, Dec 1981. (Cited on page 33.)

[41] Naoto Nagaosa and Jun ichi Takimoto. Theory of Neutral-Ionic Transition in Organic Crystals. I. Monte Carlo Simulation of Modified Hubbard Model. *Journal of the Physical Society of Japan*, **55**(8):2735–2744, 1986. (Cited on page 33.)

[42] A P Kampf, M Sekania, G I Japaridze, and Ph Brune. Nature of the insulating phases in the half-filled ionic Hubbard model. *Journal of Physics: Condensed Matter*, **15**(34):5895, 2003. (Cited on page 33.)

[43] C. D. Batista and A. A. Aligia. Exact Bond Ordered Ground State for the Transition between the Band and the Mott Insulator. *Phys. Rev. Lett.*, **92**:246405, Jun 2004. (Cited on page 33.)

[44] Arti Garg, H. R. Krishnamurthy, and Mohit Randeria. Can Correlations Drive a Band Insulator Metallic? *Phys. Rev. Lett.*, **97**:046403, Jul 2006. (Cited on page 34.)

[45] K. Bouadim, N. Paris, F. Hébert, G. G. Batrouni, and R. T. Scalettar. Metallic phase in the two-dimensional ionic Hubbard model. *Phys. Rev. B*, **76**:085112, Aug 2007. (Cited on page 34.)

[46] S. S. Kancharla and E. Dagotto. Correlated Insulated Phase Suggests Bond Order between Band and Mott Insulators in Two Dimensions. *Phys. Rev. Lett.*, **98**:016402, Jan 2007. (Cited on page 34.)

[47] Kalobaran Maiti, Ravi Shankar Singh, and V. R. R. Medicherla. Evolution of a band insulating phase from a correlated metallic phase. *Phys. Rev. B*, **76**:165128, Oct 2007. (Cited on page 34.)

[48] V. Jaccarino, G. K. Wertheim, J. H. Wernick, L. R. Walker, and Sigurds Arajs. Paramagnetic Excited State of FeSi. *Phys. Rev.*, **160**:476–482, Aug 1967. (Cited on page 34.)

[49] C. Petrovic, Y. Lee, T. Vogt, N. Dj. Lazarov, S. L. Bud'ko, and P. C. Canfield. Kondo insulator description of spin state transition in $FeSb_2$. *Phys. Rev. B*, **72**:045103, Jul 2005. (Cited on page 34.)

[50] J. Kuneš and V. I. Anisimov. Temperature-dependent correlations in covalent insulators: Dynamical mean-field approximation. *Phys. Rev. B*, **78**:033109, Jul 2008. (Cited on page 34.)

[51] Michael Sentef, Jan Kunes, Philipp Werner, and Arno P. Kampf. Correlations in a band insulator. *Phys. Rev. B*, **80**:155116, Oct 2009. (Cited on pages 34 and 36.)

[52] Kazuo Hida. Quantum Disordered State without Frustration in the Double Layer Heisenberg Antiferromagnet. *Journal of the Physical Society of Japan*, **61**(3):1013–1018, 1992. (Cited on page 36.)

[53] Ling Wang, K. S. D. Beach, and Anders W. Sandvik. High-precision finite-size scaling analysis of the quantum-critical point of $S = 1/2$ Heisenberg antiferromagnetic bilayers. *Phys. Rev. B*, **73**:014431, Jan 2006. (Cited on page 36.)

[54] Z. Fisk, D. W. Hess, C. J. Pethick, D. Pines, J. L. Smith, J. D. Thompson, and J. O. Willis. Heavy-Electron Metals: New Highly Correlated States of Matter. *Science*, **239**(4835):33–42, 1988. (Cited on pages 49 and 50.)

[55] A.C. Hewson. *The Kondo Problem to Heavy Fermions*. Cambridge Studies in Magnetism. Cambridge University Press, 1997. (Cited on page 49.)

[56] W. Meissner and B. Voigt. Messungen mit Hilfe von flüssigem Helium XI Widerstand der reinen Metalle in tiefen Temperaturen. *Annalen der Physik*, **399**(7):761–797, 1930. (Cited on page 49.)

[57] W.J. de Haas, J. de Boer, and G.J. van den Berg. The electrical resistance of gold, copper and lead at low temperatures. *Physica*, **1**(7):1115 – 1124, 1934. (Cited on page 49.)

[58] Jun Kondo. Resistance Minimum in Dilute Magnetic Alloys. *Progress of Theoretical Physics*, **32**(1):37–49, 1964. (Cited on page 49.)

[59] K. Andres, J. E. Graebner, and H. R. Ott. $4f$-Virtual-Bound-State Formation in $CeAl_3$ at Low Temperatures. *Phys. Rev. Lett.*, **35**:1779–1782, Dec 1975. (Cited on page 50.)

[60] S. Doniach. The Kondo lattice and weak antiferromagnetism. *Physica B+C*, **91**(0):231 – 234, 1977. (Cited on pages 50 and 51.)

[61] J. R. Schrieffer and P. A. Wolff. Relation between the Anderson and Kondo Hamiltonians. *Phys. Rev.*, **149**:491–492, Sep 1966. (Cited on page 51.)

[62] S. Capponi and F. F. Assaad. Spin and charge dynamics of the ferromagnetic and antiferromagnetic two-dimensional half-filled Kondo lattice model. *Phys. Rev. B*, **63**:155114, Mar 2001. (Cited on page 51.)

[63] K. S. D. Beach, Patrick A. Lee, and P. Monthoux. Field-Induced Antiferromagnetism in the Kondo Insulator. *Phys. Rev. Lett.*, **92**:026401, Jan 2004. (Cited on page 51.)

[64] M. Vekić, J. W. Cannon, D. J. Scalapino, R. T. Scalettar, and R. L. Sugar. Competition between Antiferromagnetic Order and Spin-Liquid Behavior in the Two-Dimensional Periodic Anderson Model at Half Filling. *Phys. Rev. Lett.*, **74**:2367–2370, Mar 1995. (Cited on page 52.)

[65] A. Liebsch. Single Mott transition in the multiorbital Hubbard model. *Phys. Rev. B*, **70**:165103, Oct 2004. (Not cited.)

[66] R. Arita and K. Held. Orbital-selective Mott-Hubbard transition in the two-band Hubbard model. *Phys. Rev. B*, **72**:201102, Nov 2005. (Not cited.)

[67] Mucio A. Continentino, Gloria M. Japiassu, and Amós Troper. Thermodynamic properties of Kondo insulators. *Phys. Rev. B*, **49**:4432–4437, Feb 1994. (Cited on page 54.)

[68] Yukihiro Shimizu, Osamu Sakai, and Alex C. Hewson. The Effects of Band Dispersion and Interactions on the Excitation Gaps in the Periodic Anderson Model in Infinite Dimensions. *Journal of the Physical Society of Japan*, **69**(6):1777–1787, 2000. (Cited on page 54.)

[69] L. de' Medici, A. Georges, G. Kotliar, and S. Biermann. Mott Transition and Kondo Screening in f-Electron Metals. *Phys. Rev. Lett.*, **95**:066402, Aug 2005. (Cited on page 55.)

[70] Osamu Sakai, Yukihiro Shimizu, and Yasunori Kaneta. Band Calculation for Ce-Compounds on the basis of Dynamical Mean Field Theory. *Journal of the Physical Society of Japan*, **74**(9):2517–2529, 2005. (Cited on page 55.)

[71] A. Toropova, C. A. Marianetti, K. Haule, and G. Kotliar. One-electron physics of the actinides. *Phys. Rev. B*, **76**:155126, Oct 2007. (Cited on page 55.)

[72] Tsuneya Yoshida, Takuma Ohashi, and Norio Kawakami. Effects of Conduction Electron Correlation on Heavy-Fermion Systems. *Journal of the Physical Society of Japan*, **80**(6):064710, 2011. (Cited on page 55.)

[73] R. Hesper, L. H. Tjeng, A. Heeres, and G. A. Sawatzky. Photoemission evidence of electronic stabilization of polar surfaces in K_3C_{60}. *Phys. Rev. B*, **62**:16046–16055, Dec 2000. (Cited on page 67.)

[74] Satoshi Okamoto and Andrew J. Millis. Electronic reconstruction in correlated electron heterostructures. pages 593218–593218–17, 2005. (Cited on page 67.)

[75] Rob G. Moore, Jiandi Zhang, S. V. Kalinin, Ismail, A. P. Baddorf, R. Jin, D. G. Mandrus, and E. W. Plummer. Surface dynamics of the layered ruthenate Ca1.9Sr0.1RuO4. *physica status solidi (b)*, **241**(10):2363–2366, 2004. (Cited on page 67.)

[76] J. Mannhart. Interfaces in Materials with Correlated Electron Systems. In S.B. Ogale, editor, *Thin Films and Heterostructures for Oxide Electronics*, pages 251–278. Springer, 2005. (Cited on page 67.)

[77] J. Mannhart and D. G. Schlom. Oxide Interfaces - An Opportunity for Electronics. *Science*, 2010. (Cited on page 67.)

[78] J.K. Freericks. *Transport in multilayered nanostructures: the dynamical mean-field theory approach*. Imperial College Press, 2006. (Cited on page 67.)

[79] Millis A. Electronic Reconstruction at Surfaces and Interfaces of Correlated Electron Materials. In S.B. Ogale, editor, *Thin Films and Heterostructures for Oxide Electronics*, pages 279–297. Springer, 2005. (Cited on page 67.)

[80] E.Y. Tsymbal, E.R.A. Dagotto, C.B. Eom, and R. Ramesh. *Multifunctional Oxide Heterostructures*. OUP Oxford, 2012. (Cited on pages 67 and 68.)

[81] C. H. Ahn, J.-M. Triscone, and J. Mannhart. Electric field effect in correlated oxide systems. *Nature*, **424**(6952):1015–1018, Aug 2003. (Cited on page 68.)

[82] M. N. Baibich, J. M. Broto, A. Fert, F. Nguyen Van Dau, F. Petroff, P. Etienne, G. Creuzet, A. Friederich, and J. Chazelas. Giant Magnetoresistance of (001)Fe/(001)Cr Magnetic Superlattices. *Phys. Rev. Lett.*, **61**:2472–2475, Nov 1988. (Cited on page 68.)

[83] G. Binasch, P. Grünberg, F. Saurenbach, and W. Zinn. Enhanced magnetoresistance in layered magnetic structures with antiferromagnetic interlayer exchange. *Phys. Rev. B*, **39**:4828–4830, Mar 1989. (Cited on page 68.)

[84] W.C. Lee and The University of Texas at Austin. Physics. *Electronic Properties of Strongly Correlated Layered Oxides*. University of Texas at Austin, 2008. (Cited on page 68.)

[85] Igor Žutić, Jaroslav Fabian, and S. Das Sarma. Spintronics: Fundamentals and applications. *Rev. Mod. Phys.*, **76**:323–410, Apr 2004. (Cited on page 68.)

[86] J. Stangl, V. Holý, and G. Bauer. Structural properties of self-organized semiconductor nanostructures. *Rev. Mod. Phys.*, **76**:725–783, Sep 2004. (Cited on page 68.)

[87] Jinbo Cao and Junqiao Wu. Strain effects in low-dimensional transition metal oxides. *Materials Science and Engineering: R: Reports*, **71**(2):35–52, 2011. (Cited on page 68.)

[88] A. Ohtomo, D. A. Muller, J. L. Grazul, and H. Y. Hwang. Artificial charge-modulationin atomic-scale perovskite titanate superlattices. *Nature*, **419**(6905):378–38, Sep 2002. (Cited on pages 68 and 69.)

[89] A. Ohtomo and H. Y. Hwang. A high-mobility electron gas at the LaAlO3/SrTiO3 heterointerface. *Nature*, **427**(6973):423–426, Jan 2004. (Cited on page 69.)

[90] S. Thiel, G. Hammerl, A. Schmehl, C. W. Schneider, and J. Mannhart. Tunable Quasi-Two-Dimensional Electron Gases in Oxide Heterostructures. *Science*, **313**(5795):1942–1945, 2006. (Cited on page 69.)

[91] H. Jeffrey Gardner, Ashwani Kumar, Liuqi Yu, Peng Xiong, Maitri P. Warusawithana, Luyang Wang, Oskar Vafek, and Darrell G. Schlom. Enhancement of superconductivity by a parallel magnetic field in two-dime nsional superconductors. *Nat Phys*, **7**(11):895–900, Nov 2011. (Cited on page 69.)

[92] Vladimir I Anisimov, F Aryasetiawan, and A I Lichtenstein. First-principles calculations of the electronic structure and spectra of strongly correlated systems: the LDA + U method. *Journal of Physics: Condensed Matter*, **9**(4):767, 1997. (Cited on page 69.)

[93] Satoshi Okamoto, Andrew J. Millis, and Nicola A. Spaldin. Lattice Relaxation in Oxide Heterostructures: $LaTiO_3/SrTiO_3$ Superlattices. *Phys. Rev. Lett.*, **97**:056802, Jul 2006. (Cited on page 69.)

[94] H. Ishida and A. Liebsch. Embedding approach for dynamical mean-field theory of strongly correlated heterostructures. *Phys. Rev. B*, **79**:045130, Jan 2009. (Cited on page 69.)

[95] W. Schottky. Halbleitertheorie der Sperrschicht. *Naturwissenschaften*, **26**:843–843, dec 1938. (Cited on page 70.)

[96] Kenji Yonemitsu, Nobuya Maeshima, and Tatsuo Hasegawa. Suppression of rectification at metal–Mott insulator interfaces. *Phys. Rev. B*, **76**:235118, Dec 2007. (Cited on page 70.)

[97] Luis G. G. V. Dias da Silva, Khaled A. Al-Hassanieh, Adrian E. Feiguin, Fernando A. Reboredo, and Elbio Dagotto. Real-time dynamics of particle-hole excitations in Mott insulator-metal junctions. *Phys. Rev. B*, **81**:125113, Mar 2010. (Cited on page 70.)

[98] Takashi Oka and Naoto Nagaosa. Interfaces of Correlated Electron Systems: Proposed Mechanism for Colossal Electroresistance. *Phys. Rev. Lett.*, **95**:266403, Dec 2005. (Cited on page 70.)

[99] R. W. Helmes, T. A. Costi, and A. Rosch. Kondo Proximity Effect: How Does a Metal Penetrate into a Mott Insulator? *Phys. Rev. Lett.*, **101**:066802, Aug 2008. (Cited on pages 70 and 84.)

[100] Sherman A. and Voropajeva N. Excitations near the boundary between a metal and a Mott insulator. *Int. J. Mod. Phys. B*, **24**:979, 2010. (Cited on pages 70 and 84.)

[101] C. He, X. Zhai, V. V. Mehta, F. J. Wong, and Y. Suzuki. Interfacial magnetism in $CaRuO_3/CaMnO_3$ superlattices grown on (001) $SrTiO_3$. *Journal of Applied Physics*, **109**(7):07D729, 2011. (Cited on page 70.)

[102] T. Menke, P. Meuffels, R. Dittmann, K. Szot, and R. Waser. Separation of bulk and interface contributions to electroforming and resistive switching behavior of epitaxial Fe-doped $SrTiO_3$. *Journal of Applied Physics*, **105**(6):066104, 2009. (Cited on page 71.)

[103] A. A. Fursina, R. G. S. Sofin, I. V. Shvets, and D. Natelson. Interfacial transport properties between a strongly correlated transition metal oxide and a metal: Contact resistance in Fe_3O_4/M (M = Cu, Au, Pt) nanostructures. *Phys. Rev. B*, **82**:245112, Dec 2010. (Cited on page 71.)

[104] Y. Tokunaga, Y. Kaneko, J. P. He, T. Arima, A. Sawa, T. Fujii, M. Kawasaki, and Y. Tokura. Colossal electroresistance effect at metal electrode/$La_{1-x}Sr_{1+x}MnO_4$ interfaces. *Applied Physics Letters*, **88**(22):223507, 2006. (Cited on page 71.)

[105] Ko Munakata, Theodore H. Geballe, and Malcolm R. Beasley. Quenching of impurity spins at Cu/CuO interfaces: An antiferromagnetic proximity effect. *Phys. Rev. B*, **84**:161405, Oct 2011. (Cited on page 71.)

[106] Satoshi Okamoto. Nonequilibrium transport and optical properties of model metal–Mott-insulator–metal heterostructures. *Phys. Rev. B*, **76**:035105, Jul 2007. (Cited on page 71.)

[107] H. Zenia, J. K. Freericks, H. R. Krishnamurthy, and Th. Pruschke. Appearance of "Fragile" Fermi Liquids in Finite-Width Mott Insulators Sandwiched between Metallic Leads. *Phys. Rev. Lett.*, **103**:116402, Sep 2009. (Cited on page 71.)

[108] Sanjay Gupta and Tribikram Gupta. Physics of a metal-correlated barrierâmetal heterostructure. *Solid State Communications*, **152**(2):53 – 55, 2012. (Cited on page 71.)

[109] Silvia B. Bacci, Eduardo R. Gagliano, Richard M. Martin, and James F. Annett. Derivation of a one-band Hubbard model for CuO planar materials. *Phys. Rev. B*, **44**:7504–7509, Oct 1991. (Cited on page 78.)

[110] P Coleman, C Pépin, Qimiao Si, and R Ramazashvili. How do Fermi liquids get heavy and die? *Journal of Physics: Condensed Matter*, **13**(35):R723, 2001. (Cited on page 80.)

[111] B. Sinković, B. Hermsmeier, and C. S. Fadley. Observation of Spin-Polarized Photoelectron Diffraction. *Phys. Rev. Lett.*, **55**:1227–1230, Sep 1985. (Cited on page 83.)

Abstract: The properties of electrons in two dimensions (2D) raise fundamental questions that have been extensively explored by condensed matter theory. Extending standard frameworks such as the 2D Hubbard model by accounting for more than one electronic band offers the opportunity to access more complex phenomena, such as the interplay between transport and magnetism found in heavy-fermions materials. Such models are directly connected to the problem of coupled layers in complex materials known as heterostructures, which have been widely studied and synthesized in recent years, and are expected to lead to important applications. In that context, we study numerically several systems, by mean of the Determinant Quantum Monte Carlo Method (DQMC). We first analyze the effect of electronic correlation in a band insulator, showing in particular the absence of an intermediate metallic phase. A second system consists of two coupled bands that modelize a heavy fermion model, in which the role of the bandwidth of the correlated band is systematically investigated. Finally, we consider the case of a metal-insulator interface, unveiling an intriguing intermediate phase as the interfacial coupling is tuned.

Keywords: *Condensed matter physics, Strongly correlated systems, Hubbard model, Heterostructures, Quantum Monte Carlo, Phase transitions.*

Résumé: Les propriétés d'électrons en deux dimensions (2D) soulèvent des questions fondamentales qui ont été largement explorées au moyen des techniques théoriques de la matière condensée. L'extension de modèles classiques tel le modèle de Hubbard en 2D, en incluant par exemple plusieurs bandes électroniques, offre la possibilité d'accéder à des phénomèmes plus complexes, comme l'interaction du transport électronique et du magnétisme observé dans les composés de fermions lourds. Ces modèles sont en lien direct avec la question de couches minces couplées, les hétérostructures, qui sont depuis peu l'objet d'intenses recherches et offrent la possibilité d'intéressantes applications. Dans ce contexte, nous étudions numériquement différents systèmes au moyen de la méthode du Monte Carlo Quantique du Déterminant. Tout d'abord, l'effet de la corrélation électronique dans un isolant de bande est évaluée, montrant en particulier l'absence d'une phase métallique intermédiaire. Un deuxième système est composé de deux bandes électroniques couplées, dans lequel l'effet de la largeur de bande de la partie corrélée est exploré de façon systématique. Finalement, nous étudions une interface métal-isolant, qui présente une phase intermédiaire surprenante lorsque le couplage à l'interface est ajusté.

Keywords: *Physique de la matière condensée, Systèmes fortement corrélés, Modèle de Hubbard, Hétérostructures, Monte Carlo Quantique, Transitions de phases.*